Semi Annual Report

(July 1 — December 31, 2002)

Contract Number NAS5—31363

OCEAN OBSERVATIONS WITH EOS/MODIS:

Algorithm Development and Post Launch Studies

Kenneth J. Voss, PI
University of Miami
Department of Physics
Coral Gables, FL 33124

(Submitted January 15, 2003)

Preamble

This document describes our progress thus far toward completion of our research plans regarding two MODIS Ocean-related algorithms.

A. Retrieval of the Normalized Water-Leaving Radiance (Atmospheric Correction).
B. Retrieval of the Detached Coccolith/Calcite Concentration

In addition, we break our effort into two broad components for each algorithm:

- Algorithm Improvement/Enhancement;
- Validation of MODIS Algorithms and Products.

These components will overlap in some instances.

RETREIVAL OF NORMALIZED WATER-LEAVING RADIANCE (ATMOSPHERIC CORRECTION)

Algorithm Improvement/Enhancement

1. Evaluation/Tuning of Algorithm Performance

Task Progress:

As indicated in our last Semiannual Report, considerable effort has been expended by R. Evans and co-workers toward removing the instrumental artifacts from Terra/MODIS ocean imagery. Examples of such artifacts are severe striping, mirror side differences, effects of the variation of the instruments response as a function of scan angle, and the influence of instrumental polarization sensitivity. Sufficient progress has been made along these lines that MODAPS has begun the first retrospective reprocessing of Terra/MODIS ocean data.

We now believe there is a significantly larger fresnel-surface-reflection contribution in the case of MODIS compared to SeaWiFS. Part of this is the difference in equator crossing time that influences the sun-viewing geometry; however, we believe the effects are much larger than those caused by geometry alone. Although we have developed no conclusive answer yet, one possibility that we are investigating is the stabilization of the unstable morning atmosphere as the day progresses. In some cases the atmosphere may be unstable at the time of SeaWiFS overpass, but stable for the MODIS overpass. Atmospheric stability influences the sea surface roughness, which in turn influences its reflectance.

Anticipated Future Actions:

Although we will continue to work on Terra, our main effort under this task is to work with R. Evans in readying Aqua data for ocean processing. In addition, we will compare Aqua and Terra in regard to the sea surface roughness effects. If our hypothesis is correct, the effects should be significantly smaller in Aqua than in Terra.

2. and 3. Algorithm Enhancements

There are two important issues we are examining for inclusion into the MODIS algorithm: effecting atmospheric correction in the presence of strongly absorbing aerosols and/or Case 2 waters; and including the influence of the subsurface upwelling BRDF on water-leaving radiance.

Strongly Absorbing Aerosols/Case 2 waters

The first of the two enhancements we have been considering concerns absorbing aerosols. It also concerns Case 2 (coastal) waters, as strongly absorbing aerosols can be expected near the coasts due to urban pollution. Although success with SeaWiFS has shown that the MODIS algorithm performs well in ~ 90% of Case 1 water situations, it does not perform adequately everywhere; most notably in atmospheres containing strongly absorbing aerosols, or in turbid coastal waters that have high concentrations of all optically active constituents. Two important situations in which absorbing aerosols make an impact are desert dust and urban pollution carried over the oceans by the winds. In the case of urban pollution the aerosol contains black carbon and usually exhibits absorption that is nonselective, i.e., the imaginary part of the refractive index (the absorption index) is independent of wavelength. In contrast, desert dust absorbs more in the blue than the red, i.e., the absorption index decreases with wavelength. Generally, analysis of imagery contaminated by strongly absorbing aerosols require that atmospheric correction and water-constituent retrieval be carried out simultaneously. The same is true for Case 2 coastal waters. Because of the similarity of the algorithm requirements, we treat absorbing aerosols and Case 2 waters together.

Task Progress:

Previously, we applied (and validated) the spectral optimization algorithm [R.M. Chomko and H.R. Gordon, Atmospheric correction of ocean color imagery: Test of the spectral optimization algorithm with SeaWiFS, *Applied Optics*, **40**, 2973—2984, 2001] with the Garver and Siegel reflectance model ["Inherent optical property inversion of ocean color spectra and its biogeochemical interpretation: 1 time series from the Sargasso Sea," *Geophys. Res.*, **102C**, 18607—18625, 1997] in Case 1 waters. The results have just been published [R.M. Chomko, H. R. Gordon, S. Maritorena, D.A. Siegel, Simultaneous retrieval of oceanic and atmospheric parameters for ocean color imagery by spectral optimization: A validation, *Remote Sensing of Environment* **84,** 208—220, 2003]**.** We have now applied of the spectral optimization algorithm to Case 2 waters using SeaWiFS data, and are debugging the code for MODIS imagery. The initial application with MODIS imagery suggests that some sensor recalibration is required for the NIR bands and we are looking in to this. A description and progress report is provided in **Appendix I** (PowerPoint presentation made at the MODIS Science Team Meeting July 2002**).** A validation of the method using SeaWiFS data, and the implementation/debugging effort with MODIS is on going. We are using the ACE-Asia data set to provide validation of the algorithm in the waters that are a Case 2 *in the presence of* absorbing aerosols. During ACE-Asia, we cooperated in the operation of an MPL to obtain vertical profiles of aerosol extinction. A graduate student (David Bates) operated the lidar and analyzed the data in partial fulfillment of his Ph.D degree. The results are presented in his dissertation which is included here as **Appendix II**.

We have also replaced the Gordon et al. [A Semi-Analytic Radiance Model of Ocean Color, *Jour. Geophys. Res*., **93D**, 10909-10924 (1988)] reflectance model with the

Garver and Siegel (1997) model in our spectral matching algorithm for operation in wind-blown dust [C. Moulin, H.R. Gordon, R.M. Chomko, V.F. Banzon, and R.H. Evans, Atmospheric correction of ocean color imagery through thick layers of Saharan dust, *Geophys. Res. Lett.*, **28**, 5-8, 2001]. We tested it on a dusty image off West Africa with encouraging results, however, we continue to have problems if the candidate aerosol models include both dust and non-dust models. We are now in the process of debugging a version of the code for MODIS. We are also preparing a Case 2 version of this code so that we can validate it with the ACE-Asia imagery, for which Asian dust was known to be present.

Anticipated Future Actions:

We will continue to implement the absorbing aerosol algorithms into the MODIS processing code, as we believe they are the most versatile. In the case of the spectral matching algorithm we will examine its efficacy for atmospheric correction through African dust in the Arabian Sea. We will also process the ACE-Asia imagery with a Case 2 version of the spectral matching code, as the area was known to have been subjected to Asian dust during the exercise.

In the case of the spectral optimization algorithm for use in Case 2 waters, we believe that our implementation problem may be due to the MODIS calibration in the NIR. As such, we are undertaking a complete review of our calibration procedure at the MOBY site in the light of recent results regarding maritime aerosols [e.g., Y.J. Kaufman, *et al*., Baseline maritime aerosol: methodology to derive the optical thickness and scattering properties, *Geophys. Res. Lett.*, **28**, 3251—3254 (2001)]. When the code is operating properly in the MODIS processing environment at Miami, we will provide MODAPS with code for routinely processing a subsetted coastal region in a research mode. Although the code will be very slow, application to a small region is feasible. Our goal for the next reporting period is to provide a demonstration of the value of MODIS imagery in Case 2 waters, as well as to provide users with the methodology and software tools for processing MODIS imagery in such waters. We are looking for coastal regions where algorithms of the Garver-Seigel type have been tuned to specific Case 2 waters. Likely candidates are the Chesapeake Bay and/or the Gulf of Maine.

.

The subsurface upwelling BRDF

The subsurface BRDF issue involves relating measurements of the upwelled spectral radiance (used for bio-optical algorithm development, sensor calibration and product validation of all ocean color sensors) that are predominately made in the nadir-viewing direction (including MOBY data), with the water-leaving radiance at the remote sensor. The remote sensing viewing geometry is rarely nadir, thus an understanding of the difference of these two geometries is required, i.e., we need to understand the BRDF of the subsurface radiance distribution to reconcile these measurements. Our approach is to directly measure the BRDF as a function of the chlorophyll concentration and to

develop a model that can be used for MODIS. In addition we are working on a specific algorithm for correcting the MOBY buoy data to address the BRDF effects at this location.

Task progress:

During this period the majority of our effort on this task was spent on reducing data from the May cruise off of Hawaii, participating in and reducing the data from the Chesapeake Bay cruise, and participating in another cruise in October.

The May cruise was timed to take place during the period when the sun achieves its maximum solar elevation in Hawaii. By taking data during cloud free periods of the day we get a complete set of clear water radiance distributions for all sun angles. To allow us to stay on a single station all day we used the small vessel in Hawaii, the R/V Klaus Wyrtki. Data were taken on several days from early in the morning until the sky became too cloudy. Along with the radiance distribution; sky irradiance, absorption and beam attenuation were measured continuously. Periodic casts were performed of the water upwelling radiance and irradiance along with water temperature to document the water column properties. This produced an enormous amount of data (over 6Gbytes) which we are still trying to ingest and analyize.

The Chesapeake Bay data was important for the opportunity to collect Case II water samples. This data has been reduced, but we really have not gone in depth in the analysis of the data. The October cruise is discussed elsewhere in the report.

Anticipated Future Actions:

We are working at analyzing data from the May cruise, the Chesapeake Bay cruise, and working with the comparison with the Morel model. In addition we anticipate having another time series cruise in Hawaii, another Chesapeake Bay cruise, and a short MOCE cruise in January. In total, we will be very busy in the coming period.

Validation of MODIS Algorithms and Products

4. Participate in MODIS Initialization/Validation Campaigns

This task refers to our participation in actual Terra/MODIS validation/initialization exercises.

Task Progress:

While most of our effort the last six months has been directed towards the new radiance distribution camera system (NuRADS), we continued to maintain our CIMEL station in the Dry Tortugas during this period. This station will be used to help validate the MODIS derived aerosol optical depth (AOD), and aid in investigating the calibration of the near infrared (NIR) spectral bands of MODIS.

We have finished our analysis of the ACE-Asia lidar work. The results are presented in a thesis by David Bates, and are attached as an appendix to this report. The results will now be used in our algorithm development effort.

We participated in the MOCE cruise in October, which was an effort to get post launch data for the Aqua validation. However the weather was totally uncooperative during this period and we only had one day of data. We will participate in another attempt to obtain Aqua validation data later this month.

Two of the instruments we operate during the larger MOCE cruises are the sky radiance distribution camera and the aureole camera system. Both of these camera systems are nearly 10 years old, and both failed in the period since the last MOCE cruise. We are currently replacing the cameras in both of these systems, and rebuilding the portions of the systems that require replacing.

Anticipated future efforts:

We will finish rebuilding the sky radiance camera system and the aureole camera system. In addition we are investigating various methods of calibration for these systems with the aim to improve our calibration accuracy.

We have a busy schedule with MODIS field campaigns in the next 6 months. Currently we will be participating in a cruise in January, a cruise in April, and a cruise in May. Each of these cruises will have different objectives.

The January cruise will be a post launch Aqua cruise. Unfortunately, the cruise we participated in during October did not experience weather suitable for the cal/val work. Thus we will try again during this short January cruise, which is done in conjunction with the MOBY instrument swap.

In April we will be participating in a small boat operation out of Honolulu. The idea in this part is to make more extensive measurements of the BRDF over a long time period each day. This allows us to look at the variation of the BRDF with sun zenith angle, at least in clear water. This will be an important addition to our data set.

In May we will be participating in Dennis Clarks cruise in the Chesapeake. This is an important data set as it is a very high Chlorophyll, Case 2 data set. Here the BRDF effects may be very important. We have some data from the cruise last spring, which we will be reducing, however we should use this opportunity to collect some more data as we do not have many data points in this turbid water.

We are anticipating now that the long MOCE cruise will be next fall, out of the time period covered in this report.

5. Complete Analysis of SeaWiFS Validation Campaign Data

Task Progress:

We have been comparing our BRDF data from the MOCE-5 cruise with the model proposed by Andre Morel. Initial looks at the data have shown that the model works fairly well, however there can be fairly large (20%) discrepancies. We are currently working with Dr. Morel to finish up the comparison and pin down the areas where there are problems.. We have been investigating the inversion of the sky radiance

data acquired during the MOCE-5 cruise. We want to obtain the aerosol scattering phase function using this data. Unfortunately this has not worked well to date. We are currently examining possible reasons for the failure of the inversion technique, in particular we are working on a solar reflectance based calibration.

Anticipated future efforts:

We will continue our efforts at validating the Morel model. We will be investigating reflectance-based field methods of calibrating the sky radiometers to improve the accuracy of the instrument calibration and hence the ability to perform inversions. Since the sky cameras have been very stable, if a constant offset can be found between the reflectance-based calibrations obtained in the field and the in-lab calibrations we will be able to correct our previous calibrations and invert the sky data from the MOCE-5 cruise.

RETRIEVAL OF DETACHED COCCOLITH/CALCITE CONCENTRATION MOD 23

William M. Balch
Bigelow Laboratory for Ocean Sciences
POB 475
McKown Point
W. Boothbay Harbor, ME 04575

This last half year of work has focused on several areas: 1) processing of 2002 Gulf of Maine PIC data 2) work-up of chalk-ex results, 3) acquisition of new validation samples for MODIS-Terra and MODIS-Aqua validation, 4) submission of a manuscript on optics and hydrography of the Gulf of Maine (which includes material on acid-labile backscattering from PIC), writing a new manuscript for a book chapter which includes a description of the MODIS PIC product plus our recently computed global views of surface PIC through the four seasons, 5) presentation of MODIS results at several meetings.

Algorithm Evaluation/Improvement

Task Progress:

Much of our attention in algorithm evaluation has been directed to running the revised MODIS radiances into the PIC algorithm for MOD 23 (following reprocessing of all the MODIS-Terra data. These data are now correct for instrumental artifacts such as striping, mirror side differences, effects of the variation of the instrument's response as a function of scan angle, and the influence of instrument polarization sensitivity. Moreover, as a cross-check, we have also run SeaWiFS radiances through the same PIC algorithm in order to compare the derived PIC values. At low PIC concentrations typical of non-bloom conditions, the MODIS and SeaWiFS-derived results compare favorably (no statistical bias was evident between the two instruments). We are currently checking new MODIS-Aqua data to evaluate algorithm performance in the Gulf of Maine. Global views of PIC from MODIS-Aqua compare favorably to those of MODIS-Terra. Lastly, we spent time trying to resolve significant differences between the two-band PIC algorithm (implemented with MODIS data) and the three-band algorithm (as implemented with SeaWiFS). The latter has been giving significantly higher values. We discovered that the problem was related to the assumed background backscattering value used with the three-band algorithm. The problem has since been corrected, and we are re-comparing the MODIS two-band results with the SeaWiFS three-band results.

Validation of MODIS Algorithms and Products

As coccoliths and suspended PIC (particulate inorganic carbon or calcium carbonate) are new products, and as Terra was only launched in December 1999 and Aqua launched in May '02, there are relatively few data sets available for validation,

particularly for the coccolith and suspended calcite products. This is because coccolith concentration (PIC) is not frequently measured at sea, while chlorophyll concentration is. In conjunction with our NASA SIMBIOS activities, much of our validation estimates come from the Gulf of Maine, the site of frequent blooms of coccolithophores, and a region readily accessible from our laboratory.

Validation of regional PIC

During 2002, we acquired 108 new PIC samples from our Gulf of Maine ferry studies. These are currently being prepared for processing. Coccolith samples were taken at the same 108 stations, and those tedious microscope counts are ongoing. Parallel PIC samples and coccolith counts are taken in order to check the coccolith-to-carbon conversion which is implicit in the MODIS two band algorithm. We have demonstrated using previous data that satellite-derived normalized water-leaving radiances are statistically correlated to the absolute PIC concentration, accounting for as much as 40% of the variance. Moreover, the nLw's are even better correlated to the coccolith concentration; coccolith concentration accounts for just over 50% of the variance in nLw's in the blue and green wavelengths.

Chalk-Ex

All Chalk-Ex data from our Nov' 01 cruise have been processed, and worked-up. Presentations on various aspects of this work were given at the July '02 MODIS meeting in Greenbelt, MD, November '02 Ocean Optics meeting in Santa Fe, November '02 IWG meeting in Maryland and December AGU meeting in San Francisco. The analysis involved extracting MODIS data from the Chalk-Ex overpasses, and comparing the results to ship-derived, aerially integrated, nLw-based, estimates of PIC made from ship. The MODIS PIC estimates were within 18% of the ship-based estimates (Fig. 1) . We are currently preparing for our June '03 Chalk-Ex cruise.

<u>New validation data</u>

Gulf of Maine cruises ended on the M/S *Scotia Prince* ferry in late October of 2002. One hundred percent of this year's trips were under clear skies, which was a record for us. Combined with last year's work, of our last 24d at sea in the Gulf of Maine, 23 have been under clear skies with at least one satisfactory satellite overpass per trip. This year also saw several of the first "triple-header" trips in which SeaWiFS, MODIS-Terra and MODIS-Aqua instruments had good overpasses of the ferry track (where the satellite viewed the ship at nadir.

<u>Checks of global data set</u>

As a means to cross-check the PIC algorithm, we have estimated total global PIC using the reprocessed 36km monthly averaged data. Moreover, we have performed a statistical analysis to estimate the standard error limits for the MODIS data, binned at different time and space scales. Given our estimates of RMS error of our 1km resolution,

1 day PIC estimates (SD=14.9ug PIC L^{-1}), we conclude that for 4.6km resolution data, the standard error of the PIC estimate is 1.2ug PIC L^{-1}, quite close to typical background levels in the sea. For 36km monthly averages, the expected standard error of the PIC estimates is 0.08ug PIC L^{-1}, well below typical background levels (Table 1).

Validation of global PIC and coccolithophore pigment data

Cautions when using coccolith/PIC data products

The coccolithophore data products are "provisionally validated", given that we have defined the RMS error based on ship validation measurements, under a wide range of PIC concentrations, using the Version 3.4 re-processed data. We nonetheless caution using these data from shallow ocean regions, particularly near carbonate banks (e.g. Grand Bahamas), where bottom reflectance will appear as a high-reflectance coccolithophore bloom (presumably such pixels would be flagged due to their shallowness). Moreover, near river mouths and in shallow waters, resuspended sediments (of non-calcite origin) may appear as high suspended calcite concentrations. Only use these data if the waters are sufficiently deep to not have such bottom resuspension or direct river impact. Beware that MODIS-derived coccolith concentrations assume that the coccoliths are from the Prymnesiophyte, *E. huxleyi*. If this is not true, then inaccuracies will increase although the errors are not expected to be large. Even when using the data in units of mg m^{-3}, they nevertheless assume a constant backscattering cross-section for *E. huxleyi*, which is known to vary with the size of the calcite particle.

Web Links to Relevant Information

The algorithm theoretical basis document for the coccolithophore products can be found at: http://modis.gsfc.nasa.gov/MODIS/ATBD/atbd_mod23.pdf

More information about the algorithm and inputs can be found in:

Esaias, W., et al., 1998, Overview of MODIS Capabilities for Ocean Science Observations, *IEEE Transactions on Geoscience and Remote Sensing*, **36**, 1250 1265.

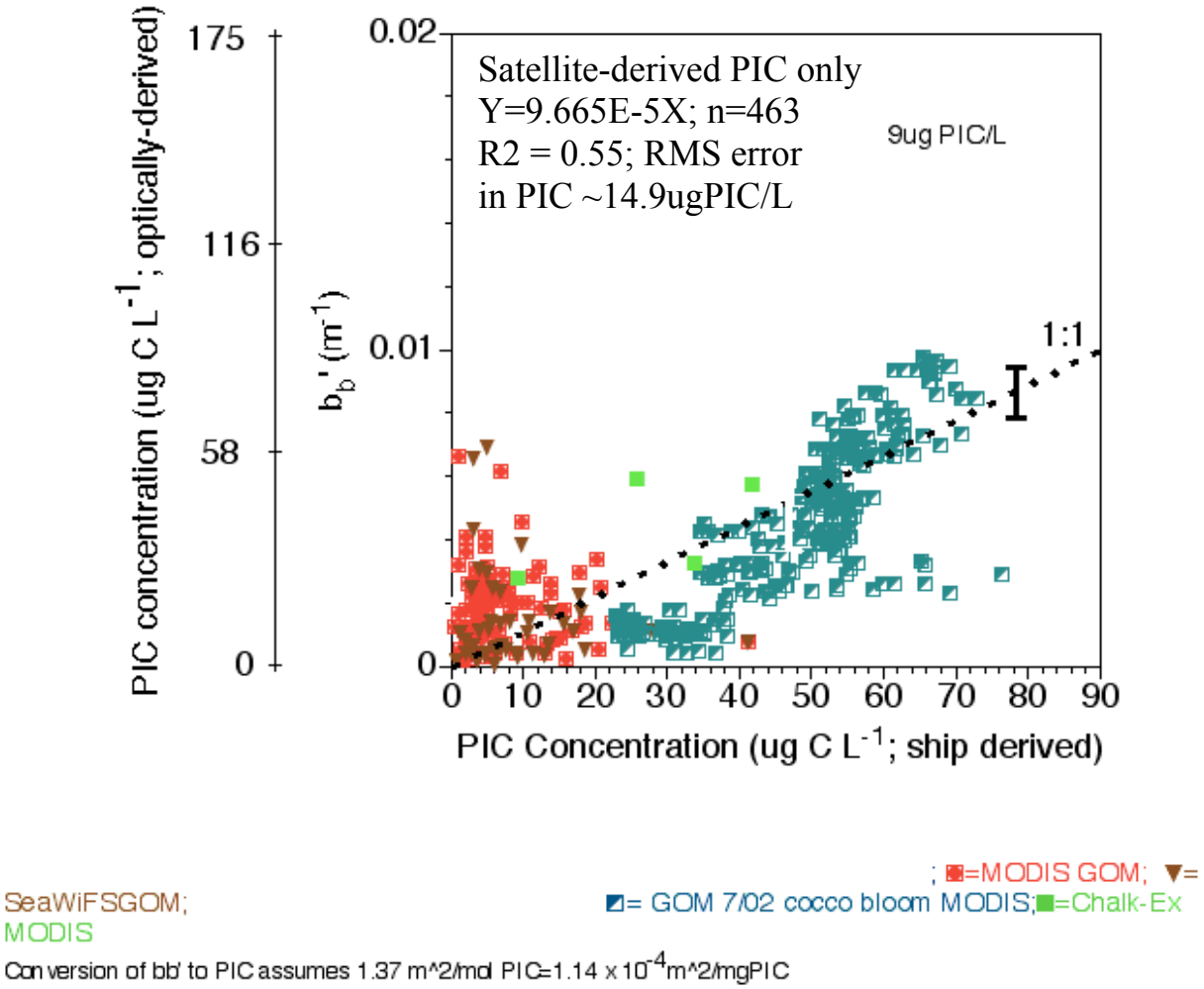

Fig. 1- Plot of MODIS-derived PIC concentration versus ship-derived estimates. All ship validation data from the Gulf of Maine (including data from the '02 coccolithophore bloom) are shown along with the Chalk-Ex results. Statistics are shown in the plot.

Spatial res (km)	1	4.63	36	111.2
Time bins (d)				
1	14.900	3.218	0.414	0.134
7	5.632	1.216	0.156	0.051
30	2.720	0.588	0.076	0.024
365	0.780	0.168	0.022	0.007

Table 1- Standard error estimates for PIC determinations as a function of time and space scales of image binning. Units are in ugPIC per liter.

Anticipated future efforts:

Our future efforts will be:

4. Work-up of the samples and validation data collected from the Gulf of Maine during 2002.
5. Continued sampling for PIC validation using the M/S Scotia Prince ferry in '03 (12 trips scheduled for clear-sky days)

6. Submission of book chapter for the new Springer book on coccolithophores (which includes a discussion of the MODIS algorithm and global results) .

7. Required revisions for our submitted paper on the Gulf of Maine results.

8. Further write-up of our Gulf of Maine results and PIC algorithm results. We have two more papers in preparation on the Gulf of Maine results. We will also begin a paper on the PIC algorithm and its performance.

9. Preparing for the third Chalk-Ex experiment in '03. Our last chalk experiment is slated for June '03 and this will require significant preparations as the date nears.

Referencing Data in Journal Articles

Results derived from this algorithm should cite the paper of Gordon et al.(Gordon et al. 1988) for the original discussion, and (Balch et al. 1996; Balch et al. 1999) for field data on the backscattering cross-section of calcite.

Citations

Balch, W. M., K. Kilpatrick, P. M. Holligan, D. Harbour, and E. Fernandez. 1996. The 1991 coccolithophore bloom in the central north Atlantic. II. Relating optics to coccolith concentration. Limnol. Oceanogr. **41:** 1684-1696.

Balch, W. M., D. T. Drapeau, T. L. Cucci, R. D. Vaillancourt, K. A. Kilpatrick, and J. J. Fritz. 1999. Optical backscattering by calcifying algae--Separating the contribution by particulate inorganic and organic carbon fractions. J. Geophys. Res. **104:** 1541-1558.

Gordon, H. R., O. B. Brown, R. H. Evans, J. W. Brown, R. C. Smith, K. S. Baker, and D. K. Clark. 1988. A semianalytic radiance model of ocean color. J. Geophys. Res. **93:** 10909-10924.

Additional Developments

The following presentations were made during the previous half year:

Balch, W. M., B. Bowler, D. Drapeau, J. Goes, and E. Booth. 2002. MODIS coccolith algorithm: Results. July 2002 MODIS Team Meeting. Greenbelt, MD.

H.R. Gordon, **R.M. Chomko**, R.E. Evans, J.W. Brown, S. Walsh and W. Baringer, An Algorithm for Coastal Water and the Status of its Implementation into the MODIS Processing Stream. July 2002 MODIS Team Meeting. Greenbelt, MD.

K. J. Voss and D.K.Clark, Radiance distribution measurements in clear water. Poster presented at the July 2002 MODIS Team Meeting. Greenbelt, MD.

K. J. Voss and D.K.Clark, Radiance distribution measurements in clear water. Poster presented at the November 2002 IWG Meeting. Baltimore, MD.

H.R. Gordon presented a short course (6 hrs) "Atmospheric correction of ocean color imagery: alpha to psi" at *Ocean Optics* XVI, Santa Fe, NM (on Nov. 16, 2002).

Presentations (2002)

(NAS5-31363 Personnel bold highlighted)

Balch, W. M. 2002. New observations of coccoliths from satellites, ferries, towed vehicles and balloons. Keynote talk. Coccolithophores- from molecular processes to global impact. Conference at Centro Stefano Franscini, Monte Verita, Ascona, Switzerland, 10-15 February 2002.

Balch, W.M., Bowler, B., Drapeau, D., **Gordon, H**., Scally, E., Ashe, A. 2002. Quantitative, space-based measurements of oceanic suspended ocean calcium carbonate with MODIS and SeaWiFS. AGU/ASLO Ocean Sciences Meeting, Honolulu, Hawaii. February 2002.

Drapeau, D. T., **W.M. Balch**, B.C. Bowler, E. Scally, J. Goes, A. Ashe. 2002. A multi-year record of bio-optical properties in the Gulf of Maine. AGU/ASLO Ocean Sciences Meeting, Honolulu, Hawaii. February 2002.

W.M. Balch, , B.C. Bowler, D.T. Drapeau, **H.R. Gordon**, E. Booth, A. Ashe, Quantitative, space-based measurements of ocean suspended calcium carbonate with MODIS and SeaWiFS, Eos. Trans. AGU, 83(4), Ocean Sciences Meet. Suppl., Abstract OS21C-32, 2002.

P.F. Banzon, R.H. Evans, **H.R. Gordon**, and R.M. Chomko, Application of the Spectral Matching Algorithm to Recover Chlorophyll Time Series During the Arabian Sea Southwest Monsoon, Eos. Trans. AGU, 83(4), Ocean Sciences Meet. Suppl., Abstract OS12I-04, 2002.

W.M. Balch, **H.R. Gordon**, B.C. Bowler, D.T. Drapeau, J. Goes, and E. Booth, Suspended Chalk and Ocean Optics, *Ocean Optics XVI*, Santa Fe, NM, November 18-22, 2002.

J. Cedric, S. Thiria, B. Galios, M. Crapon, C. Moulin, and **H.R. Gordon**, Use of a Neural Network Approach to Improve atmospheric Correction of Ocean Color Imagery, *Ocean Optics XVI*, Santa Fe, NM, November 18-22, 2002.

P.F. Banzon, R.H. Evans, **H.R. Gordon**, and R.M. Chomko, Application of the Spectral Matching Algorithm to Arabian Sea SeaWiFS Imagery, *Ocean Optics XVI*, Santa Fe, NM, November 18-22, 2002.

Balch, W. M., H. Gordon, B. Bowler, D. Drapeau, J. Goes, and E. Booth. 2002. Suspended chalk and ocean optics. Ocean Optics XVI. Presented November 2002.

Goes, J. I., **W. M. Balch**, J. Vaughn. Optical properties of submicron particles in seawater using flow field flow fractionation. Ocean Optics XVI. Presented November 2002.

Balch, W. M., Plueddemann, A. Pilskaln, C., Dam, H., McManus, G. 2002. Chalk-Ex: An Ocean Optics Manipulation Experiment on the Fate of Calcite Particles. Presented at the December ’02 AGU Meeting in San Francisco.

Bowler, B., **W. M. Balch**, D. Drapeau, J. Goes, and E. Booth. 2002. Optical Results From the November ’01 “Chalk-Ex” Ocean Optics Manipulation Experiment. Presented at the December ’02 AGU Meeting in San Francisco.

Plueddemann, A. J., **W.M. Balch**, C.H. Pilskaln. 2002. Evolution of stratification and shear during ChalkEx-2001. Presented at the December ’02 AGU Meeting in San Francisco.

Goes, J. I., **W.M. Balch**, B. Bowler, D. Drapeau, E. Booth. 2002. Evidence of DOM removal by Cretaceous CaCO3 particles during Chalk-Ex 2001. Presented at the December ’02 AGU Meeting in San Francisco.

Publications (2002):

(NAS5-31363 Personnel bold highlighted)

Balch, W.M., Vaughn, J.M., Novotny, J.F., Drapeau, D.T., Goes, J.I., Lapierre, J.M., Scally, E, Vining, C.L., Ashe, A., and Vaughn, J.M. Jr. 2002. Fundamental changes in light scattering associated with infection of marine bacteria by bacteriophage. **Limnology and Oceanography**. 47(5): 1554-1561.

Campbell, J.W., D. Antoine, R. Armstrong, K. Arrigo, **W. Balch**, and others. 2002. Comparison of algorithms for estimating ocean primary productivity from surface chlorophyll, temperature, and irradiance. **Global Biogeochemical.Cycles**, 16(3), (10.1029 / 2001GB001444).

Quinn, P. K. , D.J. Coffman, T.S. Bates, T.L. Miller, J.E. Johnson, **E.J. Welton**, C. Neusüss, M. Miller, and P. J. Sheridan, Aerosol Optical Properties during INDOEX 1999: Means, Variability, and Controlling Factors, *Journal of Geophysical Research*, 107**D**(19) 19-1—19-25, 2002. (10.10029/2000JD000037).

Welton, E.J., K. J. Voss, P. K. Quinn, P.J. Flatau, K. Markowicz, J.R. Campbell, J.D. Spinhirne, **H.R. Gordon**, J. Johnson, Measurements of aerosol vertical profiles and optical properties during INDOEX 1999 using micro-pulse lidars. *J. Geophys. Res.*, **107D**, 18-1—18-20, 2002. (10.1029/2000JD000038)

M. Wang and **H.R. Gordon**, Calibration of ocean color scanners:How much error is acceptable in the near infrared?, *Remote Sensing of Environment* **82,** 497—504, 2002.

R.M. Chomko, **H. R. Gordon**, S. Maritorena, D.A. Siegel, Simultaneous retrieval of oceanic and atmospheric parameters for ocean color imagery by spectral optimization: A validation, *Remote Sensing of Environment* **84,** 208—220, 2003.

C. Cattrall, K.L. Carder, K.T. Thome, **H.R. Gordon**, Solar-reflectance-based calibration of spectral radiometers, *Geophys. Res. Lett.*, **29**, 2-1—2-4, 2002. (10.1029/2002GL015130)

H.R. Gordon, Comment on "Pitfalls in atmospheric correction of ocean color imagery: how should aerosol optical properties be computed?" *Applied Optics*, (In Press).

Other Works Submitted or in Preparation

Broerse, A.T.C., Tyrrell, T., Young, J. R., Poulton, A. J., Merico, A. and **W. M. Balch**. The cause of bright waters in the Bering Sea in winter. 2002 Submitted to *Cont. and Shelf Research*

Balch, W. M., D. Drapeau, B. Bowler, E. Booth, J. Goes, A. Ashe, and J. Frye. A multi-year record of optical properties in the Gulf of Maine: I. Spatial and temporal variability. To be submitted to *Progress in Oceanography*.

Balch, W. M., D. Drapeau, B. Bowler, E. Booth, J. Goes, A. Ashe, and J. Frye. A multi-year record of optical properties in the Gulf of Maine: II. Connections between optics and hydrography. To be submitted to *Journal of Plankton Research*.

Vaillancourt, R.D., C.W. Brown, R.R.L. Guillard, **W. M. Balch**. Submitted. Light backscattering by phytoplankton algae and a heterotrophic bacterium measured with a multi-wavelength, fixed-angle backscattering meter. To be submitted *Jour. Geophys. Res.*

APPENDIX I

An Algorithm for Coastal Water and the Status of its Implementation into the MODIS Processing Stream

by

Howard.R. Gordon and Roman. M Chomko,
Department of Physics
University of Miami
Coral Gables, FL 33124

R.E. Evans, J.W. Brown, S. Walsh and W. Baringer
RSMAS
University of Miami
Miami, FL 33146

An Algorithm for Coastal Water and the Status of its Implementation into the MODIS Processing Stream

by

Howard.R. Gordon and Roman. M Chomko,
Department of Physics
University of Miami
Coral Gables, FL 33124

R.E. Evans, J.W. Brown, S. Walsh and W. Baringer
RSMAS
University of Miami
Miami, FL 33146

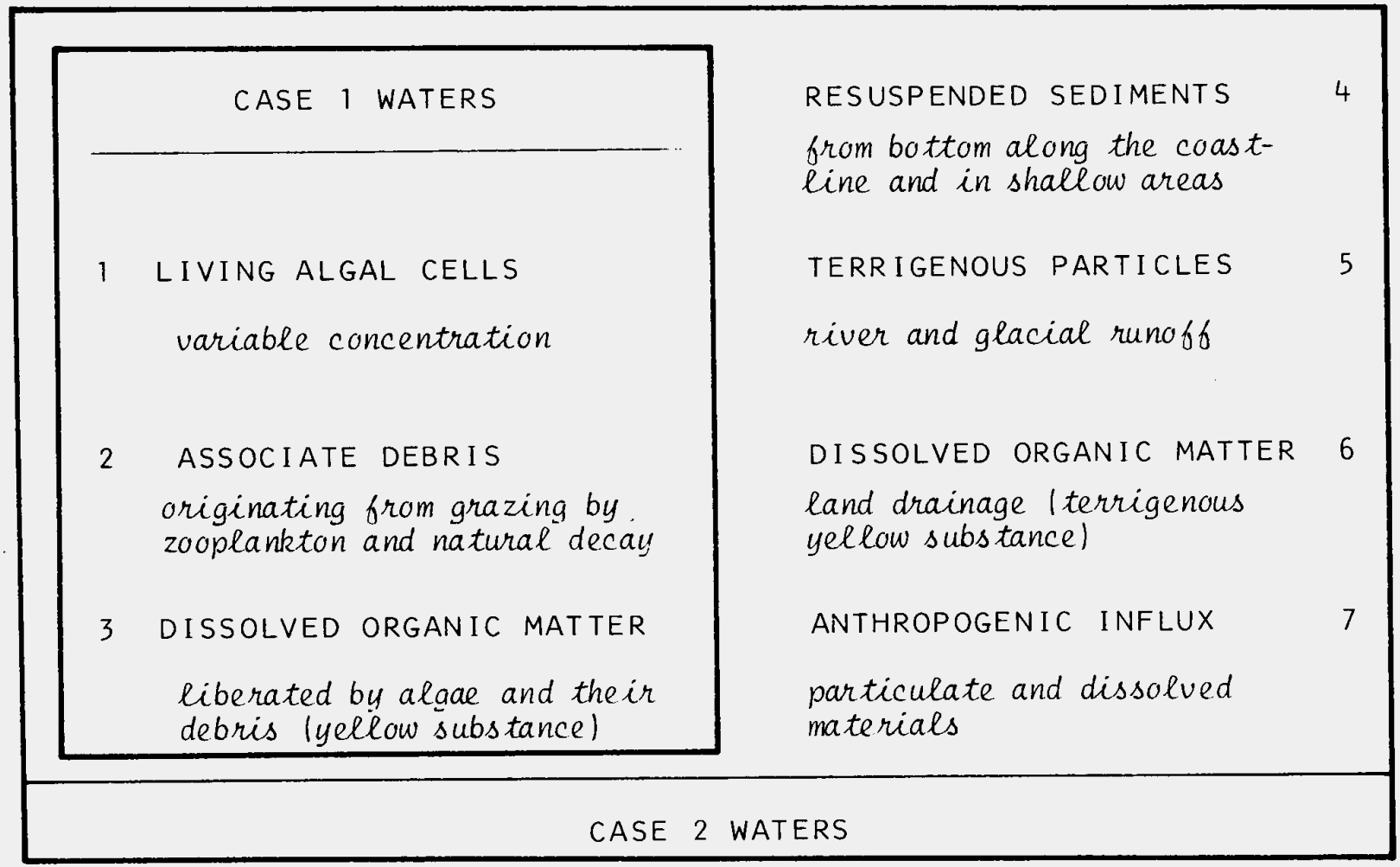

(Gordon and Morel, 1983)

Atmospheric Correction

$$\rho_t(\lambda) = \rho_r(\lambda) + \rho_A(\lambda) + t_v(\lambda)t_s(\lambda)\rho_w(\lambda)$$

Case 1 waters:

- $\rho_w(765) \approx \rho_w(865) \approx 0, \Rightarrow$ NIR can be used to assess the aerosol influence.

Case 2 waters:

- $\rho_w(\text{NIR}) \neq 0, \Rightarrow$ no bands "tailor made" for assessing the aerosol.
- Case 2 waters contain large quantities of dissolved organic material that influence ρ_t in a manner similar to strongly-absorbing aerosols.
- Strongly absorbing aerosols are often found near the coast.

Approach for Case 2 waters: model $\rho_A(\lambda)$ and $\rho_w(\lambda)$, and then use spectral optimization to find the best values of the model parameters.

The Aerosol Model

Uses a Junge Power-Law Size Distribution:

$$\frac{dN}{dD} = 0\,,\ D < D_0,$$

$$\frac{dN}{dD} = \frac{K}{D_1^{\nu+1}}\,,\ D_0 \le D \le D_1,$$

$$\frac{dN}{dD} = \frac{K}{D^{\nu+1}}\,,\ D_1 \le D \le D_2,$$

$$\frac{dN}{dD} = 0\,,\ D > D_2,$$

$D_0 = 0.06$ μm, $D_1 = 0.20$ μm, and $D_2 = 20$ μm.

Mie theory is used to compute aerosol properties

- $m = m_r - im_i$, where m_r is either 1.50 or 1.333, and m_i = 0, 0.001, 0.003, 0.010, 0.030, and 0.040.
- ν ranges from 2.0 to 4.5 in steps of 0.5.
- 72 separate aerosol models (2 values of m_r × 6 values of m_i × 6 values of ν).

$$\rho_A(G,\lambda,m_r,m_i,\nu) = a(G,\lambda,m_r,m_i,\nu)\tau(\lambda) + b(G,\lambda,m_r,m_i,\nu)\tau^2(\lambda) + c(G,\lambda,m_r,m_i,\nu)\tau^3(\lambda) + d(G,\lambda,m_r,m_i,\nu)\tau^4(\lambda)$$

- Interpolate to essentially give a continuum of models.

The Water Model
(Garver and Siegel, 1997)

$$\rho_w = \rho_w(b_b/(a+b_b))$$

$$a = a_w + a_{ph} + a_{cdm}$$
$$b_b = b_{bw} + b_{bp}$$

$$a_{ph}(\lambda) = a_{ph0}(\lambda)\ C$$
$$a_{cdm}(\lambda) = a_{cdm}(443)\ \exp[-S(\lambda-443)\}]$$
$$b_{bp}(\lambda) = b_b(443)\ [443/\lambda]^n$$

$$\rho_w = \rho_w(\lambda, C, a_{cdm}(443), b_{bp}(443))$$

Note, the parameters $a_{ph0}(\lambda)$, S, and n are provided by fitting the model to experimental data. For Case 1 waters, $S = 0.0206$ nm^{-1} and $n = 1.03$ (Maritorena, *et al.*, 2002).

The Optimization

$$\rho_t(\lambda) = \rho_r(\lambda) + \rho_A(\lambda) + t_v(\lambda) t_s(\lambda) \rho_w(\lambda),$$

$$\rho_{Aw}(G, \lambda, measured) \equiv \rho_A(G, \lambda) + t_v(G, \lambda) t_s(G, \lambda) \rho_w(\lambda).$$

The modeled counterpart of ρ_{Aw} is

$$\hat{\rho}_{Aw}(G, \lambda, m_r, m_i, \nu, \tau_a, C, a_{cdm}(443), b_{bp}(443)) \equiv \hat{\rho}_A(G, \lambda, m_r, m_i, \nu, \tau_a)$$
$$+ \hat{t}_v(G, \lambda, m_r, m_i, \nu, \tau_a) \hat{t}_s(G, \lambda, m_r, m_i, \nu, \tau_a)\, \hat{\rho}_w(\lambda, C, a_{cdm}(443), b_{bp}(443)).$$

Assuming $\rho_A(765)$ and $\rho_A(865) = 0$ gives estimation of the parameters ν and τ_a as functions of m_r and m_i, i.e., $\nu(m_r, m_i)$ and $\tau_a(m_r, m_i)$.

Given the constraints $\nu(m_r, m_i)$ and $\tau_a(m_r, m_i)$ we minimize the quantity

$$\sum_{\lambda_i} \left\{ \hat{\rho}_{Aw}(G, \lambda_i, m_r, m_i, \nu, \tau_a, C, a_{cdm}(443), b_{bp}(443)) - \rho_{Aw}(G, \lambda_i, measured) \right\}^2$$

In effect, we have optimized for 7 parameters:

C, $a_{cdm}(443)$, $b_{bp}(443)$, ν, τ_a, m_r, and m_i;

This is generally all that is needed in Case 1 waters.

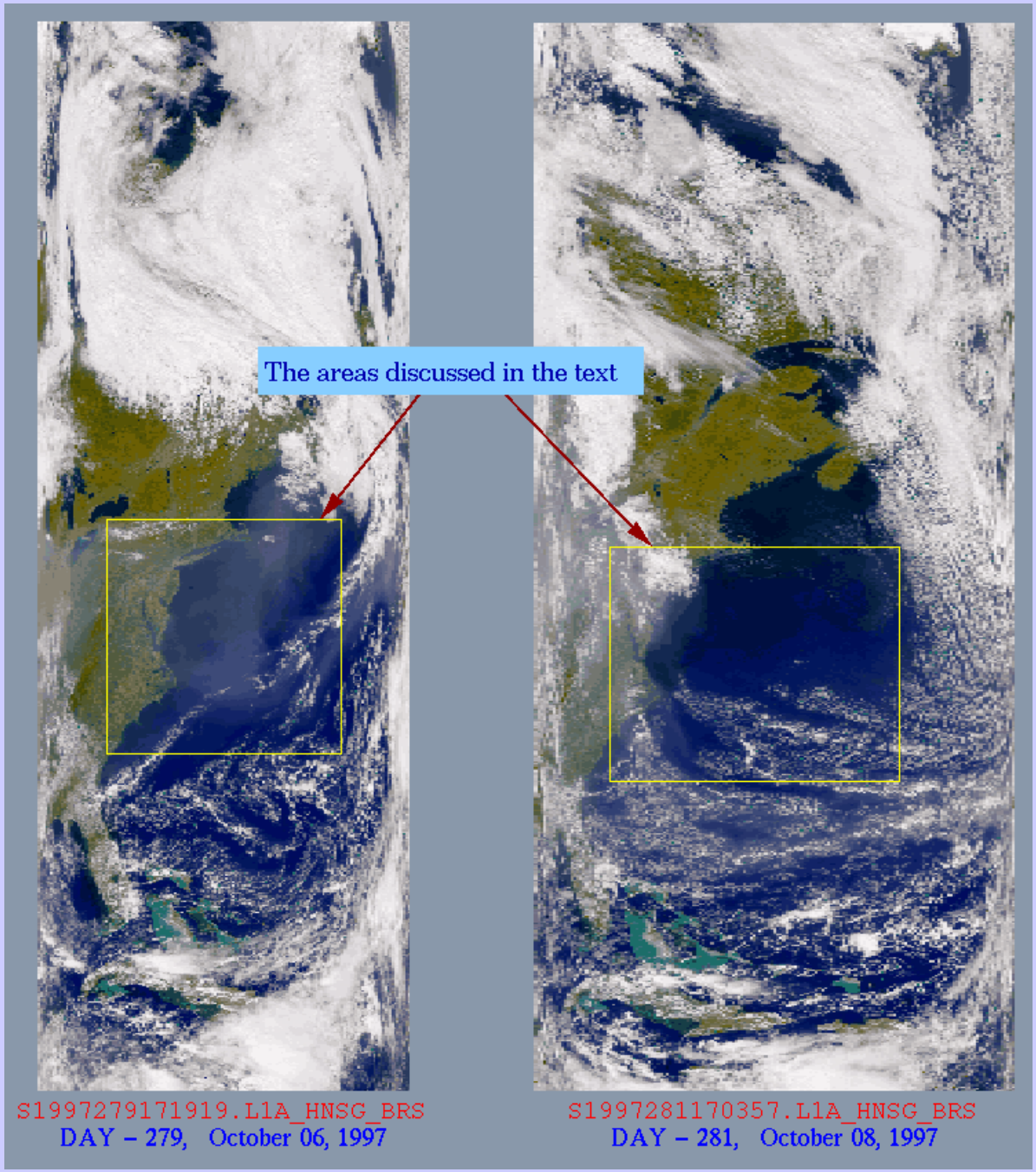
The areas discussed in the text
S1997279171919.L1A_HNSG_BRS
DAY – 279, October 06, 1997
S1997281170357.L1A_HNSG_BRS
DAY – 281, October 08, 1997

To validate this algorithm, we use the SeaWiFS image from Day 279 (left on previous slide) and compare the retrievals of a_{cdm} from the algorithm with estimates of a_{CDOM} from the AOL. The AOL measurements are made along the triangular path drawn on the next two images.

SOA $a_{cdm}(443)$ (m^{-1})

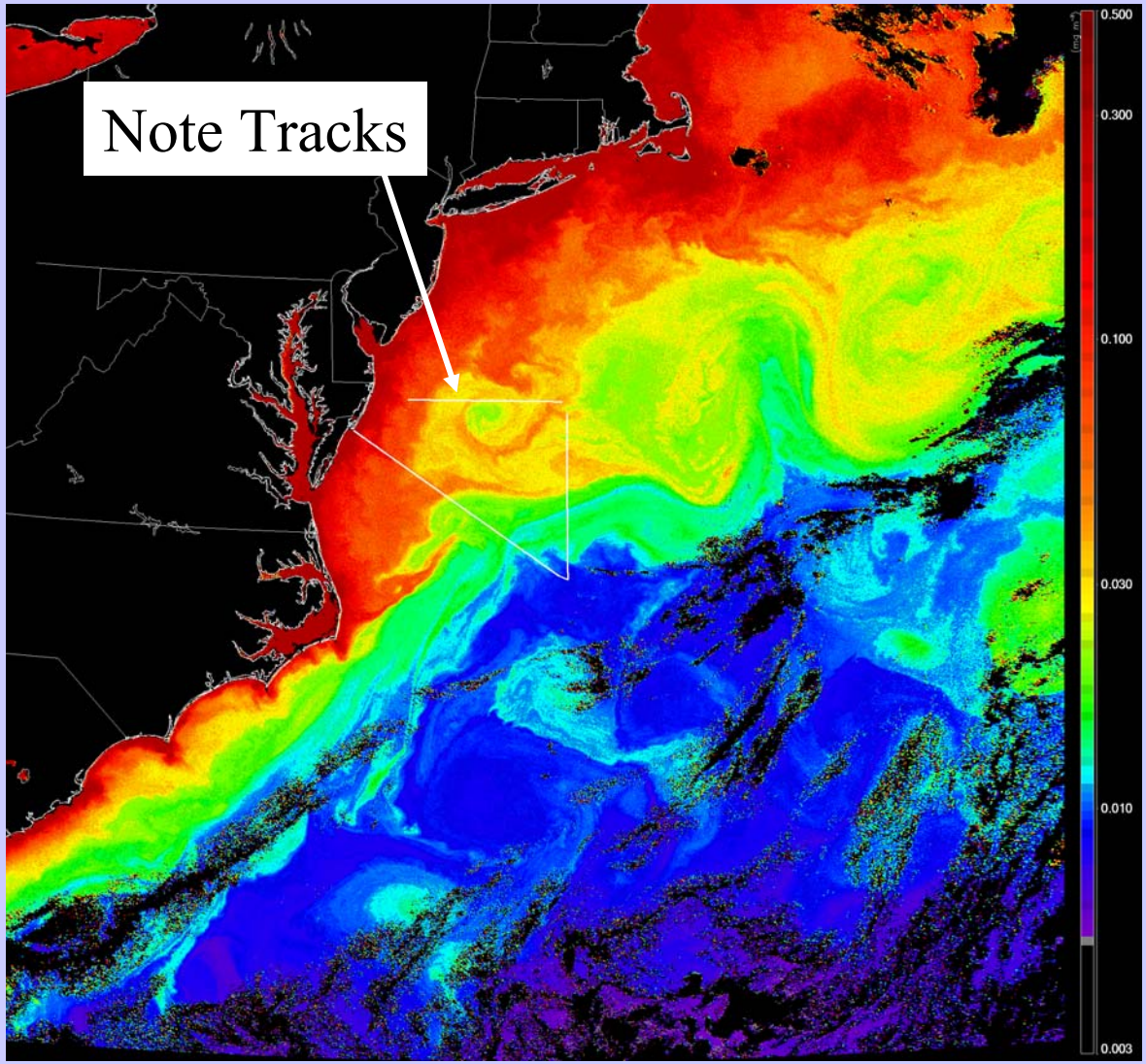

SOA $a_{cdm}(443)$ (m^{-1})

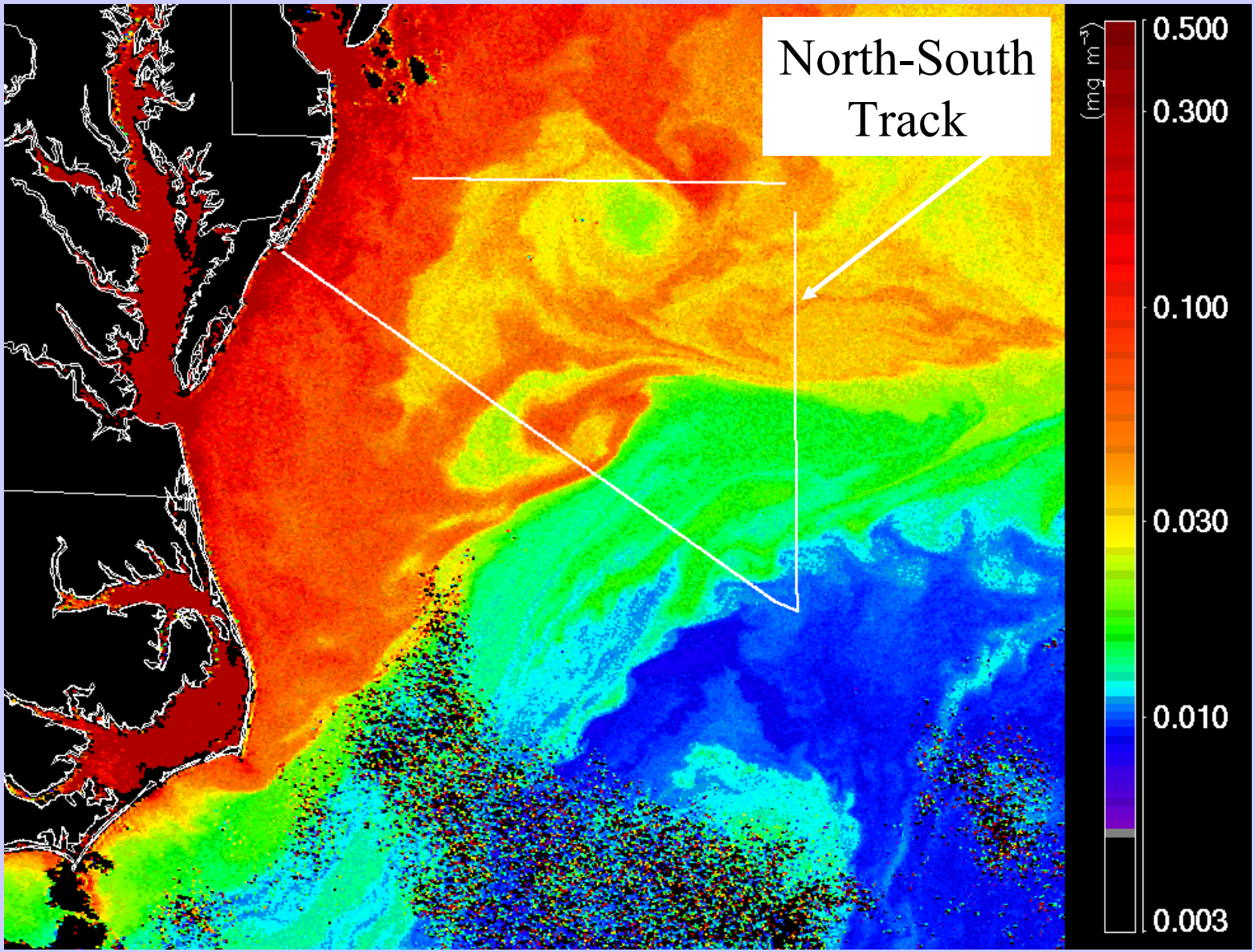

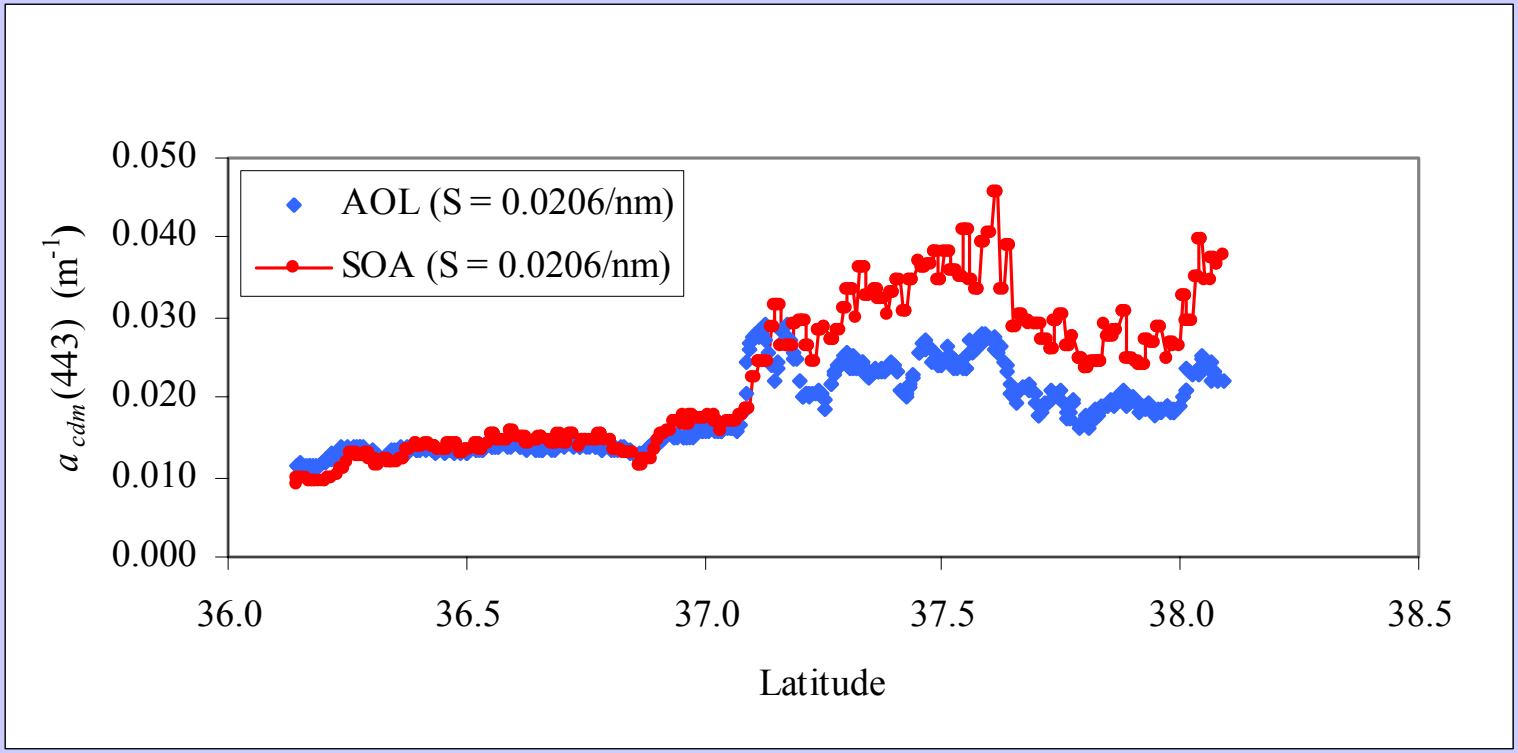

Comparison of SOA and AOL $a_{cdm}(443)$ along the North-South Track

The value of S required to bring the SOA retrieved $a_{cdm}(443)$ into confluence with the AOL-retrieved $a_{CDOM}(443)$ at each point along the track the track was determined and shown in the next slide. The resulting S values show a clear trend of decreasing into the mesotrophic waters as would be expected (Green and Blough, 1994). Similar results are found for the other two tracks.

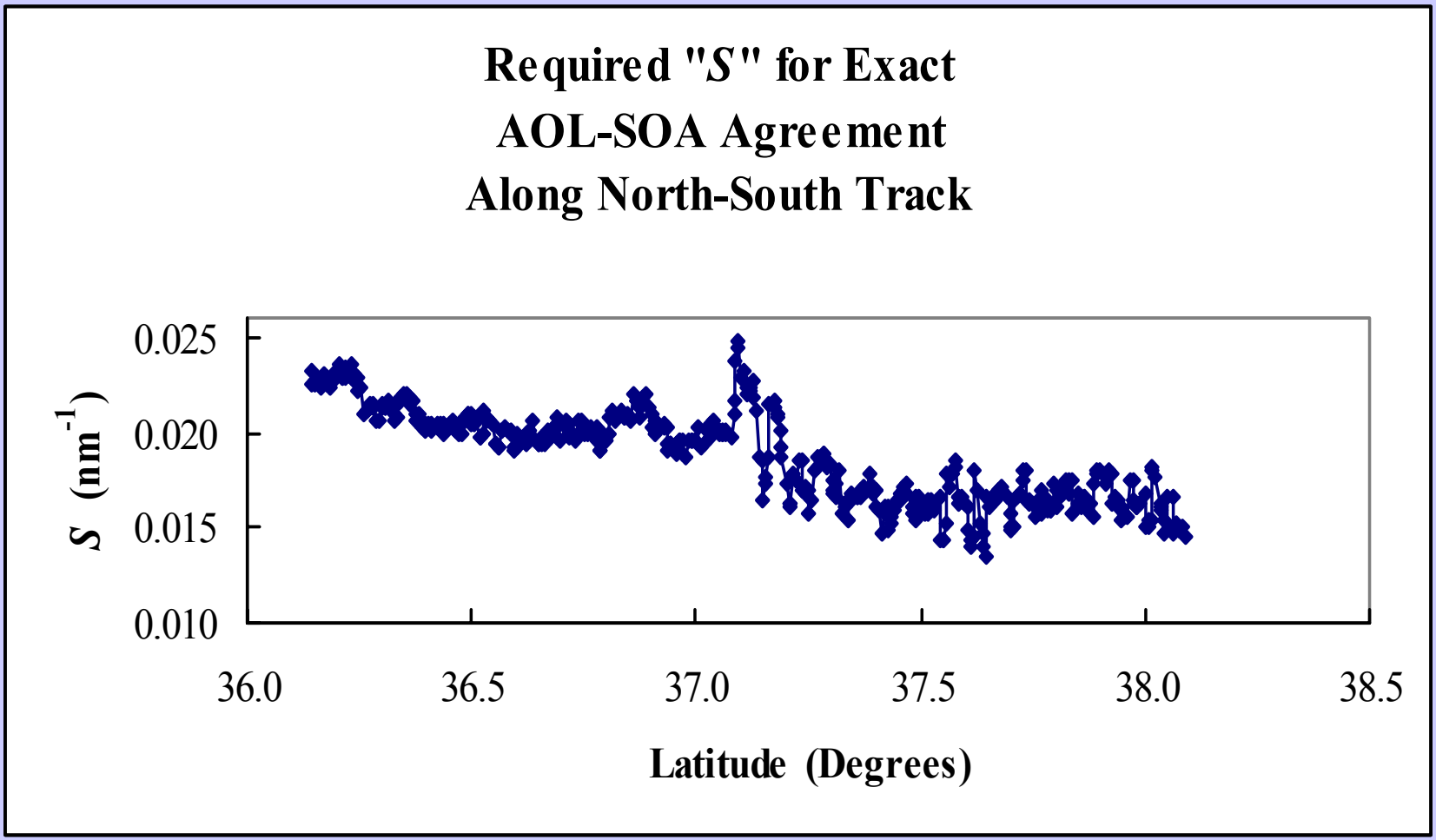
Required "S" for Exact
AOL-SOA Agreement
Along North-South Track
S (nm-1)
0.025
0.020
0.015
0.010
36.0
36.5
37.0
37.5
38.0
38.5
Latitude (Degrees)

SOA *Chl a* (mg/m^3)

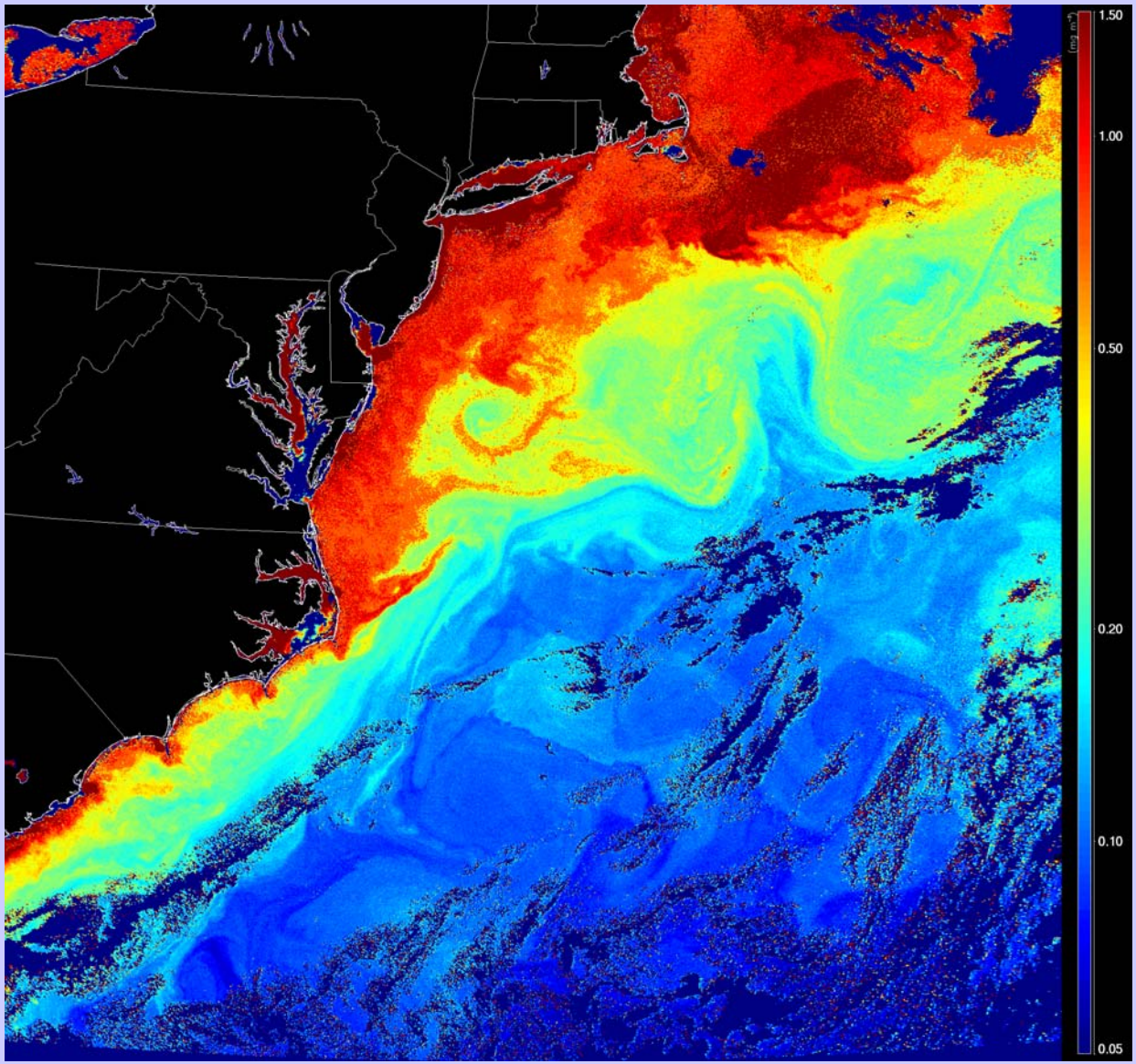

1.50

1.00

0.50

0.10

SeaWiFS 8-day mean *Chl a*

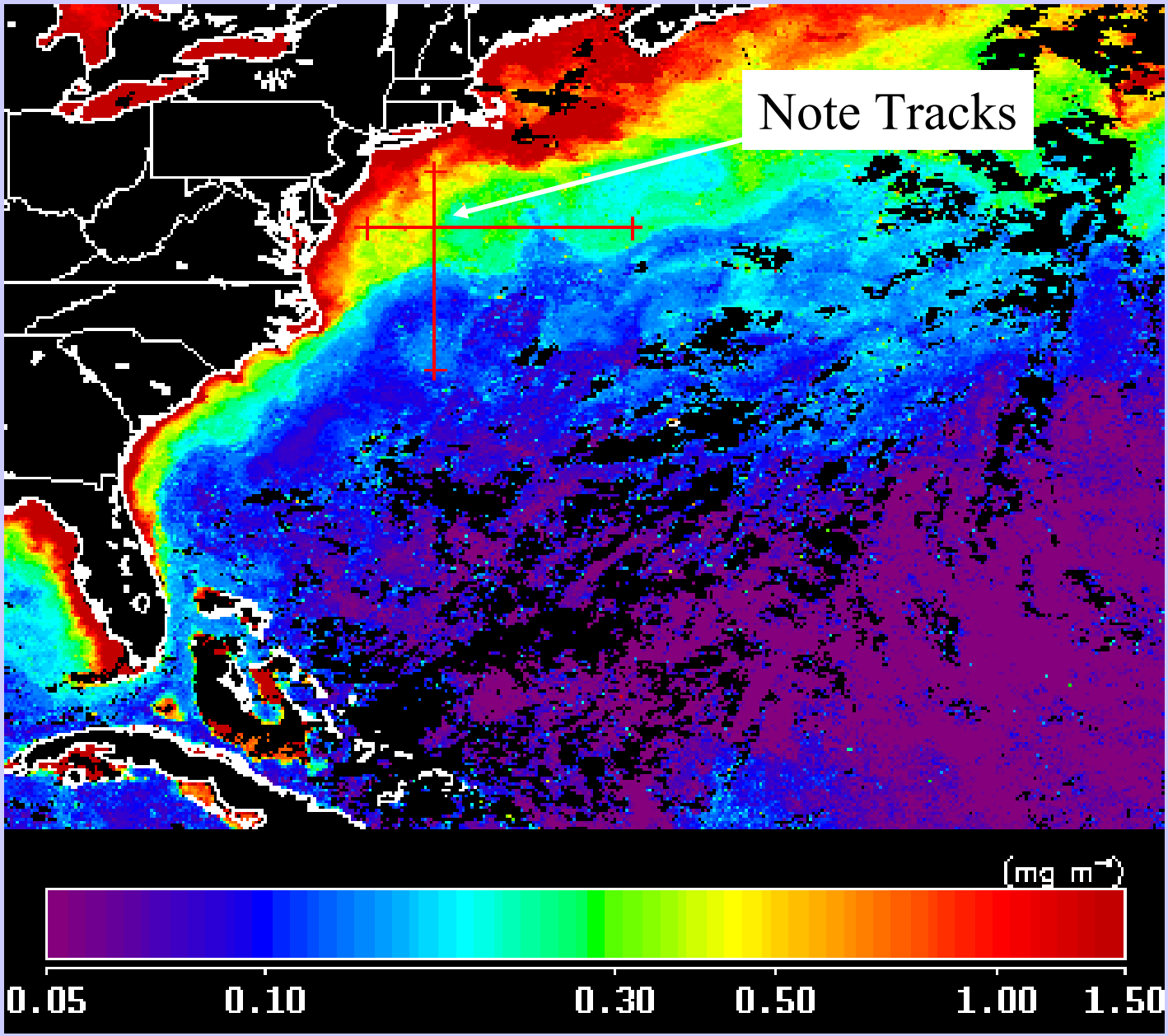

Comparison with SeaWiFS

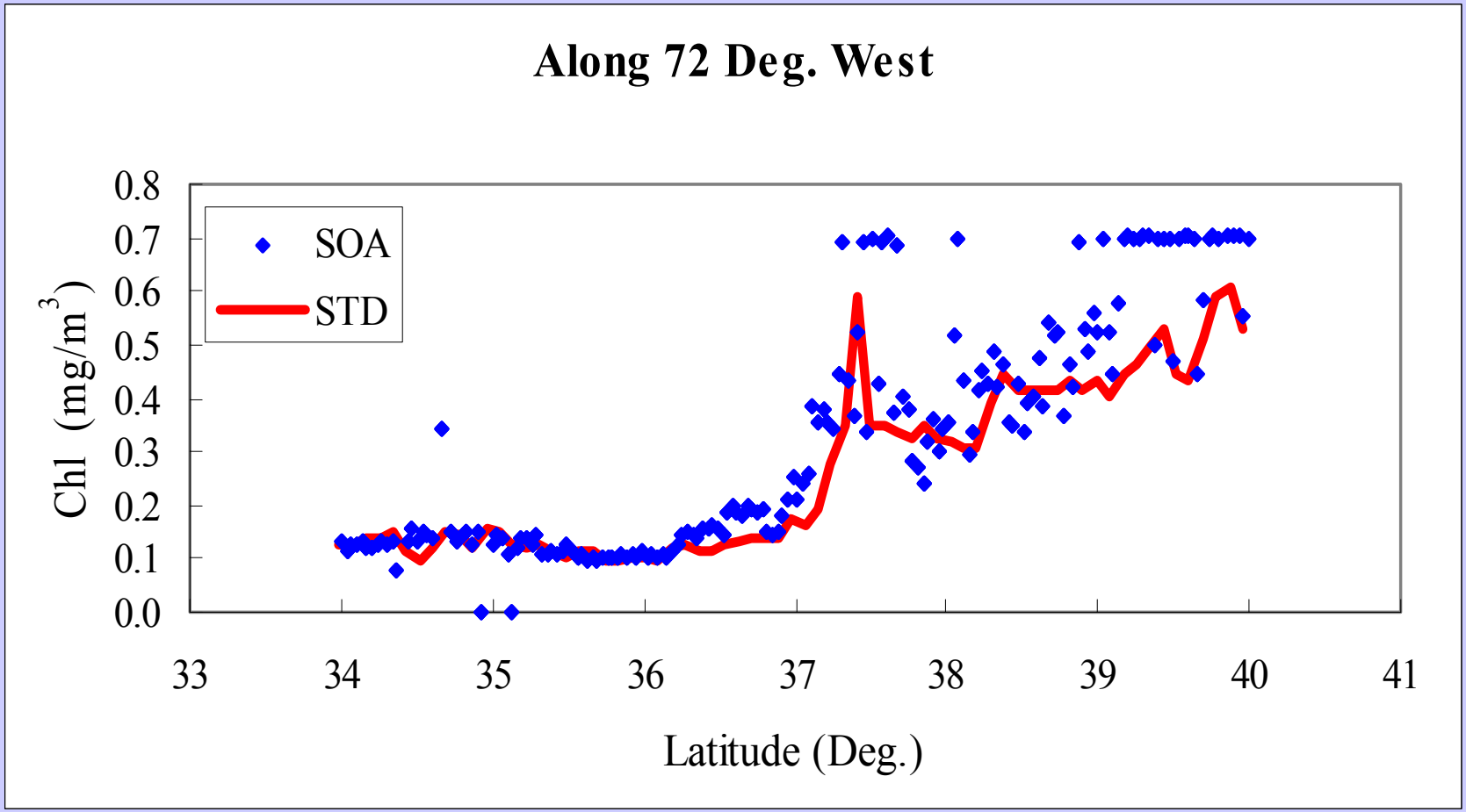

Comparison with SeaWiFS

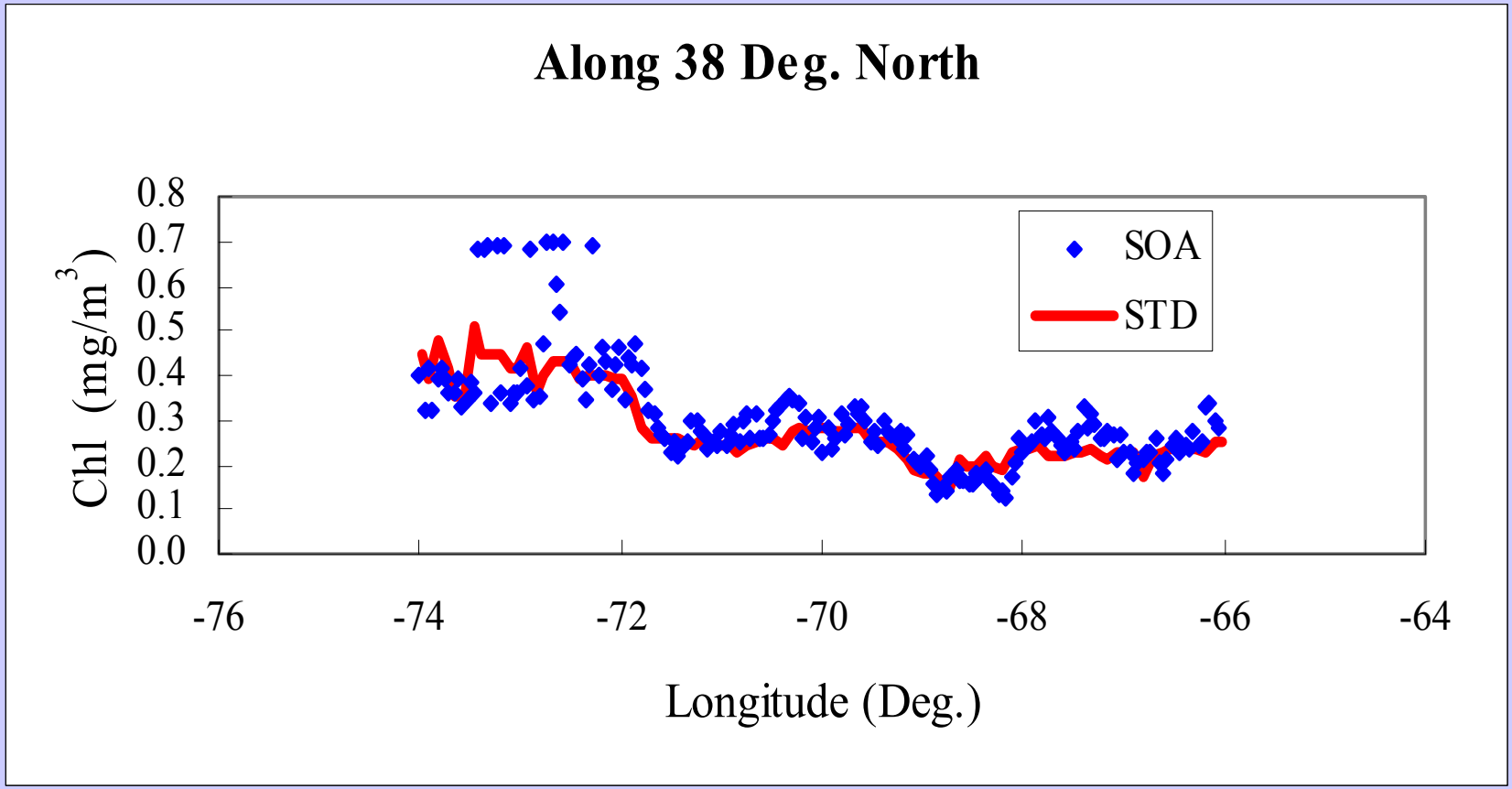

$b_{bp}(443)$ (m^{-1})

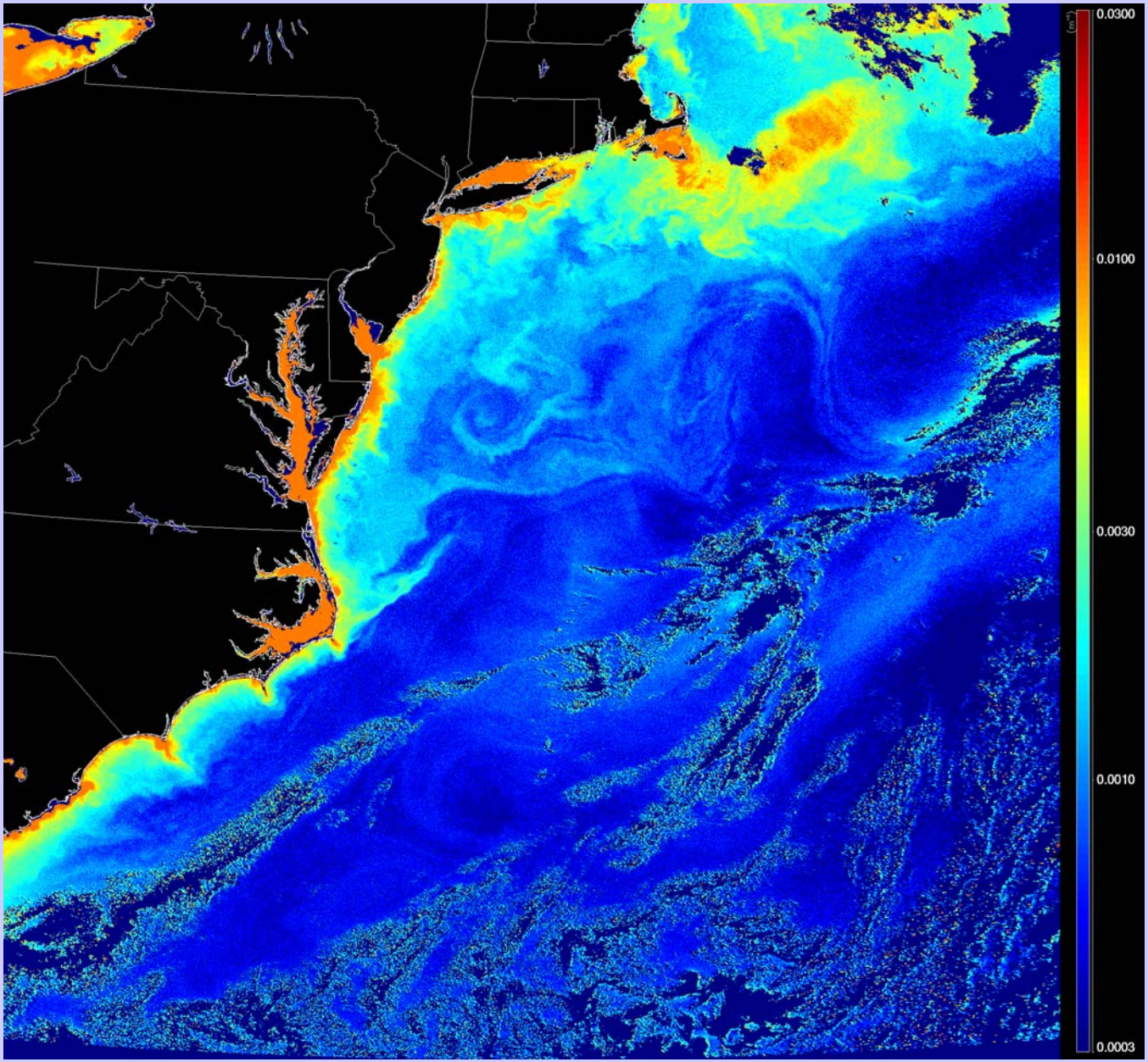

ν

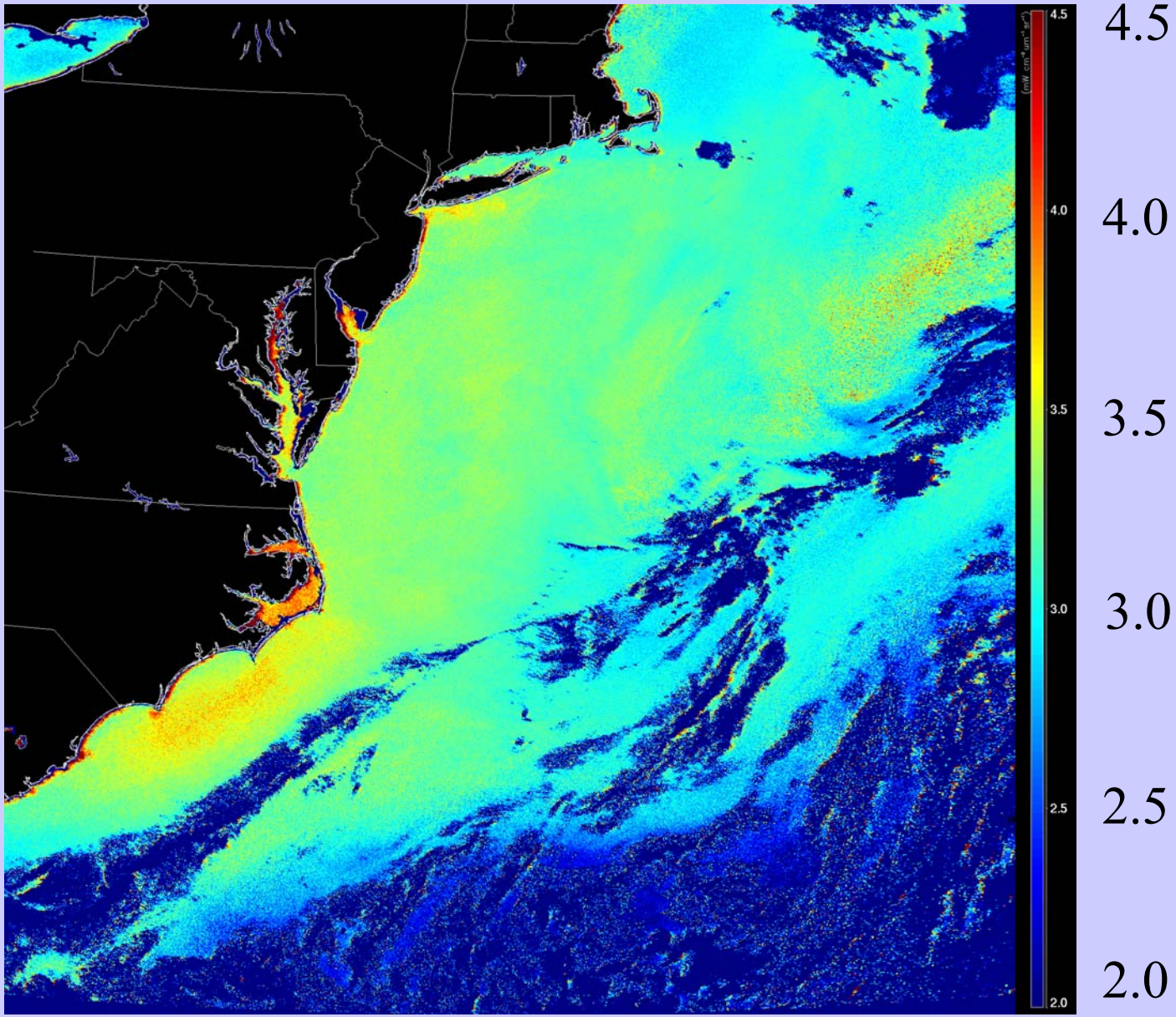

ω_0

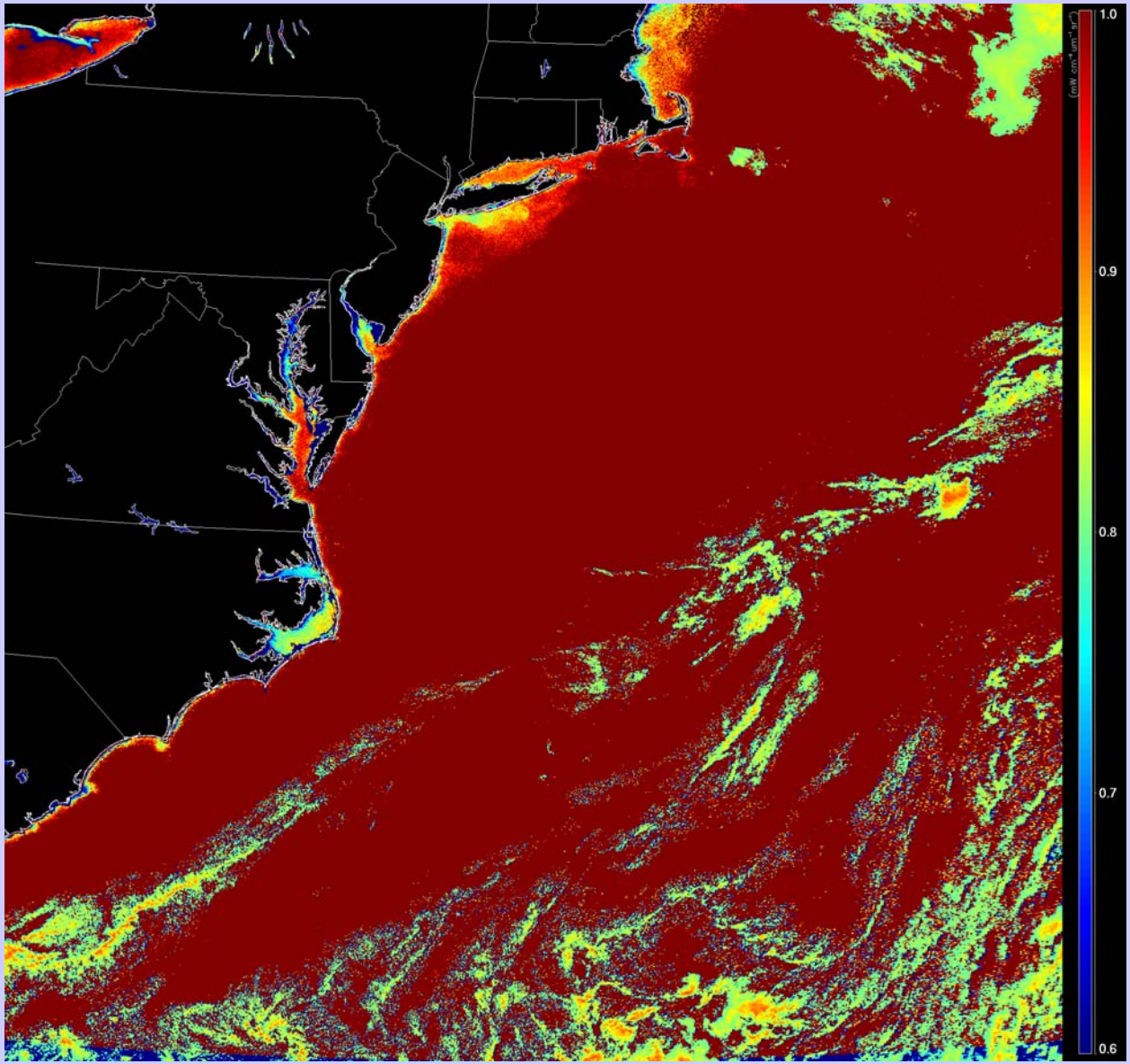

Extension to Case 2 Waters

- In Case 2 waters, we operate the algorithm as in Case 1 waters, i.e., assuming that $\rho_w(NIR) = 0$.

- Then we use the retrieved values of C, $a_{cdm}(443)$, and $b_{bp}(443)$ to provide an estimate of ρ_w in the NIR, and the retrieved values of ν, τ_a, m_r, and m_i to estimate t_v and t_s and the NIR.

- These estimates are subtracted from the total, i.e.,

$$\rho_t(\lambda_{NIR}) - t_v(\lambda_{NIR}) t_s(\lambda_{NIR}) \rho_w(\lambda_{NIR}) = \rho_r(\lambda_{NIR}) + \rho_A(\lambda_{NIR}).$$

- The $\nu - \tau_a$, portion of the algorithm is then operated with

$$\rho_t(\lambda_{NIR}) - t_v(\lambda_{NIR}) t_s(\lambda_{NIR}) \rho_w(\lambda_{NIR}),$$

instead of $\rho_t(\lambda_{NIR})$, to estimate new constraints $\nu(m_r, m_i)$ and $\tau_a(m_r, m_i)$, and to initiate a new optimization, etc.

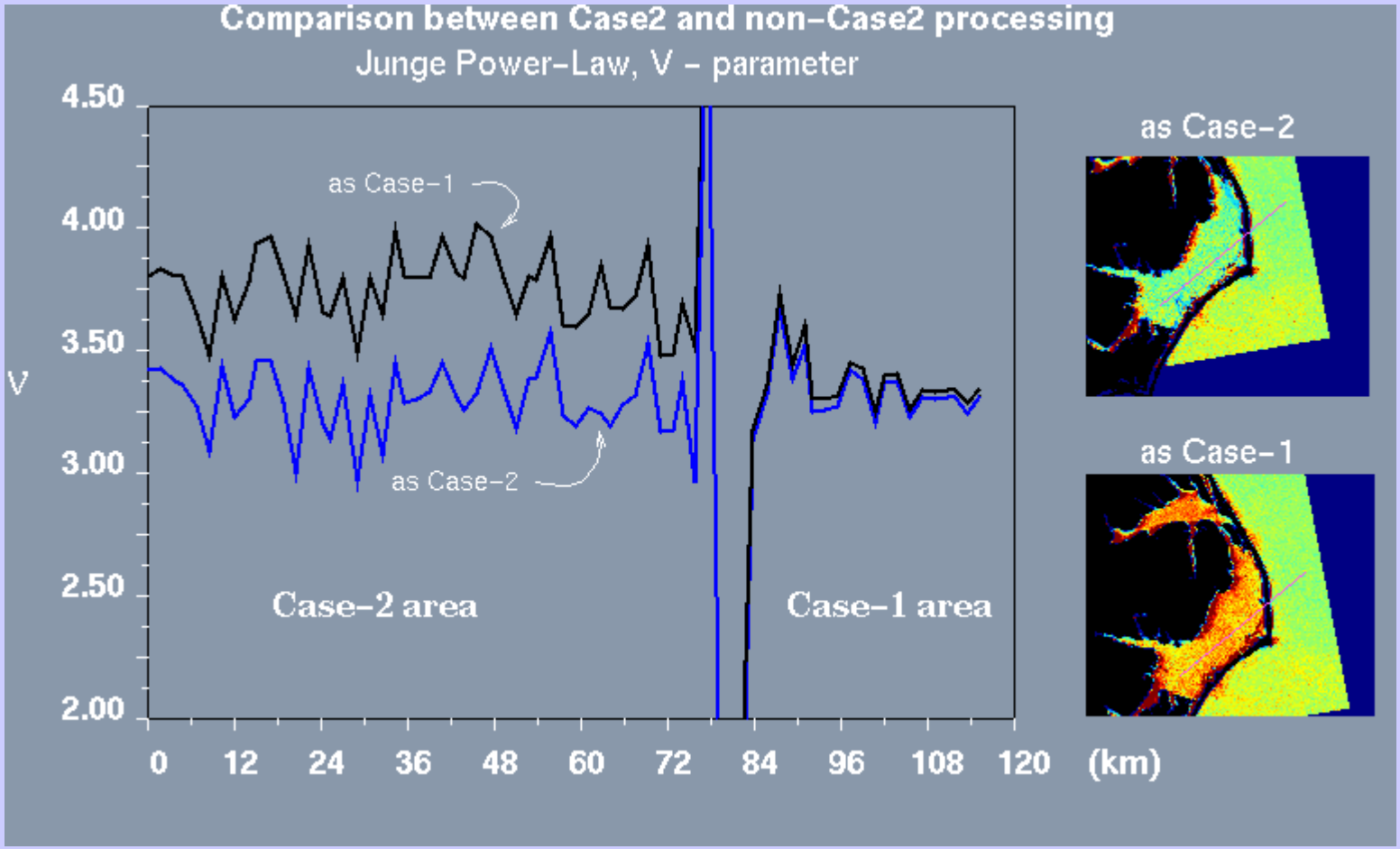
Comparison between Case2 and non-Case2 processing
Junge Power-Law, V - parameter
4.50
4.00
3.50
3.00
2.50
2.00
V
as Case-1
as Case-2
Case-2 area
Case-1 area
0
12
24
36
48
60
72
84
96
108
120
(km)
as Case-2
as Case-1

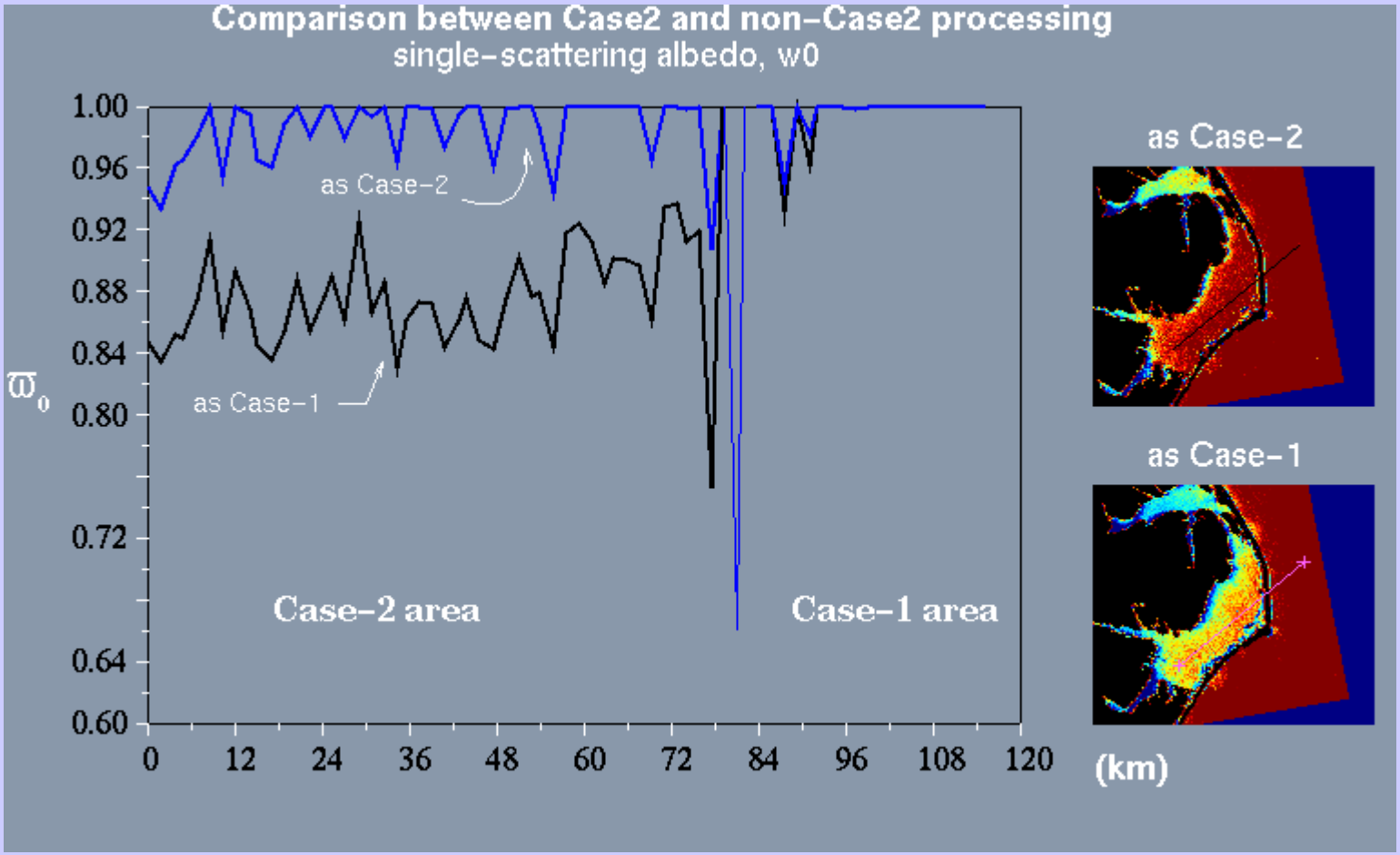
Comparison between Case2 and non-Case2 processing
single-scattering albedo, w0
1.00
0.96
0.92
0.88
0.84
0.80
0.72
0.64
0.60
ϖ0
as Case-2
as Case-1
Case-2 area
Case-1 area
0
12
24
36
48
60
72
84
96
108
120
(km)
as Case-2
as Case-1

Incorporation into the MODIS Code: A Status Report

Processing philosophy

- Spectral Optimization Algorithm is slow, so at present we must restrict application to sub-granuals.

- Unlike the Case 1 $\rho_w(\lambda)$ model, the Case 2 $\rho_w(\lambda)$ model will most likely be site specific, i.e., the parameters in the GS97 model $\{a_{ph0}(\lambda), S, \text{and } n\}$ will depend on the target location.

- Our goal is to provide processing code that can be used for any location, given model parameters for that location. Individual investigators must supply $a_{ph0}(\lambda)$, S, and n.

b_{bp} (m^{-1})

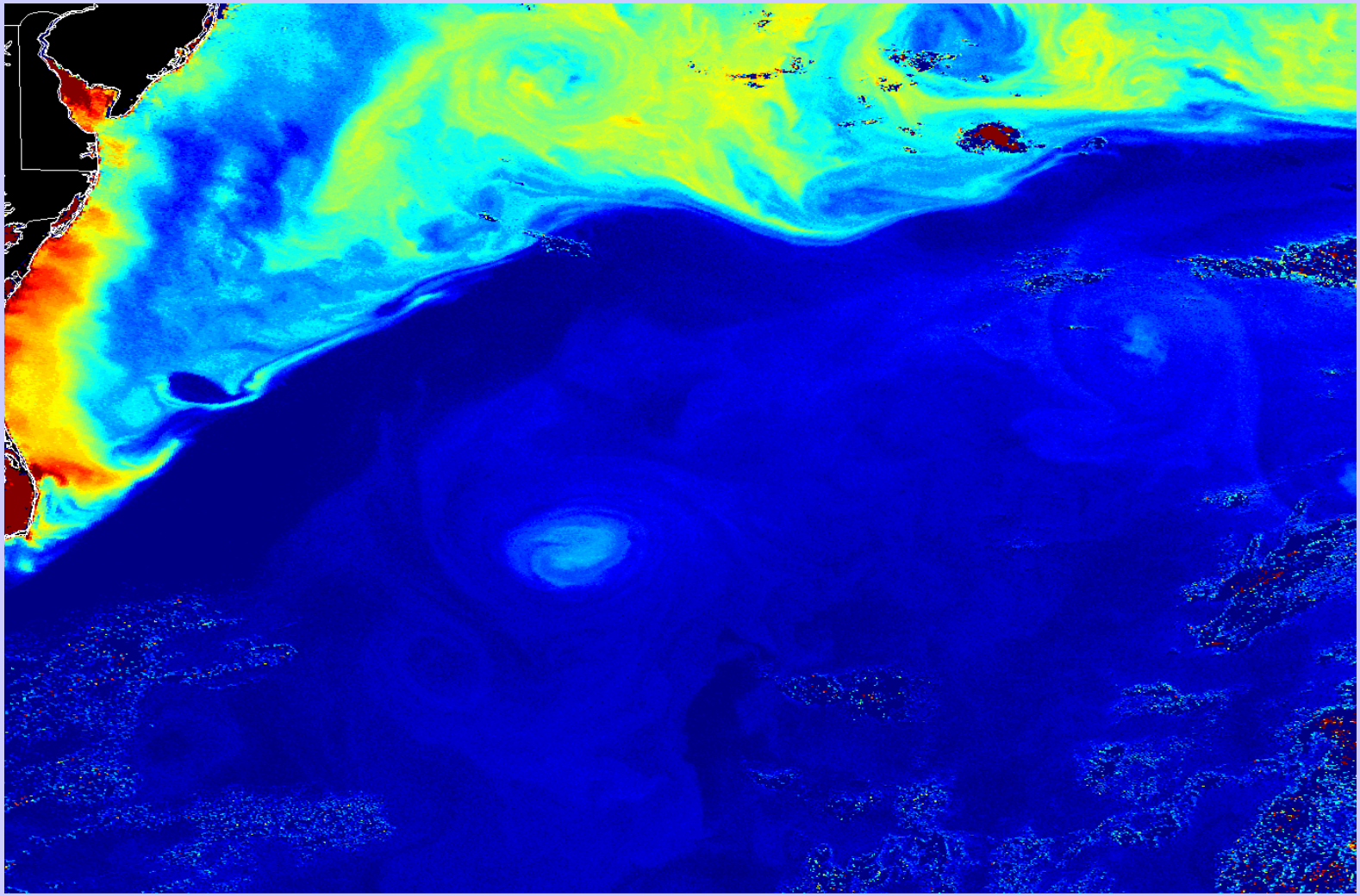

SeaWiFS

$b_{bp}\,(\mathrm{m}^{-1})$

SeaWiFS

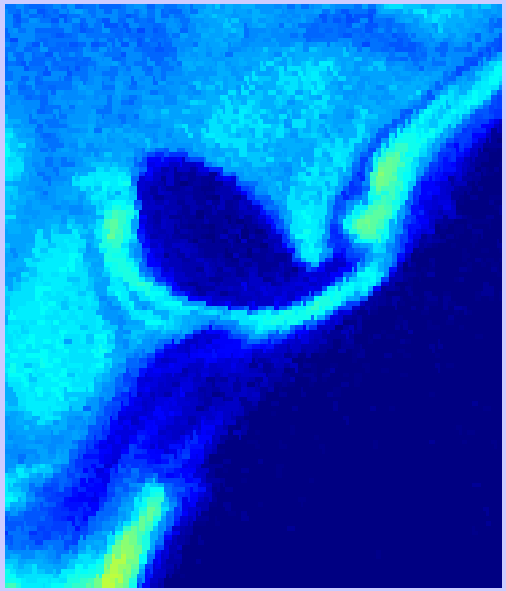

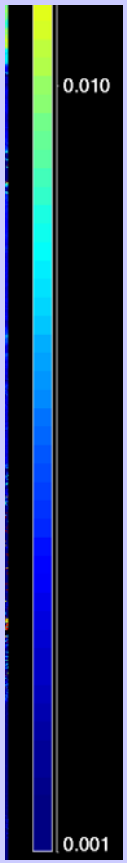

MODIS

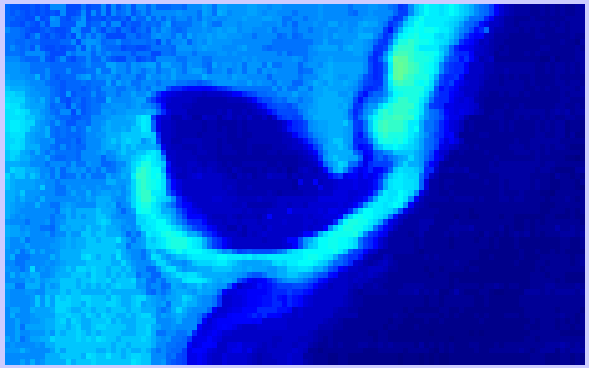

b_{bp} (m^{-1})

SeaWiFS

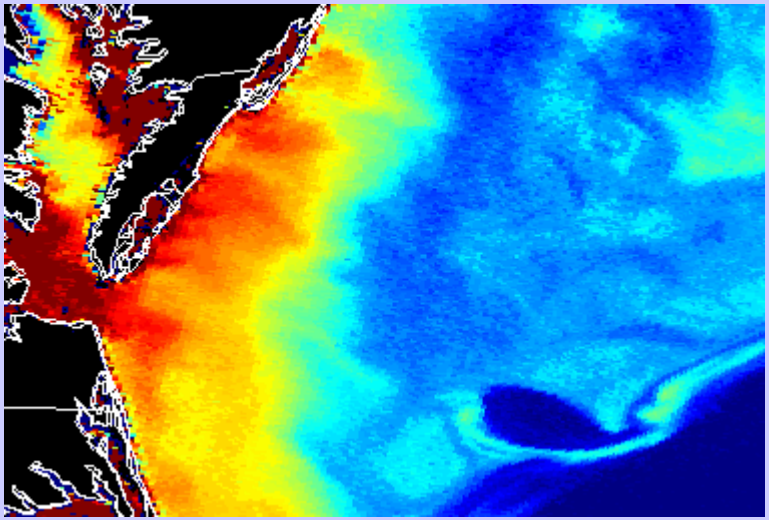

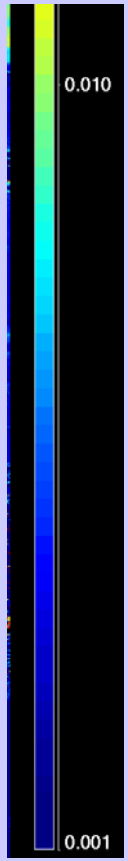

MODIS

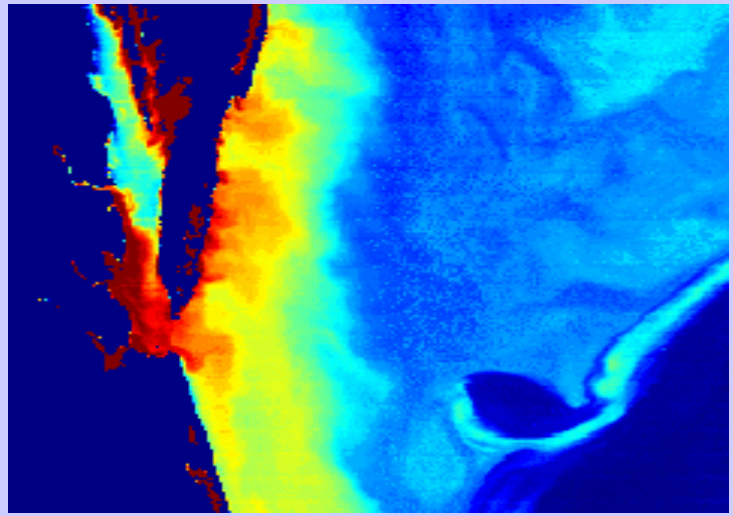

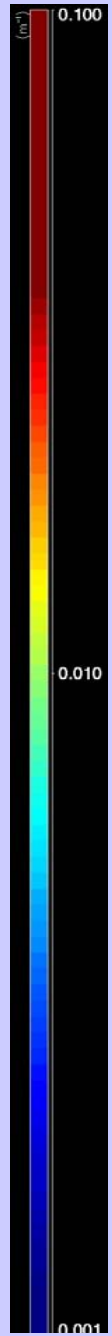

a_{cdm} (m^{-1})

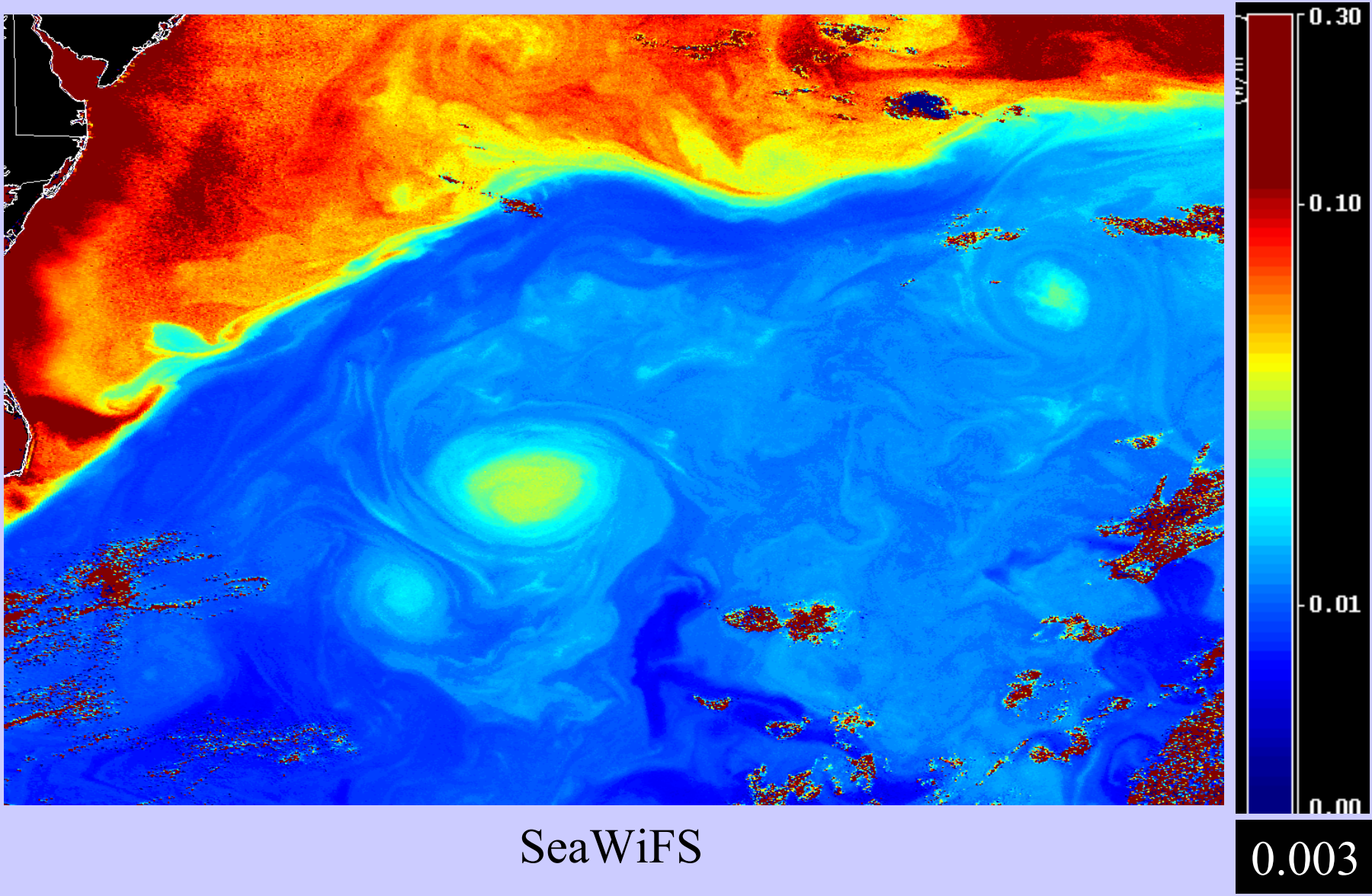

SeaWiFS

0.003

a_{cdm} (m^{-1})

SeaWiFS

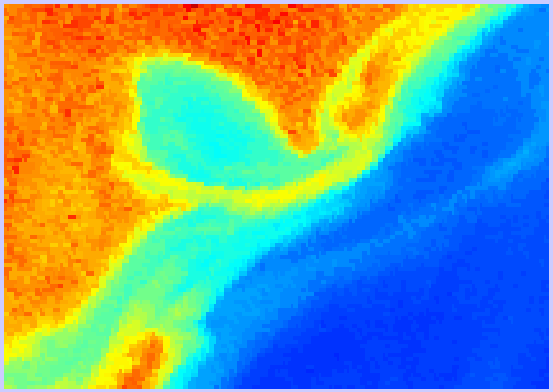

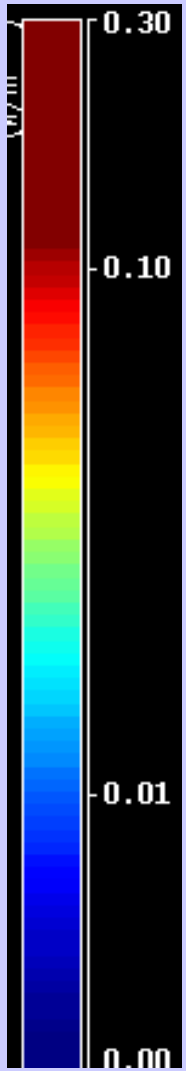

MODIS

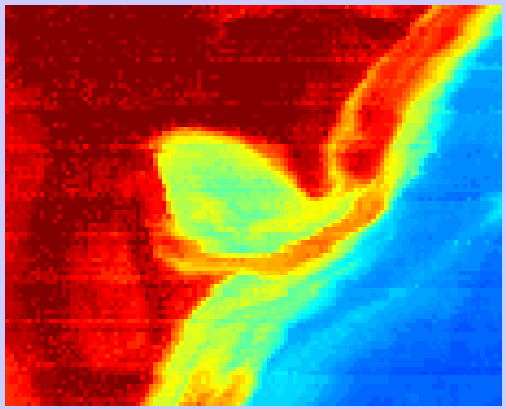

a_{cdm} (m^{-1})

SeaWiFS

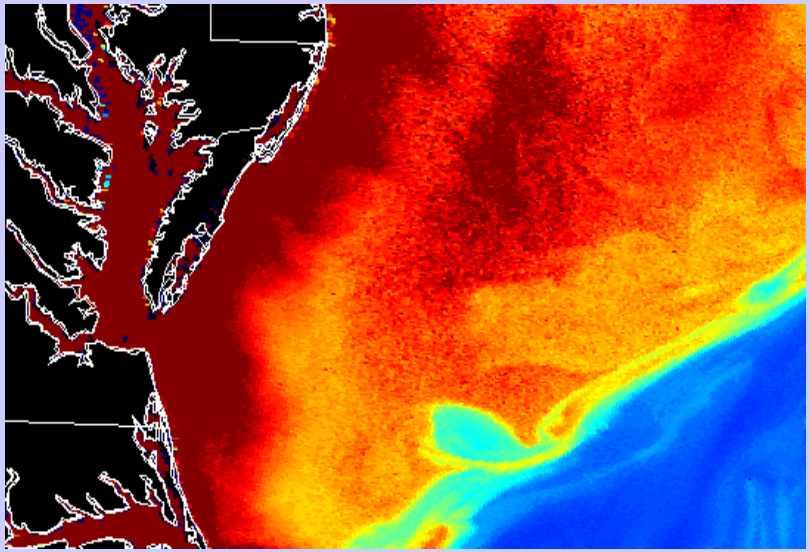

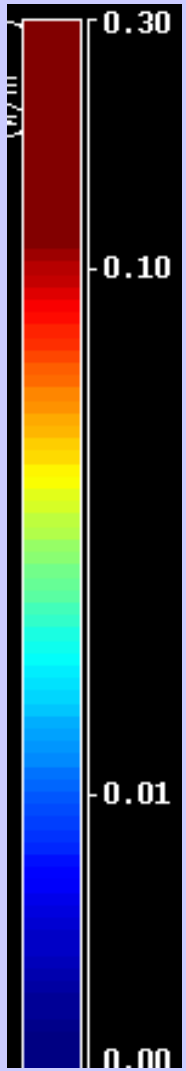

MODIS

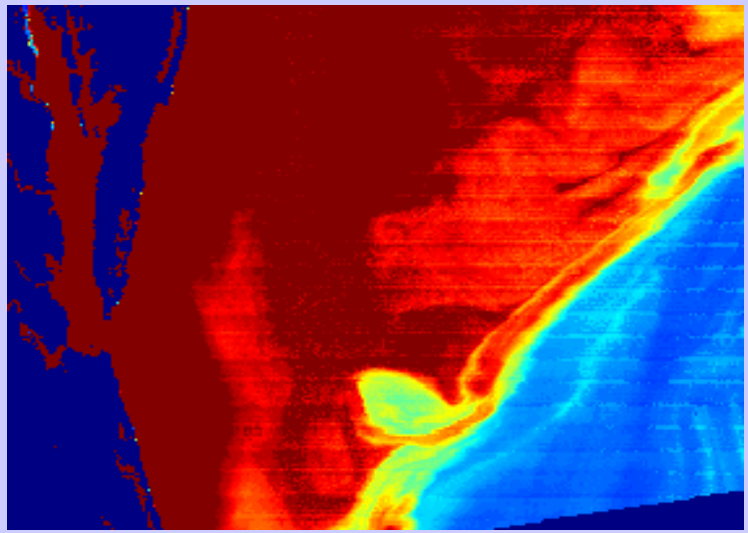

Chl (mg m^{-3})

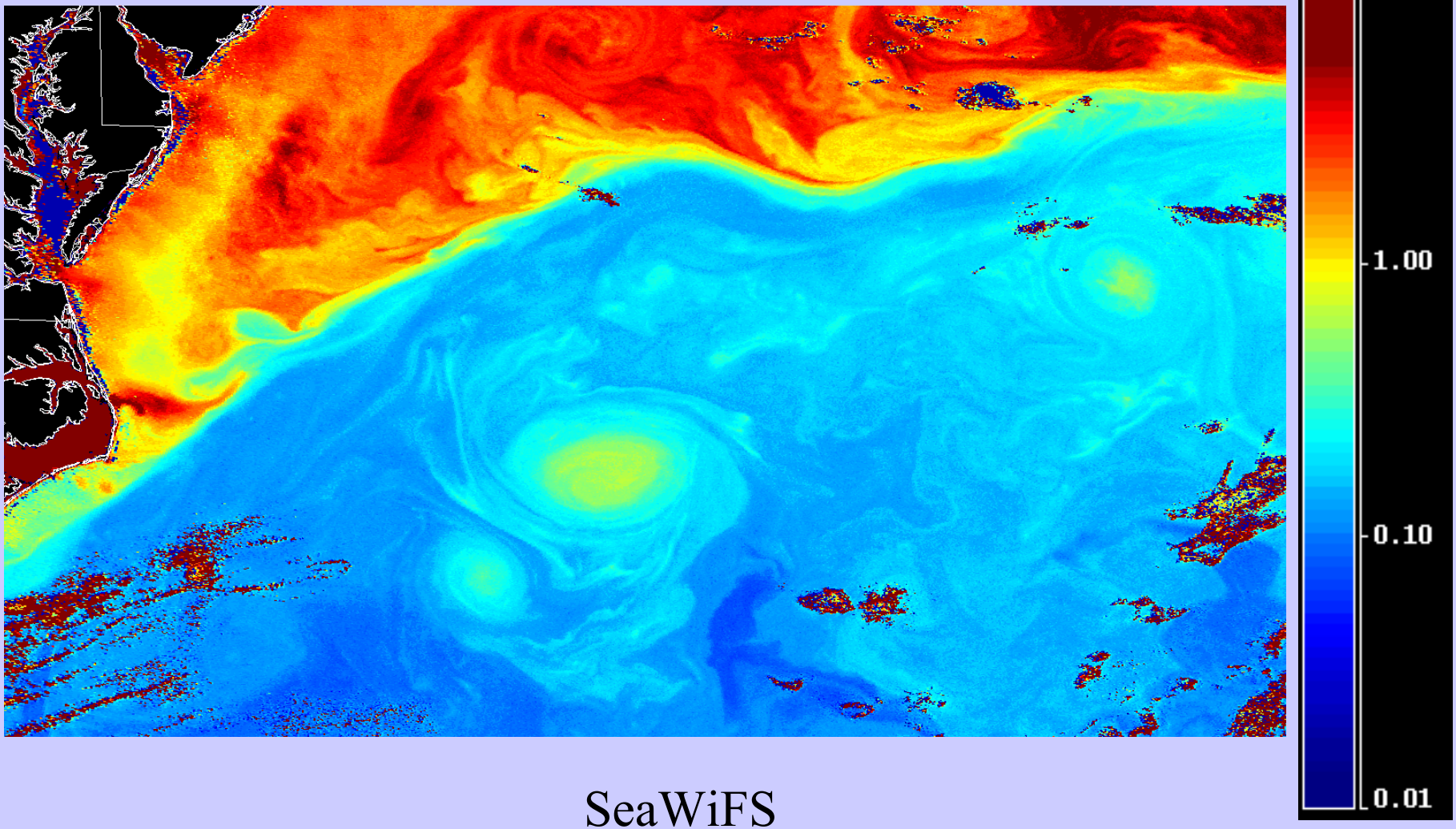

SeaWiFS

Chl (mg m^{-3})

SeaWiFS

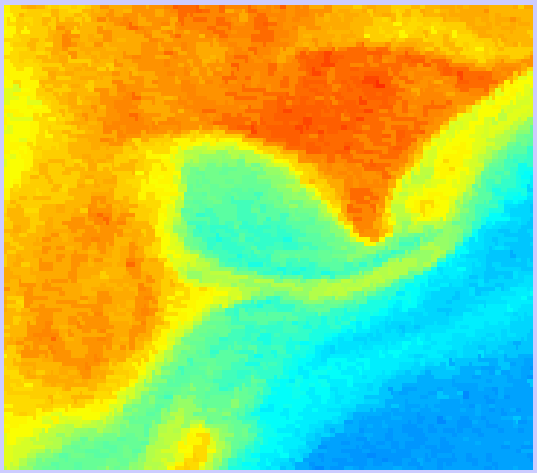

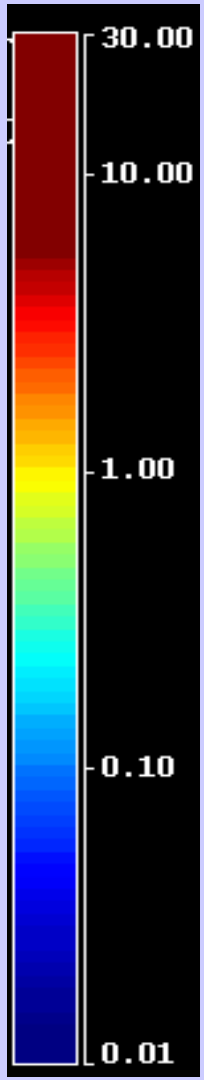

MODIS

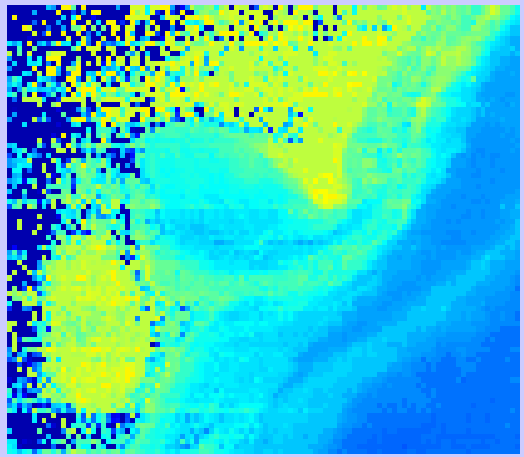

Chl (mg m^{-3})

SeaWiFS

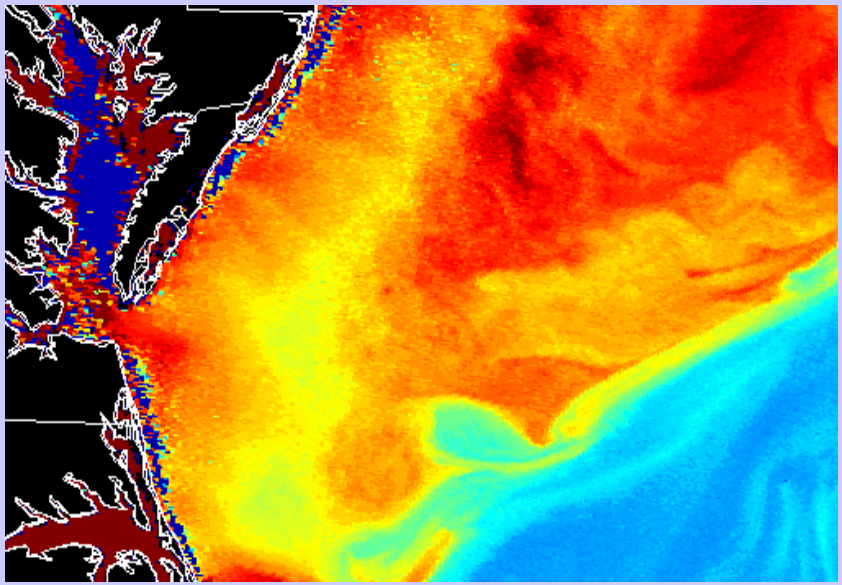

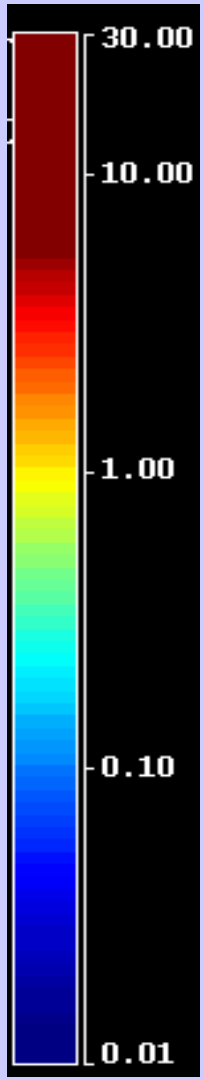

MODIS

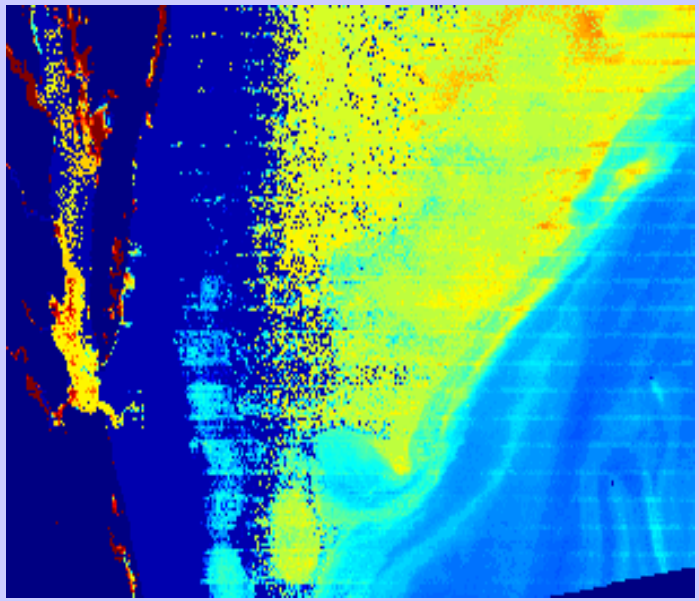

Summary

- Spectral Optimization Algorithm (SOA) works well with SeaWiFS (Case 1 waters).
- Potential for SOA in Case 2 waters is excellent — good continuity of atmospheric parameters (ω_0 and ν) across Case 1/Case2 boundaries.
- Code for MODIS imagery is now operating — retrieval of $b_{bp}(443)$ – good, $a_{cdm}(443)$ – fair, and C – poor.
- Retrieval problems are believed to be due to MODIS calibration.
- Will work with R. Evans to improve calibration, particularly the 869 nm band.
- Incorporation of the 500 m and 250 m bands is relatively straightforward.
- Preparing to make detailed comparisons of retrievals in Chesapeake Bay and Delaware Bay using AOL flights, surface measurements of C and a combination of MODIS and SeaWiFS imagery.

Appendix 2

LIDAR MEASUREMENTS OF MARINE AEROSOLS WITH IMPROVED ANALYSIS TECHNIQUES

By

David Earl Bates

A DISSERTATION

Submitted to the Faculty
of the University of Miami
in partial fulfillment of the requirements for
the degree of Doctor of Philosophy

University of Miami

Coral Gables, Florida

May 2003

UNIVERSITY OF MIAMI

A dissertation submitted in partial fulfillment of
the requirements for the degree of
Doctor of Philosophy

LIDAR MEASUREMENTS OF MARINE AEROSOLS WITH IMPROVED ANALYSIS TECHNIQUES

David Earl Bates

Approved:

_____	_____
Dr. Kenneth J. Voss Professor of Physics	Dr. Steven G. Ullmann Dean of the Graduate School
_____	_____
Dr. Howard R. Gordon Professor of Physics	Dr. G. Christopher Boynton Research Assistant Professor of Physics
_____	
Dr. Darek J. Bogucki Assistant Professor of Physics	

Bates, David E. (Ph.D. Physics)
(May 2003)

Lidar Measurements of Marine Aerosols with
Improved Analysis Techniques

Abstract of a doctoral dissertation at the University of Miami

Dissertation supervised by Professor Kenneth J. Voss

Number of pages in text: 95

Aerosols have been receiving increasing attention for two main reasons. First, their effects on the global radiation budget, both direct and indirect, are now understood to be substantial, and the difficulty in measuring their properties and distribution is the single largest source of uncertainty in calculations of global warming and climate change. Second, the interference of the atmosphere in satellite-based measurements of Earth surface properties is large and the variability is dominated by aerosols. In order to better understand the present and future states of the environment it is important to be able to measure the spatial and temporal distribution and optical properties of aerosols. My work has focused upon measuring the vertical distribution of aerosols over the oceans. In this dissertation I describe several new techniques for the analysis of lidar data and their application to data collected during ACE-Asia (Asian Pacific Regional Aerosol Characterization Experiment). The intensive field phase of this experiment was conducted in the spring of 2001 in and around the Sea of Japan. The field phase included a variety of instruments on land, sea and air measuring physical, optical and chemical properties of aerosols during a period of especially high dust levels in the atmosphere. The lidar system described in this dissertation was located aboard the NOAA Research Vessel Ronald H. Brown between March 14 and April 20, 2001. The lidar ACE-Asia data products include aerosol layer heights and thicknesses, aerosol optical depths, aerosol volume extinction and backscatter coefficients at 523 nm wavelength vs. altitude and corresponding extinction-to-backscatter ratios (“lidar ratios”). Improvements in the reliability (reduced uncertainty) of these data products is demonstrated based on

improved inversion techniques. These data are also correlated with other data products collected on the cruise.

For my parents.

Acknowledgments

I would like to thank Dr. Kenneth Voss for the many things he taught me and his generous support, guidance and assistance in my graduate work and doctoral research. I also thank Dr. Howard Gordon and Dr. Chris Boynton for their knowledge and help along the way. Thanks also to you, Albert Chapin, for your great help and comradeship over the last four years. I also express my friendship and appreciation to Zhang Hau, Du Hong, and Dr. Roman Chomko, my associates in the lab. And I must thank the University of Miami Physics Department for providing me with the opportunity and financial support to pursue my graduate education. In particular I want to thank Dr. George C. Alexandrakis for his kindness and for having faith in me.

I also want to thank my wife Karen and daughter Alora for their unflagging support of me through this long and sometimes trying process. I especially want to thank Karen for keeping the faith while I was gone to sea for seven weeks during ACE-Asia.

My participation in ACE-Asia was funded by NASA through the Goddard Space Flight Center, for which I am very grateful. I also gratefully acknowledge that my research assistantship was supported by NASA contract #NA55-31363.

Table of Contents

Ch. 1. Introduction

1.1 Purpose of this Research

It is increasingly apparent that to better understand global and regional climates and environments, it is necessary that scientists obtain more and better information about the properties and distribution of aerosols. This is because the lack of detailed knowledge about the optical properties of aerosols is one of the largest sources of uncertainty in climate forcing assessments [Dubovik et al., 2002]. Toward this end, more researchers are deploying instrumentation for the measurement of aerosols [Menzies et al., 2002]. In particular, there has been a lack of data about the vertical structure of marine aerosols [Voss et al., 2001]. Aircraft are expensive and difficult to operate, while balloon-borne instruments are currently limited to temperature, pressure, and RH measurements. Lidar plays a unique role in that it is one of the few ways to remotely obtain vertical information about aerosols. Many ground-based lidar systems are in use, for example those deployed by the United States Dept. of Energy Atmospheric Radiation Measurement (ARM) Program [ARM Aerosol Working Group Report, July 2000], NASA's MPLNET [Welton et al., 2001], and the European Commission's EARLINET [Schneider et al., 2000]. Although some of these lidars are on small islands, and therefore the atmosphere above them is mostly marine, the majority are located on large land masses and therefore measure mostly continental aerosols. It takes special effort to operate a lidar system at sea, because the equipment must be portable and rugged. Many lidar systems are large, heavy and delicate, and as a result are permanently mounted at ground locations. For example, the ARM project's CART Raman lidar is permanently

located at their Southern Great Plains site in Oklahoma [Turner, 2002]. The Micro Pulse Lidar (MPL) used in this research is one of the few lidar systems that is small and rugged enough to operate on a ship.

As the ocean surface is far more uniform than land, there are some aspects of marine aerosols that are simpler than continental aerosols. For instance, in the absence of continental-sourced layers, they tend to be composed mostly of hydrated sea salts and natural sulfates [Menzies et al., 2002]. And yet research has shown that at certain times and places, marine aerosols can be significantly contaminated or overlaid with aerosols of continental origin such as dust, soot, anthropogenic sulfates and organic compounds [Quinn et al., 2000]. These aerosols can persist for weeks and cover vast areas of ocean, significantly affecting the radiation balance [Ramanathan et al., 2001]. For example, aerosols containing soot from biomass burning in Africa and dust from the Sahara Desert can be found in the middle of the Atlantic Ocean [Voss et al., 2001]. To collect better data on marine aerosols, various large-scale research projects have been conducted, including ship-borne instrumentation extending far out to sea. This dissertation presents the lidar data collected during one such research cruise as part of ACE-Asia, as well as improved techniques for the analysis of such data.

1.1.2 Ocean Color and the Vertical Structure of Marine Aerosols

Currently there are two U.S. satellite-based imaging instruments (SeaWiFS and MODIS) deployed in part for the purpose of measuring the color of light leaving the ocean surface to determine chlorophyll concentration [Gordon, 1997]. The light received by these instruments is predominately (approximately 90%) reflected by the atmosphere, and the atmospheric part must be removed to ascertain the true ocean color

[Chomko and Gordon, 1998]. If the aerosols are nonabsorbing, this process of atmospheric correction may be done without knowledge of the aerosol vertical structure [Gordon, 1997]. However, if the aerosols *are* absorbing, atmospheric correction is heavily dependent upon aerosol vertical structure [Gordon et al., 1997]. Lidar is one of the few tools by which this structure may be measured, and support of atmospheric correction of ocean color is another purpose of this research.

1.2 ACE-Asia

The lidar and sunphotometer data presented in this dissertation were collected as part of ACE-Asia between March 14 and April 20, 2001 aboard the NOAA R/V Ronald H. Brown (the "Ron Brown"). A Micro Pulse Lidar system (described below) and a MicroTops™ handheld sunphotometer (Solar Light Co. Philadelphia, PA) were used. This dissertation uses the ACE-Asia lidar data to demonstrate analysis techniques, and presents the results of that analysis to provide specific information on the vertical structure and optical properties of the observed aerosols. The focus of the ACE-Asia experiment is the large amount of Asian dust and pollution carried into the troposphere each spring [Huebert, 2001]. It is expected that these aerosols may have enough absorption to change the sign of the aerosol forcing (that is, whether the aerosol has a net heating or cooling effect) from that calculated without strong absorption [Dubovik et al., 2002].

Ch. 2. Lidar Description and Calibration

2.1 Description of Elastic Lidar used in this Research

The basic concepts of aerosol science, sunphotometry, and lidar analysis are discussed in Welton [1998]. The reader unfamiliar with these subjects is referred to this and other sources. Those aspects that are particularly relevant to the research presented in this dissertation are discussed below.

2.1.1 Hardware

The lidar system used in this research is a standard system manufactured by Science and Engineering Services, Inc. (SESI), Burtonsville, MD USA. It is known as a "Micro Pulse Lidar" (MPL), invented by Dr. James Spinhirne of NASA [Spinhirne, 1993]. The system is of coaxial design, with a pulsed 523 nm green laser beam of limited power (10-20 μJ/pulse) expanded to 20 cm diameter, and is eye-safe. In this work the MPL system was operated with a pulse rate of 2500 Hz and a time resolution of 500 ns, corresponding to 75 m range resolution. The signal is sufficient to detect aerosols and measure atmospheric properties up to approximately 10 km during daylight conditions and up to approximately 30 km at night [Spinhirne, 1995]. Data were collected for ranges extending to 60 km; the data beyond 30 km is used for background noise correction as discussed in Chapter 2. These settings are the standard settings used by MPLNET, a network of MPLs being operated by NASA.

The lidar transceiver is based upon a 20 cm Schmidt-Cassegrain telescope through which the lidar source (consisting of 10 ns laser pulses) is expanded and projected, and through which light reflected backward by the atmosphere is collected.

The expanded beam has a divergence of approximately 500 μradians, while the field of view of telescope is about 1000 μradians, so that the entire direct beam remains in the field of view. This is important for the quantitative analysis of signals. The small field of view is important for reducing skylight contamination and multiply-scattered lidar photons.

The laser head and photon-counting detector (Avalanche Photo Diode or APD) are enclosed in an aluminum housing attached to the back of the telescope tube. The detector responds to individual photons, emitting a 10 ns TTL pulse for each photon detected. The detector is preceded by a narrow-band (0.1 nm) green filter centered at 523 nm. This filter passes light reflected by air molecules and light reflected by aerosol particles. Such a system is referred to as an elastic lidar. The transceiver may be pointed at any angle, but is normally directed vertically. The transceiver is connected to a laser power supply unit manufactured by Spectra-Physics, Inc., and a specialized scaler unit for counting received photon pulses. The laser power supply produces continuous infrared laser light which is sent to the laser head in the transceiver via fiber-optic cable. The laser head is "pumped' by the continuous infrared light, and in turn emits visible green light. The laser power supply also serves as the laser control unit, allowing adjustment of laser power, pulse repetition frequency, etc., and providing the RF Q-switch signal which actually pulses the laser head. The Q-switch signal prevents the laser head from putting out light except when it is off. By turning the Q-switch signal off briefly, the power supply causes the laser head to emit very short pulses of green light. The scaler receives the TTL pulses from the detector and counts them in 500 ns bins. It is in turn connected to an IBM PC-compatible personal computer for system control and

data storage. The laser pulse energy has a short-term rms energy variability of 5% and drifts slowly with time by as much as 50% over a period of months. Consequently the output energy of the laser is monitored inside the MPL transceiver and saved in the data records. Further details of the system may be found in [Spinhirne, 1993] and [Spinhirne, 1995].

2.1.2 The Lidar Equation

The signal received by an ideal elastic lidar is described by the lidar equation:

$$\frac{dN}{dt}(r) = N_0 \frac{c}{2} \frac{A}{r^2} \beta(r) \exp\left(-2\int_0^r \alpha(r')\,dr'\right) \qquad (2.1.1)$$

Here, $dN/dt(r)$ is the number of photons received in the lidar detector in a time dt after reflecting (backscattering) off of the atmosphere a distance r away. The MPL system stores data in photoelectrons (counts) per microsecond, so we have used photons per time here, assuming one count per photon in the detector. $\beta(r)$ is the volume backscatter coefficient and $\alpha(r)$ is the volume extinction coefficient. β is a measure of how strongly a parcel of atmosphere backscatters light, while α is the fraction of a light beam lost to scattering and absorption as it passes through a thin parcel of atmosphere. The exponential term in (2.1.1) is the transmission of the atmosphere for a round trip over the distance r. The "2" is due to the fact that the light pulse must travel through the intervening atmosphere twice as it goes from the lidar to range r and back. N_0 is the number of photons in the outgoing pulse, c is the speed of light in air, A is the area of the receiver objective, and A/r^2 is the solid angle subtended by the receiver as seen from the distance r. The outgoing pulse is a laser beam and does not spread significantly over the distances involved ($\leq$ 30 km).

The actual data represent the integral of the lidar equation over consecutive 500□ns time periods (bins), and are indexed by the integer *n*. Assuming slowly-changing values of *dN/dt(r)*, □*(r)*, and □*(r)*, we assume the counts per microsecond for the *n*th bin (or *N*(*n*)) is equal to the value of *dN/dt(r)* at the bin center times the 500 ns period Δ*t*:

$$N(n) \equiv \int_{t_n}^{t_{n+1}} \frac{dN}{dt}\, dt \approx \frac{dN}{dt}(r_n)\,\Delta t \tag{2.1.2}$$

where r_n is the distance from the lidar to the center of the *n*th bin:

$$r_n = r_0 + \frac{c}{2}\,\frac{(t_n + t_{n+1})}{2}. \tag{2.1.3}$$

r_0 is the range offset – see sections 2.2.4 and 4.3. Written in discrete form the ideal lidar equation is

$$N(n) = N_0\,\frac{c}{2}\,\frac{A}{r_n^{\,2}}\,\beta(r_n)\exp\left[-2\sum_{m=1}^{n}\frac{(\alpha(r_m)+\alpha(r_{m-1}))}{2}(r_m - r_{m-1})\right]\Delta t \tag{2.1.4}$$

where we have used (2.1.2) and the trapezoidal approximation for the □-integral. Setting $\beta(n) \equiv \beta(r_n)$, $\alpha(n) \equiv \alpha(r_n)$, and

$$\tau(n) \equiv \sum_{m=1}^{n}\frac{(\alpha(r_{m-1})+\alpha(r_m))}{2}(r_m - r_{m-1}) \tag{2.1.5}$$

we may write

$$N(n) = N_0\,\frac{c}{2}\,\frac{A}{r_n^{\,2}}\,\beta(n)\exp(-2\tau(n))\,\Delta t. \tag{2.1.6}$$

We now introduce a dimensionless constant C_0 to represent any losses in the system:

$$N(n) = N_0 C_0\,\frac{c}{2}\,\frac{A}{r_n^{\,2}}\,\beta(n)\exp(-2\tau(n))\,\Delta t. \tag{2.1.7}$$

To be consistent with other researchers we write the energy of the outgoing pulse as $E(\mu J) = N_0 / 2.63 \times 10^{12}$ (λ = 523 nm) and combine C_0, c, A, and Δt into a new constant C, and obtain

$$N(n) = CE\frac{1}{r_n^{\,2}}\beta(n)\exp(-2\tau(n)). \tag{2.1.8}$$

Dividing by E and multiplying by r^2 we obtain the *normalized relative backscatter* (*NRB*) data for an ideal lidar with system constant C:

$$NRB(n) \equiv \frac{r_n^{\,2}}{E}N(n) = C\beta(n)\exp(-2\tau(n)). \tag{2.1.9}$$

We can express C in terms of the other constants, with 2.63×10^{12} photons/μJ (λ = 523 nm), $A = \pi$ (0.0001 km)^2 = 3.14159×10^{-8} km^2, $c = 3.00\times10^{8}$ m/s, and $\Delta t = 500\times10^{-9}$ s:

$$C \equiv \frac{c\,A\,\Delta t}{2}\times 2.63\times10^{12} C_0 = 6.20\times10^{6}\ C_0 . \tag{2.1.10}$$

The units of C as defined here and in the rest of this dissertation are m-km^2/sr.

2.2 Lidar Calibration

In practice, however, there are certain nonideal behaviors of a lidar system, and among these are detector deadtime, the system constant C (defined above), background noise *BG*, the afterpulse function *AP(r)*, and the overlap function *O(r)*. When these are included the lidar equation is:

$$\frac{dN}{dt}_{DTC}(r) = BG + N_0 \left[\frac{C}{t} O(r) \frac{1}{r^2} \beta(r) \exp(-2\int_0^r \alpha(r')dr') + AP(r) \right] \quad (2.1.11)$$

or in discrete form:

$$N_{DTC}(n) = BG + E \left[C O(n) \frac{1}{r_n^2} \beta(n) \exp(-2\alpha(n)) + AP(n) \right] \quad (2.1.12)$$

The subscript DTC indicates that the data has been deadtime corrected as described below.

2.2.1 Detector Deadtime Correction

It is necessary to compensate for deadtime in the MPL's avalanche photodiode detector (APD). This is the behavior that after detecting a photon, there is a very small amount of time (~50 ns) during which the detector is unable to detect any more photons. This is due to the need to discharge the junction of the avalanche charge. Although there is an active quenching circuit to speed this up, the small deadtime remains. The detector manufacturer (PerkinElmer Optoelectronics, Vaudreuil, Quebec, Canada) supplies data by which a statistical correction can be made relating the number of counts in a certain amount of time (in this case 500□s) to the probable number of photons that actually entered the detector. This correction is applied to all data before any further processing.

2.2.2 Background Noise Correction

When a lidar system is operated during daylight hours, ambient green skylight enters the transceiver and produces significant levels of random photon counts in the detector. In this work data is taken for 400 us after an outgoing pulse, corresponding to a distance of 60 km. The data from beyond 30 km is found to be constant on average, and

is assumed to represent the background noise only. This background noise is deadtime corrected and averaged, and then the average value is subtracted from the deadtime corrected data.

2.2.3 Afterpulse Function

If the MPL is operated in a vacuum, one would expect no return signal whatsoever. However, in practice it is found that under conditions approximating such a vacuum (such as with the MPL directed at a black surface at close range in the dark), there is still some small received signal. This signal is proportional to the outgoing pulse energy, with an amplitude vs. time that is generally a small spike with a tail that falls off fairly quickly. This unwanted return signal represents "leakage" of the outgoing light pulse into the nearby detector hardware, and possible "afterpulsing" of the detector (false detection of nonexistent photons by the detector after a burst of detected real photons). The afterpulse signal is a function of time (or distance, related by the speed of light) and, as mentioned, is proportional to outgoing pulse energy. In practice the afterpulse function is determined by measuring the return signal with the MPL directed at a black target at near range many times, dividing each return signal by its pulse energy, and averaging. Field data records are corrected for deadtime and background noise, then divided by pulse energy, after which the afterpulse function is subtracted. The afterpulse function is generally very stable, and is a small fraction of normal atmospheric signals. One positive side effect of pulse leakage is that it allows identification of the outgoing pulse in the data records, when independent synchronization is unavailable, although to limited accuracy (see the sections on range offset).

2.2.4 Range-Offset

Another calibration issue is range-offset. The MPL system starts counting received photons as soon as the laser power supply sends the scaler a TTL pulse indicating that the laser head has been pulsed. In practice, there is a delay between the arrival of the TTL pulse in the scaler and the emission of the actual light pulse. This can be seen by examining the first few data bins from a recorded afterpulse signal, and observing that there are virtually no received photons detected in the first 500 ns bin, and then a small but distinct number in the second 500 ns bin, followed by small numbers in subsequent bins. The conclusion is that the second bin contains a pulse of photons that have leaked from the outgoing pulse into the detector, and thereby serve to identify the actual emission of the light pulse. Normally the third bin is taken as the first actual data bin, and is considered to represent reflections from the first 75 m of atmosphere. Range-offset is an issue related to the assignment of distance to each data bin, and therefore does not appear in equation (2.1.2), which is expressed in terms of the continuous variable *r*. See Chapter 3 for more discussion of range-offset.

2.2.5 Range Correction

Although the laser beam travels upward with very little divergence (~50□radians), the reflected light diverges according to the inverse-square of range, and hence the data from increasing ranges are proportionately less simply by virtue of the smaller solid angles subtended by the receiver objective. The data from a bin centered at range *r* must be multiplied by r^2 to correct for this inverse-square loss. It is important

that the values of bin-center ranges used in range-correction of actual data are the same as those used in determining the overlap function (see below).

2.2.6 Overlap Function

The overlap function is a measure of a different nonideal behavior of most lidar systems. The receiving part of the transceiver, being a telescope focused at infinity with a very small field of view, is unable to focus reflected light from near ranges (in the MPL system described this is $r <$ 5 km). The result is that not all of the photons that enter the telescope objective from near ranges end up in the detector. Since under theoretical conditions typical return signals are much stronger at near ranges, this behavior produces an effect called "optical compression" which is actually desirable if the detector has limited dynamic range. However, this behavior must be compensated for to allow proper interpretation of the data. The overlap function is realized as a correction factor < 1 for each data bin corresponding to a range < ~5 km, and equal to one for $r >$ ~5 km. It is measured by directing the MPL transceiver horizontally in a horizontally homogeneous atmosphere (when such an atmosphere can be found). In such a situation the theoretical return signal is given by the ideal lidar equation (range-corrected, energy-normalized) with β and σ constant over distance:

$$NRB(n) = \frac{r_n^{\,2}}{E} N(n) = C \cdot \exp(-2 \cdot \sigma \cdot r_n) \qquad (2.1.13)$$

This is an exponential decay over distance. The constant σ can be deduced from actual horizontal data (corrected for deadtime, background, afterpulse, and range, and divided by N_0) by using only the data from the far ranges ($r >$ 5 km). The near range correction

factors *O(n)* can then be found by extrapolation to near ranges. The corrections to the data are realized by solving Equation (2.1.12):

$$\left[\frac{N_{DTC}(n) - BG}{E}\right] - AP(n)\left[\frac{r_n^2}{O(n)}\right] = C\,\beta(n)\exp(-2\tau(n)) = NRB(n)\ . \qquad (2.1.14)$$

It is important in overlap function determination to use the same bin-center ranges as will be used in the actual data analysis. The exact range numbers are not critical, as the procedure also corrects for any errors in the range-correction for near ranges, as long as the same range-correction is used for field data. At far ranges it is assumed that the range-correction is accurate enough, as the range numbers are so much larger than the possible error.

2.2.7 System Constant *C*

The system constant *C* is an overall scale factor that represents the loss of the system with respect to outgoing light energy. *C* is dependent upon the detector counting efficiency, dirt or moisture on the objective glass of the transceiver or any windows, losses in optical components such as filters and beam splitters, and similar factors. Knowledge of *C* is important for interpreting the data quantitatively, but *C* generally cannot be determined until the actual vertical data are analyzed. It is not separable from the backscatter coefficient in horizontal overlap data, and calibrations against artificial standard targets are found to be difficult if not impossible. *C* may be determined by analyzing data collected on cloud- and stratospheric aerosol-free days with an independent measurement of the aerosol optical depth at the same time, place and wavelength. Since the volume backscatter and extinction coefficients of air in the

atmosphere are known to a high degree of accuracy, the data reflected by the air above any aerosol can be used together with the measurement of aerosol optical depth to find *C*. This is described in detail in section 3.2.2.

Ch. 3. Lidar Signal Analysis Techniques

3.1 Standard Analysis Techniques

3.1.1 Normalized Relative Backscatter (*NRB*)

Lidar data are typically collected and stored for later analysis. The data are first corrected for instrument errors and inverse-square range falloff to produce the normalized relative backscatter (*NRB*). *NRB* data still contain the multiplicative system constant *C*, which is often not known until the data are analyzed. The *NRB* data are related to the volume extinction and backscatter coefficients by:

$$NRB(r) = C\beta(r)\exp(-2\int_0^r \alpha(r')dr') \qquad (3.1.1)$$

where *C* is the system constant, $\beta(r)$ is the volume backscatter coefficient in inverse meters times inverse steradians, and $\alpha(r)$ is the volume extinction coefficient in inverse meters.

3.1.2 Attenuated Backscatter (*ABS*)

When *NRB* data are divided by *C* one obtains the attenuated backscatter (*ABS*) data (*ABS* = *NRB* / *C*). The *ABS* data are a record of the intensity of light reflected directly backward (usually downward) from each distance, given the attenuation (extinction) the light has undergone in transiting the intervening atmosphere. In theory, *ABS* data contain information about the atmosphere alone – all instrument factors have been removed, i.e.:

$$ABS(r) = \beta(r)\exp(-2\int_0^r \alpha(r')dr') . \qquad (3.1.2)$$

But until we know *C* we must work with the *NRB* data.

3.1.3 Aerosol and Rayleigh Components

It is customary in aerosol research to immediately distinguish between the extinction due to air itself, which is the molecular, or Rayleigh, extinction α_R (after Lord Rayleigh who pioneered much of our understanding of the propagation of light through the atmosphere) and the extinction due to aerosols (α_A). Under normal lidar conditions, for which multiple-scattering effects are negligible [Ackermann et al., 1999], the two extinctions simply add:

$$\alpha = \alpha_R + \alpha_A \,, \tag{3.1.3}$$

as do the corresponding backscatter coefficients β_R and β_A:

$$\beta = \beta_R + \beta_A \,. \tag{3.1.4}$$

The ratio of extinction coefficient to backscatter coefficient, *S*, is an important quantity in lidar research:

$$S \equiv \alpha / \beta. \tag{3.1.5}$$

The units of *S* are steradians (sr). Again, aerosol and Rayleigh quantities are distinguished by subscripts:

$$S_R \equiv \alpha_R / \beta_R \,, \qquad S_A \equiv \alpha_A / \beta_A \,, \tag{3.1.6), (3.1.7}$$

and

$$S = \frac{\alpha_R + \alpha_A}{\beta_R + \beta_A} \neq S_R + S_A \,. \tag{3.1.8}$$

Written in separate terms the *NRB* lidar equation takes the form:

$$NRB(r) = C(\beta_R(r) + \beta_A(r))\exp(-2\int_0^r (\alpha_R(r') + \alpha_A(r'))dr'), \quad (3.1.9)$$

also known as the 2-component *NRB* lidar equation. $\beta_R(r)$ and $\alpha_R(r)$ are known to a high degree of accuracy for the Earth's atmosphere, and their ratio S_R is known to be $8\pi/3$, also to a high degree of accuracy. For the work presented in this dissertation, Rayleigh extinction profiles were calculated using a theoretical expression for extinction coefficient [Zuev, 1976], with number density from standard atmospheric profiles [United States Standard Atmosphere 1976, 2002] corrected to measured surface temperature and pressure, and the index of refraction for air [Filippenko, 1982]. Rayleigh backscatter profiles are just the extinction profiles divided by S_R.

Thus, the only quantities (other than *C*) in the lidar equation which are unknown are $\beta_A(r)$ and $\alpha_A(r)$, and these are what we are trying to find. For a given *NRB*(*r*) measurement, there are infinitely many pairs of $\beta_A(r)$ and $\alpha_A(r)$ profiles which will satisfy the lidar equation. Fortunately, the aerosol lidar ratio S_A for typical aerosols is known generally to lie within certain bounds (~20-80 sr), and can be approximated for different types of aerosols. Given an assumed lidar ratio profile $S_A(r)$, one may find a unique solution to the lidar equation for a given *NRB*(*r*), and thus a useful estimate of $\beta_A(r)$.

3.1.4 Fernald Inversion Algorithm

The basic numerical inversion algorithm used in this research is known as the "inward Fernald two-component solution" [*Fernald,* 1984]. Since the range of measured *NRB* data is quantized in equally-spaced bin-center ranges (75m per bin in this research), we will express the quantities in the lidar equation as functions of integer *n*, where the

center of the *n*th bin is at a distance of 75□n times (*n*-1/2) plus the range-offset. The solution (for constant S_A) then appears as [*Fernald*, 1984] (3.1.10)

$$\beta_A(n-1) = \frac{NRB(n-1)\exp((S_A - S_R)(\beta_R(n)+\beta_R(n-1))\Delta r)}{\frac{NRB(n)}{\beta_A(n)+\beta_R(n)} + S_A(NRB(n)+NRB(n-1)\exp((S_A - S_R)(\beta_R(n)+\beta_R(n-1))\Delta r))\Delta r} - \beta_R(n-1).$$

This may not look very nice – it is complicated by the separation of $\beta(n)$ and $\alpha(n)$ into aerosol and molecular (Rayleigh) parts. But this separation makes the algorithm more directly applicable to the atmospheric problems for which it was designed. For example, S_R is a constant but S_A depends upon the aerosol, and combining them obscures the aerosol properties. Holding *S* constant with altitude would actually imply that S_A is not constant with altitude, but trades off with the varying ratio of aerosol to Rayleigh extinction. In variable-S_A inversions (see section 3.2.6) combining the components would be even more confusing. Also note that since each term in the numerator and denominator of the right-hand side of this equation has an *NRB* factor, the system constant *C* divides out completely, and *NRB* may be replaced by *ABS*. In fact, the Fernald algorithm is based upon the ratio of an *NRB* data point to the one below it, and as both contain the factor *C*, it disappears. The Fernald algorithm and the solutions it gives are independent of *C*.

In the rest of this discussion it is assumed that the lidar system is directed vertically – this was the case in this research except when overlap-correction data were taken. The Fernald inward solution assumes a value for β_A at a range index n_c (the "calibration" altitude) for which it is thought to be known, such as above all aerosol layers (where it is 0), and, assuming a value for S_A, calculates β_A and α_A at an altitude one bin-width lower (n_c-1). The process is repeated until the lowest-altitude bin is reached. The process has been shown to be numerically stable under all conditions [*Fernald*,

1984], unlike the corresponding "Fernald outward" version. The Fernald solution uses linear interpolation to approximate the integral, which is certainly adequate to the task given the resolution of the system. The accuracy of the Fernald solution depends upon the approximation $e^x \approx 1+x$, and here x is β_A times 75 m, which for an extremely high value of $\beta_A = 0.6\ \mathrm{km}^{-1}$ is 0.045, and the approximation is good to 0.1%. Alternatively, one may use the *NRB* lidar equation, $\beta_A(n)$ and S_A (replacing β_A with $S_A\beta_A(n)$) and iterate on it (via Newtonian search, for example) to find a value for $\beta_A(n\text{-}1)$ which gives the *NRB*(n) and *NRB*(n-1) data to whatever accuracy is desired, but this takes more computational time.

The first approximation to a solution for $\beta_A(n)$ is to assume a reasonable value for the aerosol lidar ratio S_A, and assume it to be *constant with altitude*, and then, starting at a point believed to be above all aerosol layers, use the inward Fernald two-component algorithm to work down to the altitude of the lowest-range bin.

3.1.5 Inverting to a Known AOD

The AOD (aerosol optical depth) or τ_A is the integral over distance of the aerosol volume extinction coefficient:

$$\tau_A = \int_0^\infty \beta_A(r')\,dr' \tag{3.1.11}$$

while for a distance r above the surface the AOD of the atmosphere below is

$$\tau_A(r) = \int_0^r \beta_A(r')\,dr' \,. \tag{3.1.12}$$

τ_A may be measured directly using a sunphotometer, or inferred from the 2-component lidar equation if one knows the system constant C. This is described in section 3.2.2. Given a value of τ_A, one would like to constrain a Fernald inversion to produce an aerosol extinction profile that integrates to that value. This is done by first making a guess at S_A and applying the Fernald algorithm. Once a profile of $\alpha_A(n)$ is found using the assumed value of S_A, the corresponding AOD may be calculated by numerically integrating the $\alpha_A(n)$ profile from the lidar altitude (assumed to be at the surface) to the top altitude point n_c (at and above which there is assumed to be no aerosol). The resulting calculated AOD may then be compared to the known value of the AOD, and the ratio of the two AODs may be used to modify the assumed value of S_A [*Welton*, 1998] according to the formula

$$S_A(new) = S_A(old)\frac{AOD(measured)}{AOD(calculated)}. \qquad (3.1.13)$$

This process may be repeated until the calculated AOD matches the known AOD to sufficient accuracy. This procedure is also generally quite stable and will produce a final value of S_A that approximately represents a "column average" of the actual aerosol lidar ratio [*Welton*, 1998]. The retrieved extinction profile $\alpha_A(n)$ can be used to identify separate layers when present, but in general may have significant errors in the recovered extinction due to the assumption of a constant S_A.

The above discussion describes the standard basic techniques used for lidar data analysis. Improved techniques for dealing with noise and methods for better determining S_A as a variable function of altitude are discussed below and in Chapter 5.

3.2 Improved Analysis Techniques

In this section I will present some new techniques to deal with ambient noise in lidar signals and the imperfections of the hardware. Even for a constant-S_A inversion, there are difficulties due to noise in the signals. I have developed several techniques to better deal with this problem, which are described below.

3.2.1 Smoothing Filter

Often, the noise in *NRB* signals is so large as to cause standard inversion algorithms to fail or give anomalous results. I have applied to such signals an "expanding" Gaussian filter, which smoothes the data to an extent that is proportional to the noise, which generally follows the squared range. The filtered data at a given range is a Gaussian-weighted sum of the unfiltered point and the nearest-neighbor points, such that the width of the Gaussian is proportional to the noise at that range. The filtered data are normalized to the filter width at each range, such that a constant signal would be left unchanged. The noise in the signal is determined as follows. The corrected data records, normally collected over one minute time periods, are themselves averages of thousands of "shots". In this work each record is an average of 2500 shots per second times 60 seconds = 150,000 shots. However, in daylight conditions there is still substantial noise at far ranges, and this is reduced by averaging multiple one-minute records over ten to sixty minutes. At the same time, the standard deviation at each range is computed. An r-squared function is then fit to the standard deviation data to find the "noise factor" – this is a measure of the ambient noise plus variations in the data due to changes in the

atmosphere during the period in question. This noise factor is then used to determine the Gaussian filter width at each point. The actual equation for the filter is

$$SmoothedData(n) = \frac{\sum_{m=0}^{m\max} Data(m)\, e^{-[(range(m)-range(n))/(NF\cdot range^2(n))]^2}}{\sum_{m=0}^{m\max} e^{-[(range(m)-range(n))/(NF\cdot range^2(n))]^2}}. \tag{3.2.1}$$

The result is that for signals with low noise, the filter does almost nothing, while for noisy signals it smoothes the far ranges while leaving the near ranges alone. Figure 3.2.1 shows an example of unsmoothed and smoothed *NRB* data.

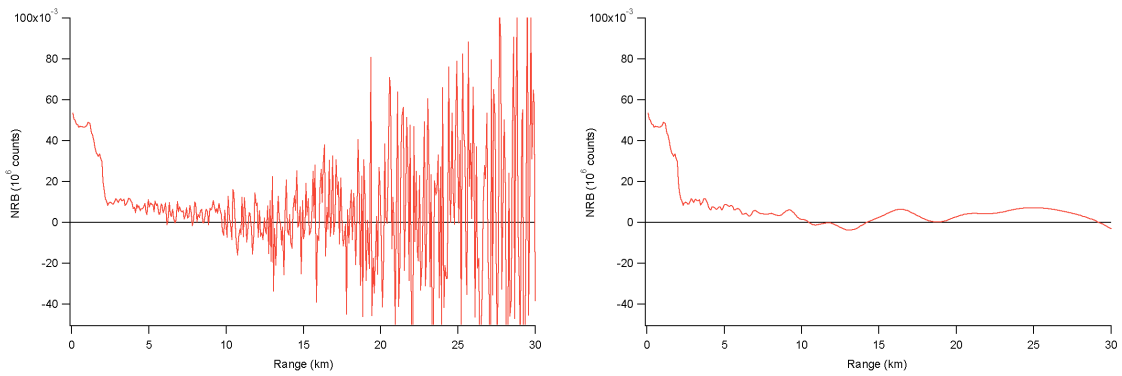

Figure 3.2.1. Typical unsmoothed and smoothed *NRB* data.

The standard deviation of the smoothed data is computed as the unsmoothed standard deviation divided by the square root of the filter width at each range.

3.2.2 Determination of *C*

The system constant *C* is an important parameter in recovering extinction and backscatter from lidar data. However, calculation or direct hard-target measurement of *C* is notoriously difficult [Fernald et al., 1972]. In practice the best measure of *C* comes

from the lidar data itself combined with an independent measurement of τ_A. The approach used in this research is to identify an altitude above which there is no aerosol, and to deduce *C* from the data there and the AOD at 523 nm (τ_A) wavelength using the *NRB* lidar equation at altitudes above all aerosol:

$$NRB(r) = C\beta_R(r)\exp\left(-2\int_0^r \alpha_R(r')dr'\right)\exp(-2\tau_A) \qquad (3.2.2)$$

which allows calculation of *C* for each value of r at which *NRB* data is available. Let us define "attenuated Rayleigh *ABS* profile" to be the right-hand side of equation (3.2.2), with $C = 1$. This is the lidar *ABS* signal expected from an aerosol-free atmosphere, but attenuated by the independently measured aerosol extinction, that is, multiplied by $\exp(-2\tau_A)$. The Rayleigh *ABS* profile may be computed from the sea-level pressure and known Rayleigh atmospheric properties. In this analysis of lidar data the best value of *C* is found by doing a weighted least-squares fit of an attenuated Rayleigh *ABS* signal multiplied by *C* (the expected *NRB* signal above all aerosol) to the *NRB* data, with *C* being the fit parameter. The range of values of r over which the fit is done is from the assumed top-of-aerosol to 18 km, unless there are thin clouds above the aerosol in which case the upper limit is set (by inspection) to just below the clouds. The weighting is one over the standard deviation computed during averaging. If *C* is known and τ_A is not, one may reverse the roles of *C* and $\exp(-2\tau_A)$ to find τ_A. Thus a calibrated lidar may also serve as a sunphotometer. What is often unclear is: what altitude is the top-of-aerosol? A technique to determine this is described in the following sections.

3.2.3 *C*-Matching

When *NRB* data are inverted as described with a constant aerosol lidar ratio S_A, constrained to a known value of τ_A (whether independently measured or by inference from a known value of *C* and the Rayleigh portion of the data), one obtains a column value of S_A and an extinction profile that integrates to the known AOD. One may reconstruct the *ABS* signal using the lidar equation, and it should be the *NRB* signal divided by *C*. Thus, if one inverts the *NRB* data with a known AOD, one may then find *C* by dividing the *NRB* data by the reconstructed *ABS* data. This is done here by finding the best value of *C* which fits the reconstructed *ABS* data to the measured *NRB* data, using a weighted least-square error criterion. In practice the inverted data fit so well that the method of finding *C* doesn't matter very much. What does matter is that the value of *C* retrieved this way must be the same as the value implied by the AOD and the above-aerosol lidar data. When they don't agree, it must be either because one has not truly found the top-of-aerosol or because of errors in the AOD or inversion algorithm. Assuming the AOD is correct, and the Rayleigh calculations are all correct, one must examine the inversion algorithm with respect to noise. Looking at the lidar equation again, with aerosol and Rayleigh components combined, we have

$$NRB(r) = C\beta(r)\exp(-2\int_0^r \alpha(r')\,dr'). \tag{3.2.3}$$

At an altitude Δr below *r* we have

$$NRB(r-\Delta r) = C\beta(r-\Delta r)\exp(-2\int_0^{r-\Delta r} \alpha(r')\,dr'). \tag{3.2.4}$$

Taking the ratio of the two equations and solving for $\beta(r-\Delta r)$ we get

$$\beta(r-\Delta r) = \beta(r)\frac{NRB(r-\Delta r)}{NRB(r)}\exp\left(-2\int_{r-\Delta r}^{r}\alpha(r')\,dr'\right) \qquad (3.2.5)$$

which shows that if there is a multiplicative error in the first calculation of β, at altitude r, then that error will be present in all values of β at altitudes below, as the algorithm proceeds. The inward Fernald two-component solution is basically the same, except the two components are identified separately. Thus an error in the first determination of β_A will propagate through the rest of the inversion and may well cause a substantial error in C as determined from the inversion. After all, the noisiest *NRB* data (most uncertain) are at the highest altitudes, so the first calculation of β_A is most likely to be in error. The source of the discrepancy in the values of C is actually in the first step of a Fernald inward inversion (3.1.10) where one finds the value of β_A one altitude step below the assumed top-of-aerosol ($\beta_A = 0$). One has a value of β_A *and* a value of C, one of which is derived from the other by way of the many (assumed) aerosol-free high-altitude data points. From this information one may easily determine what value the *NRB* data point at the top-of-aerosol should have if there were no noise:

$$NRB_{no\,noise}(n_c) = C\,\beta_R(n_c)\exp\left(-2\left(\beta_A + \beta_R(n_c)\right)\right). \qquad (3.2.6)$$

But the actual value of $NRB(n_c)$ generally will be different, due to noise, etc. Equation (3.1.10) effectively uses the ratio of $NRB(n_c)$ to $NRB(n_c\text{-}1)$ (and the assumed value of S_A) to find the value of $\beta_A(n_c\text{-}1)$, but this is over-constrained. The assumption that n_c is above all aerosol, together with $NRB(n_c\text{-}1)$ and the assumed values for β_A and C, *determines* $\beta_A(n_c\text{-}1)$ without the use of $NRB(n_c)$. If one is to invert the data assuming a value of n_c to

be above all aerosol, that is, such that $\beta_A(n_c) = 0$, then one may not also use a value of $NRB(n_c)$ that disagrees with this assumption to find $\beta_A(n_c\text{-}1)$. Thus, the algorithm is modified such that the value of $\beta_A(n_c\text{-}1)$ is found without using the value of $NRB(n_c)$. We take the *NRB* lidar equation at n_c-1:

$$NRB(n_c - 1) = C\,(\beta_A(n_c - 1) + \beta_R(n_c - 1))\exp(-2\,(\tau_A(n_c - 1) + \tau_R(n_c - 1))\,). \tag{3.2.7}$$

Now τ_A is numerically integrated (trapezoidally) from (3.1.12) as follows:

$$\tau_A(n) = \sum_{m=1}^{n} \frac{\beta_A(m) + \beta_A(m-1)}{2}\,(r_m - r_{m-1}) \tag{3.2.8}$$

so that

$$\tau_A(n_c) = \sum_{m=1}^{n_c} \frac{\beta_A(m) + \beta_A(m-1)}{2}\,(r_m - r_{m-1}) \tag{3.2.9}$$

and so

$$\tau_A(n_c) = \tau_A(n_c - 1) + \frac{\beta_A(n_c) + \beta_A(n_c - 1)}{2}\,\Delta r. \tag{3.2.10}$$

But $\beta_A(n_c) = 0$ by the assumption that n_c is above all aerosol, and $\tau_A(n_c) = \tau_A$, so

$$\tau_A = \tau_A(n_c - 1) + \frac{\beta_A(n_c - 1)}{2}\,\Delta r \tag{3.2.11}$$

What (3.2.11) says is that since $\tau_A(n_c\text{-}1)$ is the AOD from the surface to the *center* of bin number n_c-1, and so $\tau_A(n_c)$ is slightly larger, even though $\beta_A(n_c) = 0$ by assumption, because it includes the upper half-bin of aerosol extinction from bin number n_c-1. But this is a tiny difference: if $\tau_A(n_c\text{-}1) = 1$ km^{-1}, which is larger than ever seen on the ACE-Asia cruise even at the surface, the absolute error in τ_A is 0.0375. At an altitude just

below the altitude where $\beta_A = 0$, we can expect it to be *much* smaller (at least 100 times), so we ignore it, and say

$$\beta_A(n_c - 1) \approx \beta_A . \tag{3.2.12}$$

Substituting this in (3.2.7) gives

$$NRB(n_c - 1) \approx C\,(\beta_A(n_c - 1) + \beta_R(n_c - 1))\,\exp(-2\,(\beta_A + \beta_R(n_c - 1)))\,. \tag{3.2.13}$$

This gives us

$$\beta_A(n_c - 1) = \frac{NRB(n_c - 1)}{C}\ \exp(2\,(\beta_A + \beta_R(n_c - 1)))\,\approx\,\beta_R(n_c - 1). \tag{3.2.14}$$

Equation (3.2.14) gives us a value of $\beta_A(n_c\text{-}1)$ calculated from β_A, C, and the $NRB(n_c\text{-}1)$, *without* using $NRB(n_c)$. This value is used instead of the normal Fernald value, and produces extinction and backscatter profiles that when used to reconstruct the *ABS* data give a value of C that agrees with the known value. The name "*C*-matching" comes from the fact that the value for C implied by the inversion (below n_c) must match the value implied by the aerosol-free data (above n_c) or the value of C determined by independent calibration at another time. As a check on whether the top-of-aerosol assumption is correct for a given n_c, the value for $NRB(n_c)$ that would be required with no noise is calculated using (3.2.5). If the resulting value differs from the actual measured value by more than one standard deviation, the inversion is rejected as being invalid, n_c is increased by one, and the process repeated (see section 3.2.5 Automatic Inversion).

3.2.4 Invalid Inversions

Regardless of how one obtains extinction and backscatter profiles from a lidar profile, one may classify certain inverted profiles as "invalid" based on physical grounds. I have used four such conditions for rejecting an inversion and refer to them as "under-Rayleigh", "off-Rayleigh", "negative-extinction" and "no-*C*-match".

After the best value for *C* for a given *NRB* profile has been determined, the "attenuated Rayleigh *NRB* profile" can be computed. This is the *NRB* signal expected from an aerosol-free atmosphere, but attenuated by the known aerosol extinction, that is, multiplied by exp(-2τ_A). It is just the attenuated Rayleigh *ABS* profile times *C*. If the *NRB* data at a given altitude below the assumed top-of-aerosol is significantly less than the attenuated Rayleigh *NRB* at that altitude, then something must be wrong. This is because a real lidar signal can never be less than the theoretical signal from an aerosol-free atmosphere attenuated by the aerosol extinction:

$$NRB(r) = C(\beta_R(r) + \beta_A(r))\exp(-2\int_0^r(\beta_R(r') + \beta_A(r'))dr') \geq$$
$$C\beta_R(r)\exp(-2\int_0^r\beta_R(r')dr')\exp(-2\tau_A) \qquad (3.2.15)$$

or (dividing the left side by the right)

$$\frac{\beta_R(r) + \beta_A(r)}{\beta_R(r)}\exp(2\int_r^\infty\beta_A(r')dr') \geq 1. \qquad (3.2.16)$$

Whenever an inversion is computed, it is rejected if the *NRB* data at any point below n_c is "under-Rayleigh" by more than three standard deviations of the *NRB* data at that point, plus one percent (to allow for some error in overlap or Rayleigh calculations when the noise is very low, as at night).

Similarly, if one has found or assumed a top-of-aerosol altitude and a *C* value for a given *NRB* profile, then if the *NRB* data is greater or less than the attenuated Rayleigh *NRB* profile by more than three standard deviations plus one percent (as before) of the data at any altitude above the top-of-aerosol, the inversion is rejected. This is referred to as "off-Rayleigh".

After an inversion has produced an extinction profile, sometimes the aerosol extinction at some *r* will actually be negative, which of course is physically impossible without light emission. Thus, in this analysis, the inversion will be rejected if the extinction is negative by more than three standard deviations of the aerosol extinction plus one-quarter the Rayleigh extinction at that altitude. The standard deviation of aerosol extinction at a particular altitude is determined for this purpose by

$$SD_{\beta_A}(n) = \sqrt{\left[SD_{NRB}(n+1)\frac{\partial \beta_A(n)}{\partial NRB(n+1)}\right]^2 + \left[SD_{NRB}(n)\frac{\partial \beta_A(n)}{\partial NRB(n)}\right]^2}. \qquad (3.2.17)$$

The derivatives are found analytically from equation (3.1.10), multiplied by S_A. $SD_{\beta A}(n)$ is a measure of the uncertainty in the aerosol extinction which is due solely to the noise in the data, not the assumed values of *C*, β_A, top-of-aerosol, or the aerosol extinction at other altitudes. The one-quarter Rayleigh extinction allowance is added to allow for some small negative excursions when the noise in the data is particularly low, such as at night. Failure of an inversion on the basis described above is referred to as "negative-extinction" for obvious reasons. The figure of three standard deviations for negative extinction, under-Rayleigh and off-Rayleigh was arrived at by finding the most consistent inversions of noisy pseudodata as in Table 3.2.1 (see section 3.2.5).

The fourth way an inversion is considered invalid is if the *C*-matching implies that $NRB(n_c)$ is different from the value required by *C* and $\square_A$ by more than one standard deviation, as mentioned above in section 3.2.3.

3.2.5 Automatic Inversion

With these definitions in mind, I have implemented an algorithm for determining the best values for top-of-aerosol, *C* (or $\square_A$), and S_A for a given *NRB* profile, which involves inverting the data several (sometimes many) times before deciding on the best result. This "automatic" inversion algorithm begins with an *NRB* profile and an independent value for either *C* or $\square_A$. It then assumes the lowest altitude point (nearest-range bin) to be the top-of-aerosol, and finds either $\square_A$ or *C*, whichever is not given. If the resulting value is physically unlikely (invalid inversion), it assumes the next-higher point to be the top-of-aerosol and repeats the calculations. This process continues until an altitude is reached that gives an inversion that is valid, meaning *C* and $\square_A$ are physically possible and produce no under-Rayleigh or off-Rayleigh conflicts, *C*-matching works, and the resulting extinction profile has no negative-extinction conflicts. However, this first "valid" inversion may not be the best possible constant-S_A inversion.

3.2.6 RMS Negative Deviation

If an inversion is started several altitude steps above any significant aerosol, one would expect to obtain zero aerosol extinction for the highest several altitudes. With noise in the data, one would expect small positive and negative excursions at altitudes at which there is actually no significant aerosol. Even at altitudes below aerosol layers, there may well be ranges for which there is no significant aerosol, and one would expect

small positive and negative values of extinction here as well. In order to decide if a valid inversion is really started from above any significant aerosol, and noise is not introducing an unexpectedly large error, a quantity called "RMS negative deviation" is introduced. It is defined as the square root of the mean of the squares of those values of aerosol extinction which are negative divided respectively by their expected standard deviations due to data noise only.

$$RMS\ Negative\ Deviation \equiv \sqrt{\sum_{0}^{n_c} \left[\frac{\sigma_A(n)}{SD_{\sigma_A}(n)} \right]^2}, \sigma_A(n) < 0. \qquad (3.2.18)$$

After reaching an altitude which when considered as the top-of-aerosol gives a valid inversion, the algorithm continues up 12 more altitude steps (a total range of 1 km), one step at a time, at each step taking that altitude as the true top-of-aerosol and reinverting, then computing the RMS negative deviation for each valid inversion. One would expect the best value of RMS negative deviation to be one, assuming that n_c is a few steps above the aerosol and that the noise will produce some small negative values for σ_A, but tests with noisy pseudodata indicated a value of 0.4464 gives best recovery of extinction and lidar ratio (see below). The valid RMS negative deviation values are scanned for the value closest to the target value of 0.4464, and the corresponding top-of-aerosol point is chosen as the best. In other words, the algorithm searches for the valid inversion which best distributes the errors due to noise at altitudes where there is no significant aerosol. This is a good indicator of being above all aerosol, and not choosing a starting altitude that has an especially large noise deviation. The inversion using that top-of-aerosol is repeated and the results saved, completing the automatic inversion.

Below are some graphs of simulated data (pseudodata) and inverted extinction profiles. Figure 3.2.2 shows a noise-free simulated *NRB* profile obtained from the trapezoidal aerosol extinction profile shown in Figure 3.2.3 (black trace) with $S_A = 30$ and $\square_A = 0.525$, and the same *NRB* data with range-corrected white noise added to simulate actual noisy data. The noise added produces a signal to noise ratio of 144,000 at 94.5 m (the lowest bin) but only 1.55 at 6 km. Figure 3.2.3 shows the recovered extinction using the Fernald constant-S_A algorithm, with the smoothing filter but no *C*-matching, and without automatic inversion. The top-of-aerosol was set to 5.6445 km ($n_c = 75$). The recovered S_A was 45.7, a 52% error. With the smoothing filter off no valid inversions were found, even though the larger standard deviation of the unsmoothed data was used. Also shown in Figure 3.2.3 is the recovered extinction using automatic inversion including smoothing and *C*-matching. The recovered S_A was 27.5, an 8.3% error.

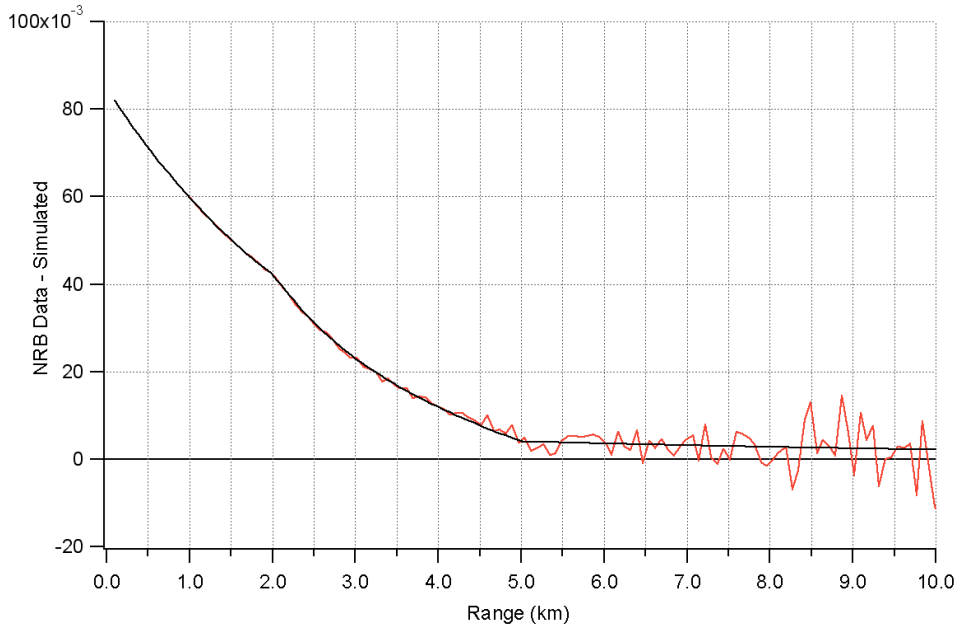

Figure 3.2.2 Simulated *NRB* pseudodata for the aerosol extinction profile in Figure 3.2.3 with noise (red trace) and without (black trace). $S_A = 30$, standard Rayleigh atmosphere..

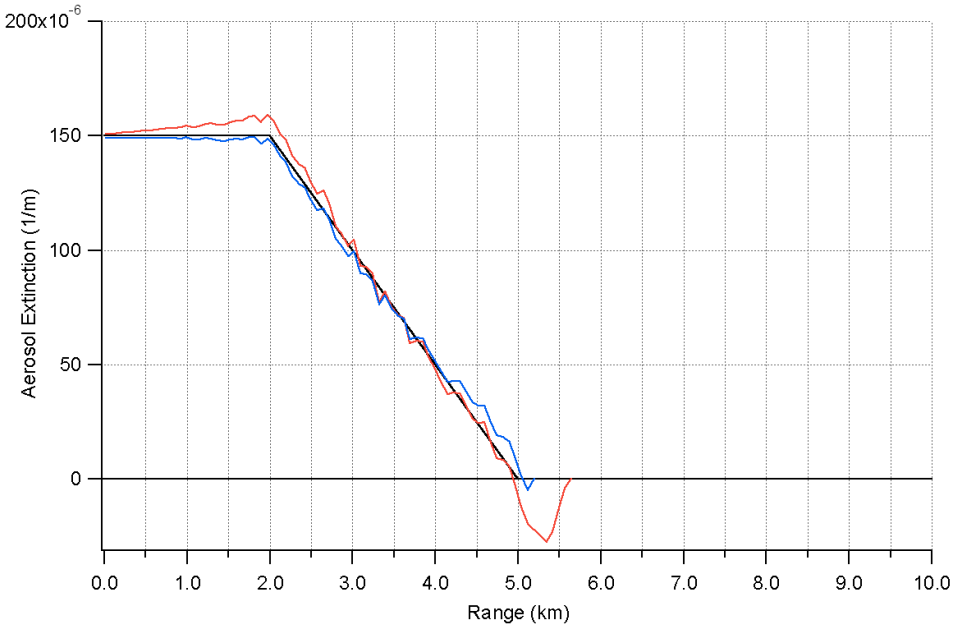

Figure 3.2.3 Assumed noise-free aerosol extinction profile (black trace) for pseudodata and recovered extinction profiles (standard inversion in red, automatic inversion in blue).

Note that even when S_A was found to be 45.7, the recovered extinction is not too bad. But the result for the automatic inversion algorithm with *C*-matching is better, with half the RMS error in recovered extinction (0.00388 km^{-1} vs. 0.00764 $km^{-1)}$. 20 such pseudodata profiles were generated with new random noise each time. The target value of 0.4644 for the RMS negative deviation was found by first finding the values of RMS negative deviation for the 20 noisy pseudodata profiles that corresponded to the best recovered values of S_A, and then taking their mean, which was 0.4644. The pseudodata were inverted again with this target value and the results are shown in Table 3.2.1.

Trial_Number	Plain_Inversion	Smooth_Only	C_Match_Only	Smooth_and_C_Match	Automatic
1	31.09	33.69	30.36	30.34	30.61
2	48.27	45.69	30.19	30.19	26.74
3	30.03	38.19	27.14	27.14	32.58
4	102.82	39.82	34.17	34.09	32.77
5	5.87	19.07	22.05	21.91	24.97
6	55.53	27.18	37.13	37.16	35.98
7	63.09	35.48	29.16	29.16	27.52
8	32.15	30.63	30.84	30.63	26.56
9	22.87	15.42	27.52	27.54	27.99
10	20.00	16.17	22.50	22.49	23.59
11	32.51	31.93	27.81	27.82	27.49
12	6.11	38.47	31.61	31.29	34.73
13	3.80	35.90	28.60	28.61	33.83
14	55.94	32.83	40.42	40.45	39.53
15	29.40	18.32	29.40	29.80	30.01
16	94.53	59.20	28.85	28.93	31.53
17	2.45	17.86	31.58	31.62	29.10
18	26.09	31.07	24.41	24.39	24.35
19	69.14	51.49	41.65	41.65	33.85
20	12.89	29.02	29.99	29.90	29.89
Mean	37.23	32.37	30.27	30.26	30.18
Standard Deviation	28.82	11.68	5.09	5.09	4.19

Table 3.2.1 Recovered lidar ratio for noisy pseudodata using various inversion algorithms, target $S_A = 30$.

Automatic inversion is best. Furthermore, it seeks out the top-of-aerosol without requiring visual inspection. *C*-matching seems to do as well as smoothing *and C*-matching, yet without smoothing much actual data produce unstable inversions and automatic inversion is nearly impossible. Although aerosol extinction is our primary goal, lidar ratio is also an important parameter, and more sensitive to errors in *C*. Thus recovery of lidar ratio was used as the criterion here. Of course, with very low noise, all of the algorithms work well, as the pseudodata were constructed and then inverted with a constant lidar ratio.

3.2.7 Variable Lidar Ratio Inversions

When other information about the aerosols is available, one may improve the results of inversion by allowing S_A to vary with altitude in a realistic manner. One can modify the Fernald solution (equation (3.1.10)) to obtain the variable-S_A version:

$$\beta_A(n-1) = \frac{NRB(n-1)\exp((S_A(n)-S_R)\beta_R(n)+(S_A(n-1)-s_R)\beta_R(n-1))\Delta r)}{\frac{NRB(n)}{\beta_A(n)+\beta_R(n)}+(NRB(n)S_A(n)+NRB(n-1)S_A(n-1)\exp((S_A(n)-S_R)\beta_R(n)+S_A(n-1)\beta_R(n-1))\Delta r)\Delta r}-\beta_R(n-1). \quad (3.2.19)$$

But how does one decide what the S_A profile should be? One approach is based on the availability of surface extinction data from an independent source. Such data are available from the ACE-Asia cruise of the R/V Ron Brown, and are used in Chapter 4 to constrain the inversion to return the given surface extinction with a constant lidar ratio in the boundary layer, and a different constant lidar ratio in upper layers. The selection of layers heights is made by visual inspection of constant-S_A extinction profiles, and could be automated in the future. The algorithm varies the ratio of upper-to-boundary layer S_A values in a loop outside of the AOD loop. Generally, the *NRB* profile is inverted from the top-of-aerosol altitude determined by an automatic constant-S_A inversion, although the automatic algorithm can be used with a variable lidar ratio. Although only a crude approximation to the true lidar ratio profile, this approach can nonetheless offer important information about upper-level aerosols. It provides a more accurate estimate of extinction, and the lidar ratio (which is itself an optical property of aerosols) can, with other data, help estimate aerosol types and properties. For instance, in the mid-visible range (about 500 nm) clean marine aerosol tends to have S_A near 20 - 35 sr (depending in

part on RH) [Ackermann, 1998, Doherty et al., 1999], dust S_A is 35 - 40 sr [Menzies et al., 2002], and continental aerosol typically has S_A between 50 and 80 sr [Doherty et al., 1999].

3.2.8 Error Analysis

The data collected during ACE-Asia were recorded in one-minute averages. The data are usually further averaged over one-hour periods, and at the same time the standard deviation of the mean data for each range is calculated. As the inversions are typically constrained by an independent measurement of AOD, the error in that measurement should also be included. We assume that the error in AOD is Gaussian-distributed with a standard deviation of 0.02. Because of the complexity of the inversion process, it was decided to estimate the errors involved in the lidar signal analysis by the Monte Carlo method. The averaged data are inverted as is, then each data point is adjusted upward or downward by one standard deviation for that range, The AOD, if from an independent measurement, is also adjusted upward or downward by one standard deviation. If inverting from a given value of C, that value is adjusted up or down by one standard deviation. The adjusted data are inverted and the differences from the original results are computed. This process is repeated 200 times and the resulting differences are accumulated. Finally the RMS errors in extinction and S_A are computed and saved. These errors may be interpreted as one-sigma values. Note that these errors are only due to random errors in the data and AOD measurements, not due to assumptions such as whether to use a constant S_A value with altitude, or what height is considered the top of aerosol.

Ch. 4. ACE-Asia Calibrations

The NOAA Research Vessel Ronald H. Brown (R/V Ron Brown) was prepared for her participation in ACE-Asia in Pearl Harbor, Hawaii, between March 8 and March 14, 2001. During that period, the two micropulse lidar systems (numbers MPL 005 belonging to the University of Miami and MPL 016 belonging to NASA Goddard Space Flight Center) were unpacked from their shipping crates and assembled at a hotel in Honolulu. Afterpulse data was taken for both systems, and then both were in turn directed horizontally off the hotel balcony over the ocean at a height of approximately 30 m above sea level. Elevation was determined with a precision protractor (electronic tilt meter) accurate to 0.1 degrees. These data were collected for overlap correction, and it was done at night to reduce solar noise. The resulting data files were saved for later processing.

MPL 005 was then installed on the ship near the bow, clear of exhausts and superstructure, in a small van equipped with an optically flat window in the roof for the MPL. The van contained several vacuum pumps for other instruments not related to the MPL. These pumps generate substantial heat, so the van was equipped with an air conditioner. The heat generated by the pumps combining with the intermittent failure of the air conditioner eventually led to the total failure of MPL 005 at 08:30UTC on

Figure 4.1 Micro Pulse Lidar (MPL) installed in van aboard the R/V Ronald H. Brown during ACE-Asia. There is an optical window in the roof above the transceiver.

DOY 86. However, little useful lidar data had been collected up to that point as the weather had been stormy with heavy low clouds nearly all of the time. MPL 016 was installed and operated for the rest of the cruise during daylight and early evening hours only. It was felt that the risk of operating the only remaining MPL unattended outweighed the value of any night data that might be gathered.

Several attempts were made to obtain horizontal overlap data while at sea; however, the motion of the ship even in the calmest of waters made this effort largely unsuccessful. At the end of the cruise, more afterpulse and overlap data were taken while the ship was docked in Yokosuka, Japan, and this proved to be the best data for overlap determination.

4.1 Background Noise

For the processing of data for ACE-Asia, the average background noise for each deadtime-corrected data record (averaged over one minute) was determined by averaging the data over the range of 30 to 60 km, which contains virtually no photons from the laser due to the inverse-square falloff of such reflected photons and the general lack of return signal at such altitudes. The average background noise for each one-minute record was subtracted from all data points for that record. Occasionally this produces negative values, but these are small in magnitude and dealt with elsewhere.

4.2 Afterpulse Function

Afterpulse data for both systems were taken at 500 ns resolution at various times during the cruise for use in processing the data. The afterpulse data records were in sequence corrected for deadtime and background noise, divided by the pulse energy, averaged, and then fit to a high-degree polynomial to provide a smooth afterpulse function. The resulting afterpulse function for MPL 016 is shown in Figure 4.2.1.

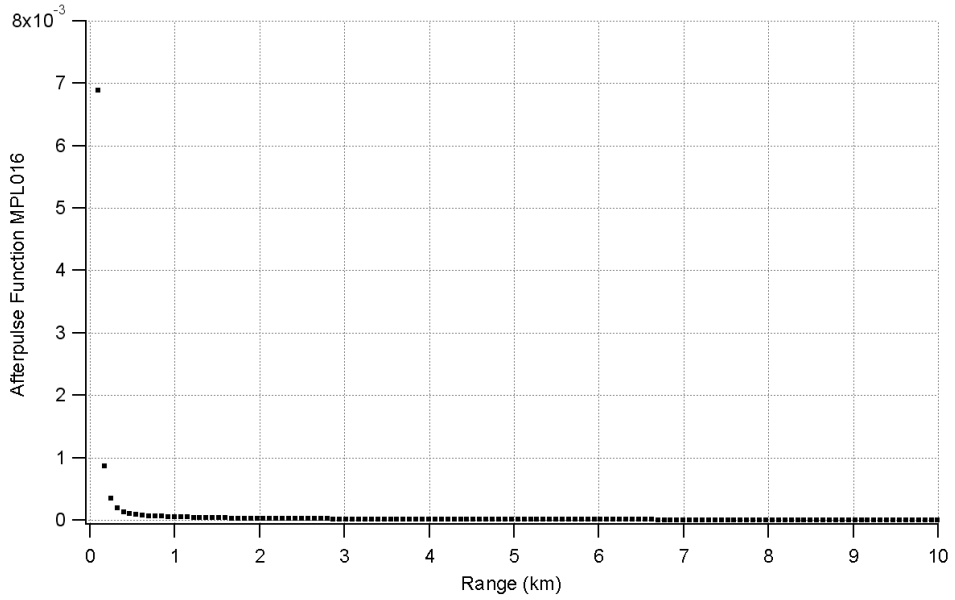

Figure 4.2.1 Afterpulse function for MPL system 016 (NASA).

Note that the bin 1 value of approximately 0.007 is much less than the typical bin 1 data for actual marine aerosols, which is about 3.8 - a factor of 0.0018 or 0.18%. This is for a situation for which the AOD was 0.08 (DOY 88.23 2001), a relatively clear day. The figure for bin 2 at the same time was 0.0011, and less for higher-numbered bins. Thus, the error introduced even if one *ignored* afterpulse correction is minimal (well less than 1%), and so the uncertainty when afterpulse correction *is* applied is at least an order of magnitude smaller and need not be considered in comparison to other sources of error.

4.3 Range-Offset

After the ACE-Asia cruise, it was decided to determine the range-offset of the MPL systems. It had previously been thought to be negligible, but in an effort to obtain the most reliable surface extinction data product possible, a closer look revealed that for thin but dense layers as often occurred in ACE-Asia, the range-offset could introduce significant errors. The laser system itself produces an RMS deviation in time for the emission of the outgoing pulse of approximately 50□s [Huang, 2002]. By directing the system into a black target at close range with a bin time of 200□s, one can more precisely determine the time of the outgoing pulse than with the standard bin time of 500□s. Afterpulse data for MPL system 016 were taken at Goddard Space Flight Center (GSFC) in Greenbelt, MD USA, where that system was located after the cruise. The data were recorded at 200 ns time-resolution (the greatest available resolution) and are shown (as mean with standard deviation error bars) in Figure 4.3.1. Although MPL system 005 failed during the cruise, some 200 ns data were available from before the cruise. These

data are also shown in Figure 4.3.1 (in red), and agree in shape quite closely with that from MPL 016, suggesting that the range offset is consistent among similar MPL systems. This older data (MPL 005) has been reduced in amplitude by a factor of three, which reflects the reduced afterpulse signal after a modification at GSFC (before the ACE-Asia cruise) intended to reduce afterpulse. It also contains some actual reflected atmospheric data (at t > 1000 ns), which is not relevant here.

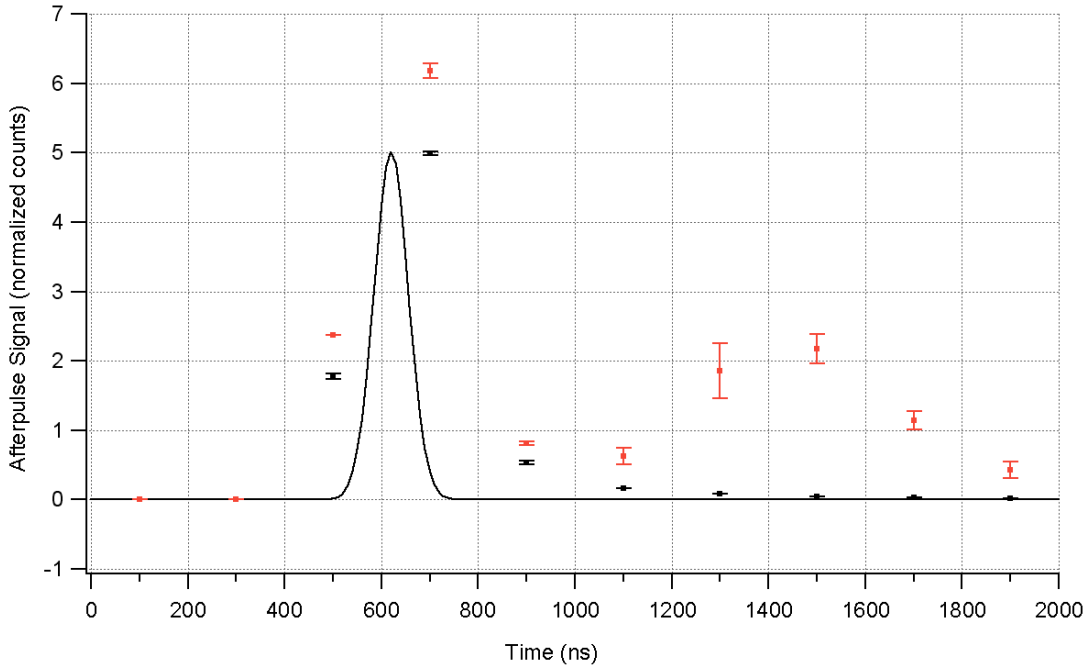

Figure 4.3.1 200 ns resolution afterpulse data for determining the actual pulse emission time (MPL 016 black, MPL 005 red), and best-fit Gaussian (black trace).

The new data were fit to a Gaussian with standard deviation 50□s integrated over the relevant 200 ns bins, and the result was a center of 620 +/- 50 ns. This is also shown in Figure 4.3.1. The areas under the Gaussian from 400 - 600 ns and from 600 - 800 ns stand in the ratio of the data at 500 ns (bin 3) to the data at 700 ns (bin 4). This corresponds to a delay of 380 ns between the mean time of pulse emission (during the second 500□s bin) and the start of the third 500 ns bin (at 1000 ns). As before, the data

in the second 500□s bin is not used, as the relatively large pulse leakage makes the remaining data quite uncertain. Thus, the first valid bin (the third at 500□s) contains data that begin 380□s after the actual pulse. This produces a range offset of 57 m +/- 7.5 m, which is not a huge error but can have a significant effect on the analysis of data in the lowest (nearest-range) bins. The main source of error in neglecting range offset is the omission of the extinction in the neglected range from calculations. For example, the optical depth of a uniform boundary layer of height 570□m (not uncommon) would be in error by 10%. Another error produced is reporting data products at altitudes 57□m lower than actual.

Based on the above results, the data reported in Chapter 5 were analyzed assuming that the first useable bin contains reflections from between 57□and 132□m beyond the lidar transceiver, and are reported as representing a range (or altitude) of 94.5□m. The lowest-altitude (surface or lidar altitude) extinction and backscatter values are taken to be the same as the first inverted data point at 94.5□m.

4.4 Overlap Function

As mentioned above, overlap data were taken at the end of the cruise while docked in Yokosuka, Japan. MPL 016 was directed horizontally over the harbor into a mild sea breeze. The conditions were such that one would expect nearly homogeneous aerosol properties in the horizontal plane. This data compared well (within a few percent) with that taken in Hawaii, and was used for overlap correction, as the atmospheric conditions for the Yokosuka data were better than those for the Hawaii data. The overlap records were recorded in 10-second averages, which were hand-selected to remove records which contained obvious reflections from ships or water. The near-

perfect exponentially decaying lidar return signal for ranges beyond 4 km confirmed horizontal homogeneity. The data were corrected for deadtime, background noise, afterpulse and range. As described in Chapter 2, range correction is the multiplying of the data for each range bin by the squared distance to the center of that bin. The range correction included the range offset determined above. The constant total extinction coefficient σ was found by fitting a straight line to the logarithm of the data beyond 4 km. Then the corrected horizontal data were divided by the best-fit exponential to find the overlap function. If there are errors in the range correction for near ranges, they will be corrected by the overlap function, and when the overlap function is used to correct actual data, the correction will be accurate for atmospheres varying slowly in the near range. Finally the overlap function is fit to a polynomial in the intermediate ranges (approximately 1 to 6 km) as the data are somewhat noisy there. The nearest ranges are not very noisy since the return signal is strong there. For the farthest ranges (> 6 km) the overlap function is set to one.

The selected, averaged, logged data (red) and best-fit line (blue) for MPL 016 are shown in Figure 4.4.1. The slope of the far range logged overlap data is determined by the line shown.

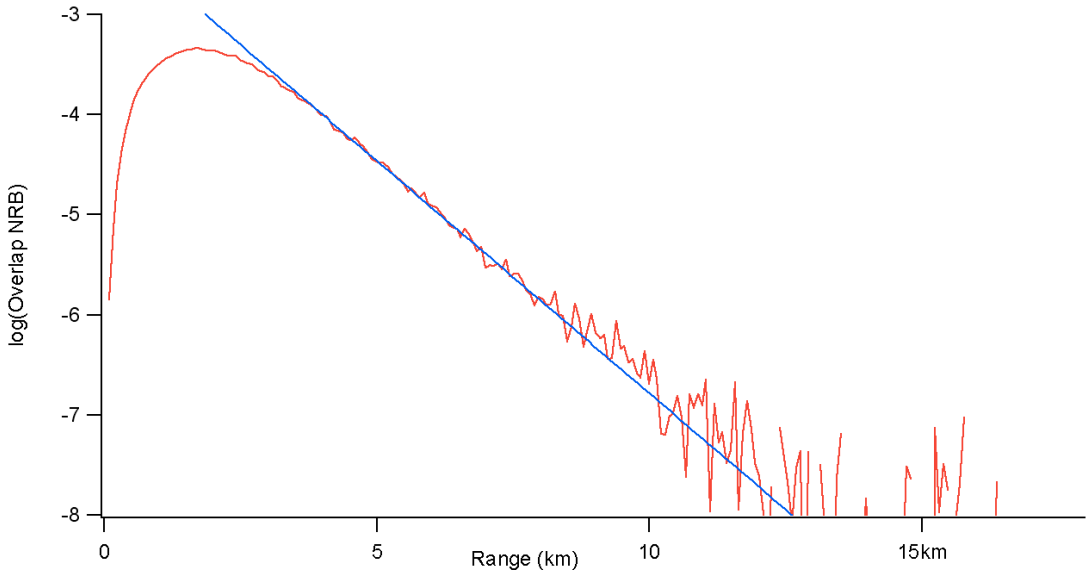

Figure 4.4.1 Logged horizontal data (red) and best-fit line to range > 5 km (blue).

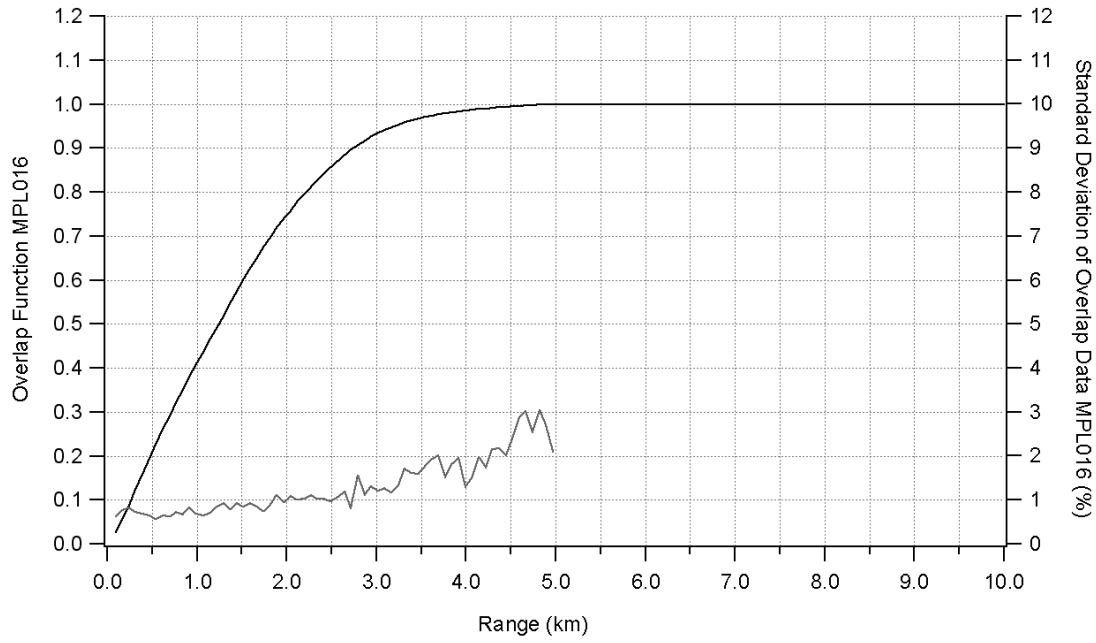

Figure 4.4.2 Overlap function used for MPL 016 data, and standard deviation of near-range overlap function.

The resulting overlap function and the percent standard deviation of the overlap data are shown in Figure 4.4.2. The standard deviation is only strictly relevant to the overlap

function for ranges less than 1 km. The chi-square for the fit from 1 to 6 km was 0.024 for 86 points, so the error there is less than the standard deviation shown. Long-term or temperature-related changes in the overlap behavior are possible and may add to the error. With the overlap function determined, all vertical data were corrected for deadtime, background noise, range offset, afterpulse, and overlap (producing *NRB* data) before being inverted.

4.5 Cloud Screening

NRB lidar data often include reflections from clouds. Usually, cloud signals are much larger than those from even the most dense aerosols, and may easily be detected by visual examination of a graph of *NRB* vs. altitude. Records with obvious thick cloud signals were rejected before averaging the remaining nearly cloud-free records. Occasionally, thin, high cirrus clouds would be apparent in the *NRB* data, and although they could conceivably be aerosol, they were rejected. Nonetheless, some cloud layers inevitably got through, as they were indistinguishable from aerosol layers in the *NRB* data. However, if the system constant *C* is known to a reasonable accuracy from other measurements close in time and free of clouds, the data can be inverted *below* the clouds, and can therefore yield a useful data product. Some data of this type are included in the data analysis and are so identified.

4.6 System Constant *C*

C was determined for each independent measurement of AOD, and was determined by automatic inversion with a constant aerosol lidar ratio (S_A). As previously mentioned, during the cruise there was difficulty maintaining proper temperature in the

lidar van due to the presence of vacuum pumps and a failing air conditioner. For each averaged *NRB* profile the maximum temperature inside the case of the lidar system was found, and the corresponding values found for *C* were plotted versus the maximum case temperature (Figure 4.6.1).

It was apparent that for lidar case temperatures above 23 degrees C the variation in *C* from the mean was much greater than for lower temperatures. These data points were rejected as unreliable, as were any other data from the entire cruise for which the case temperature exceeded 23 degrees C. The factors that determine *C* for the instrument include many of the same factors (mostly structural) that influence the overlap function, so it was felt that inverting these data would produce no valid results. They were rejected and the remaining points are shown in Figure 4.6.2.

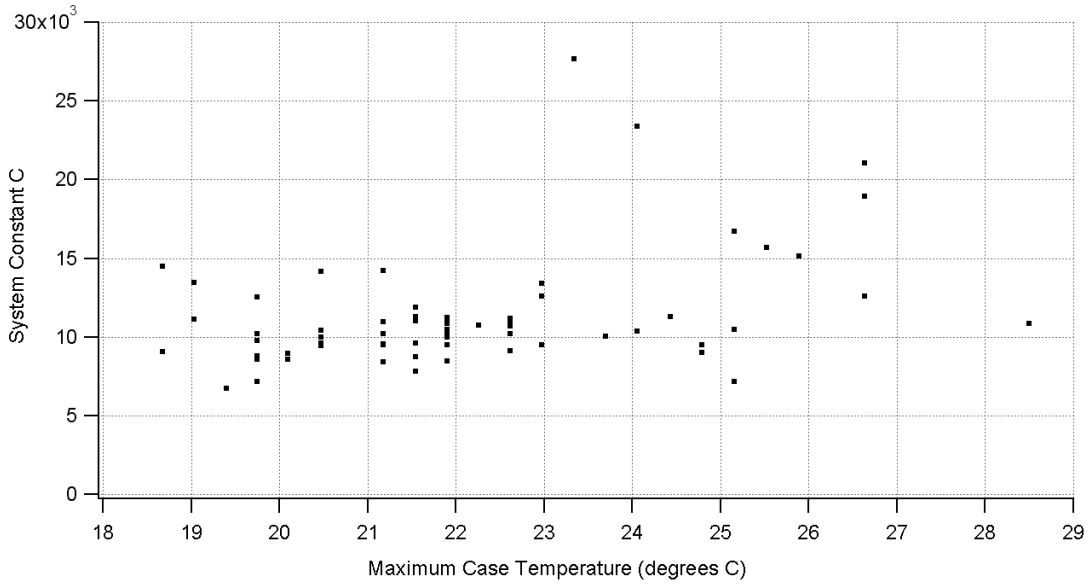

Figure 4.6.1 System constant *C* from independent AOD measurements vs. maximum lidar case temperature during measurement.

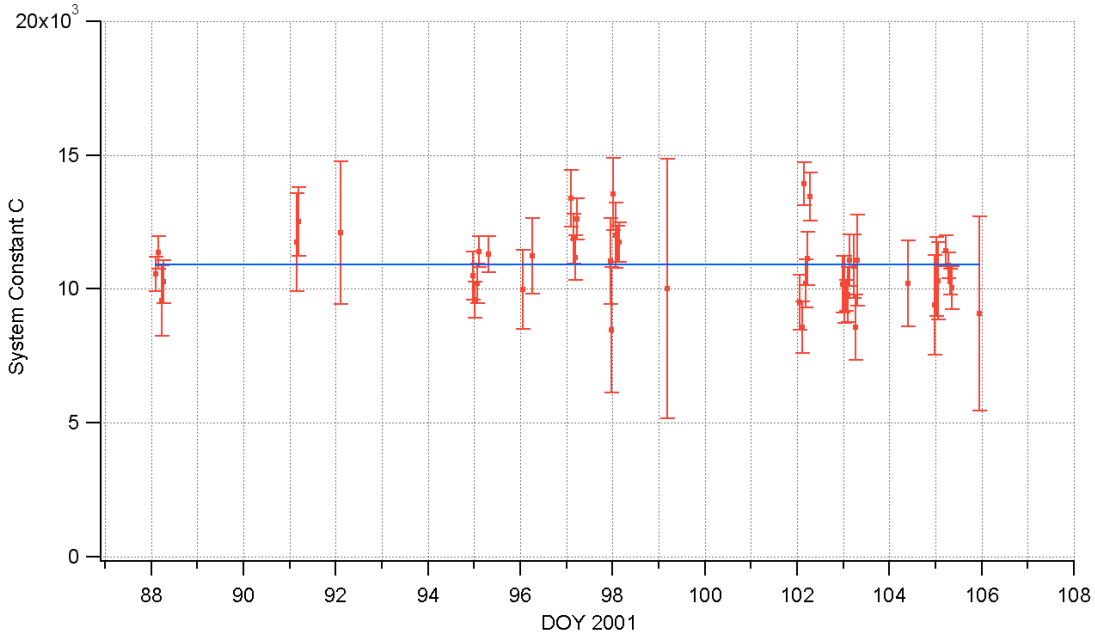

Figure 4.6.2 System constant *C* found from independent AOD measurements with lidar case temperature ≤ 23 degrees C during ACE-Asia cruise vs. DOY, and least-square-error value of 11049 +/- 213 (blue line).

It was found that the variation in *C* was within the uncertainty implied by the fit to the Rayleigh data and the typical error in the AOD measurements, which was taken to be +/- 0.06 (3 sigma) or sigma = 0.02. Consequently, it was assumed that the value of *C* would be treated as constant during the cruise within the uncertainty. The best mean value of *C* was found with a weighted least-squares fit and found to be 11049 +/- 213. This value was used for the rest of the analysis for all lidar profiles for which there was no independent AOD available. As a check I compared the measured AOD to the AOD calculated from the lidar data using the above value for *C*. The mean difference in AOD was 0.006 with standard deviation of 0.06.

Ch. 5. Analysis of Lidar Data from ACE-Asia

5.1 Overview of the Cruise

The ship sailed on March 14, 2001 (DOY 73) from Pearl Harbor, Hawaii, heading NNE until reaching approximately 34 degrees North latitude on March 18, (DOY 77), then turning due west. The ship continued west, approaching the southeastern coast of Japan on April 1, 2001 (DOY 91). As mentioned before, during this time there were little useful lidar taken due to bad weather. Also, the cold and rainy weather led to the failure of the cooling (air conditioning) system in the lidar van. Cooling was necessary to remove the heat from the vacuum pumps, as the van could not be left open to the elements. As a result the heat from the pumps led to the overheating and consequent total failure of the photodetector module in MPL 005 on DOY 86. For these reasons, only data from MPL 016 are presented here, spanning from March 27 (DOY 86) to April 1 (DOY 107). Fortunately, this was the more important part of the cruise, as our purpose was to collect data on aerosols associated with the annual Asian Spring dust storms. An outside view of the equipment setup is shown in Figure 5.1.1 and the cruise track is shown in Figures 5.1.2 – 5.1.4.

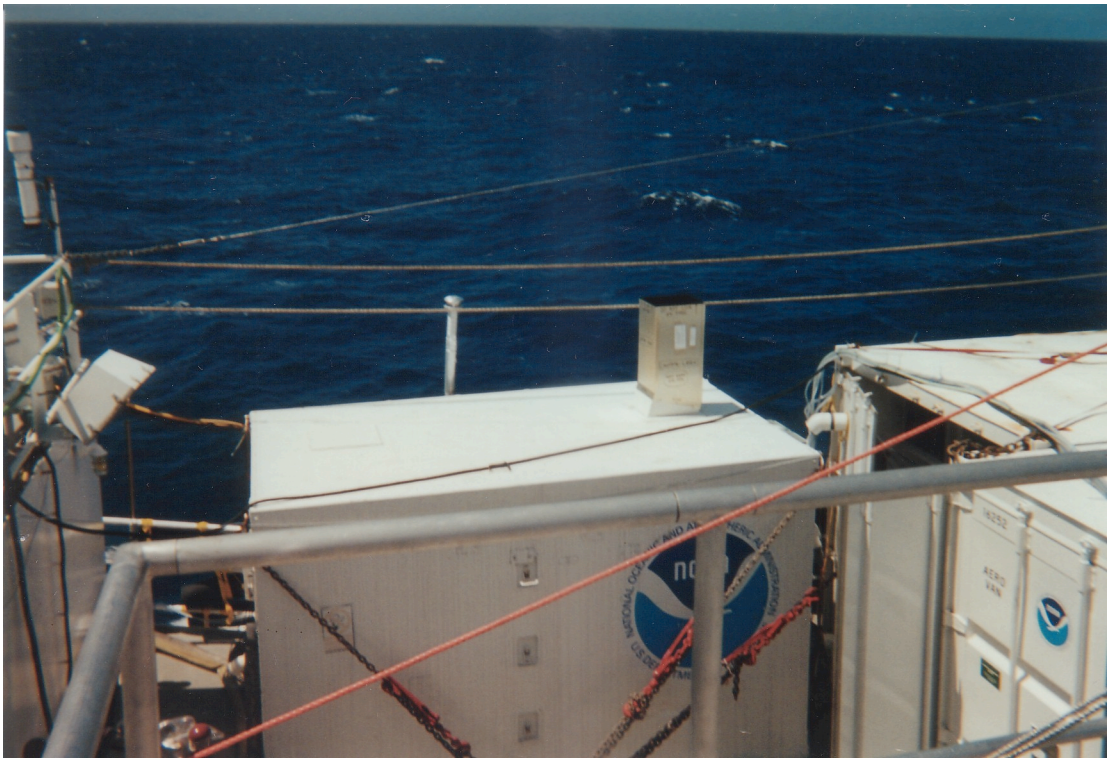

Figure 5.1.1 MPL setup, outside view of lidar van on R/V Ronald H. Brown.

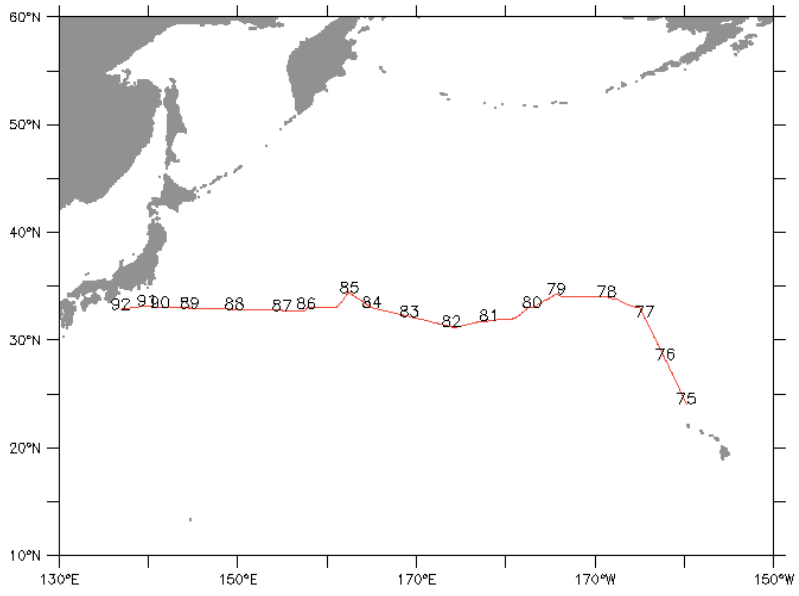

Figure 5.1.2 Cruise track: DOYs 75 – 92, 2001 (March 16 – April 2).

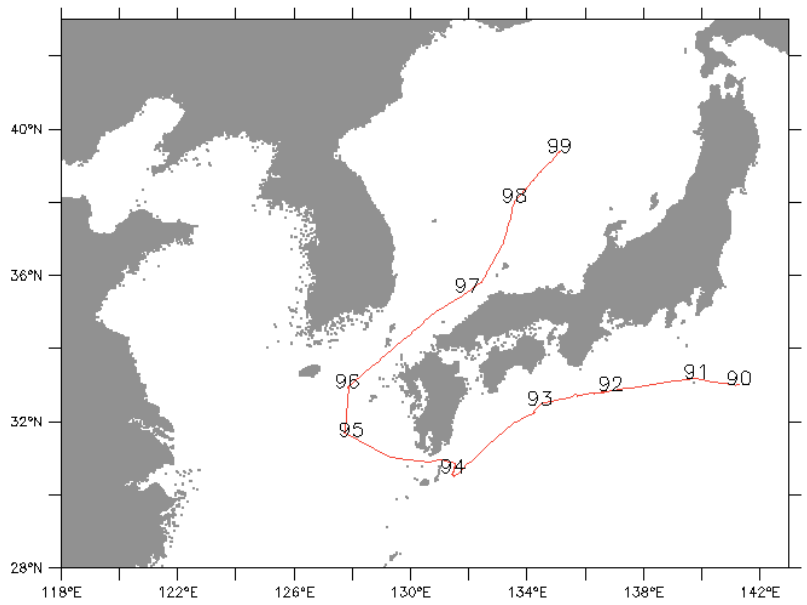

Figure 5.1.3 Cruise track: DOYs 90 – 99, 2001 (March 31 – April9).

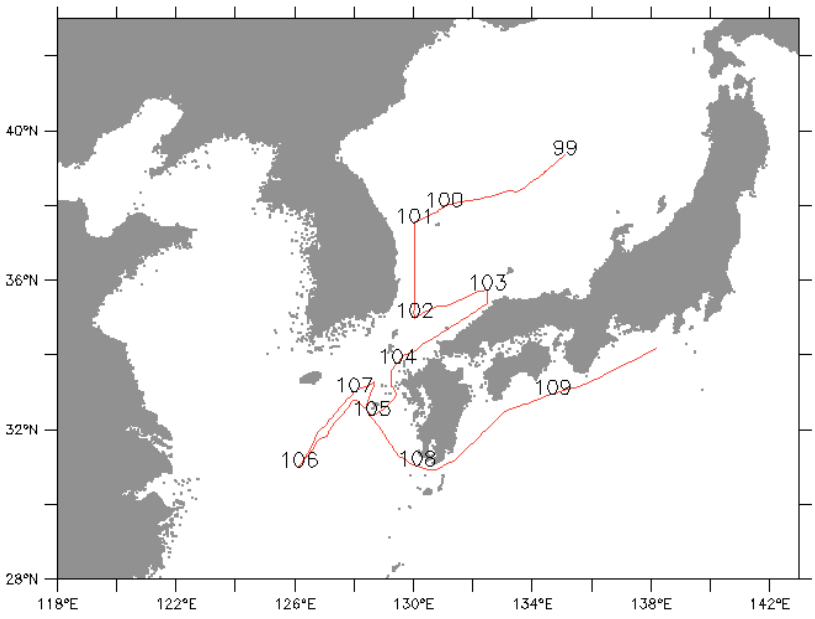

Figure 5.1.4 Cruise track: DOYs 99 – 109, 2001 (April 9 – April 19).

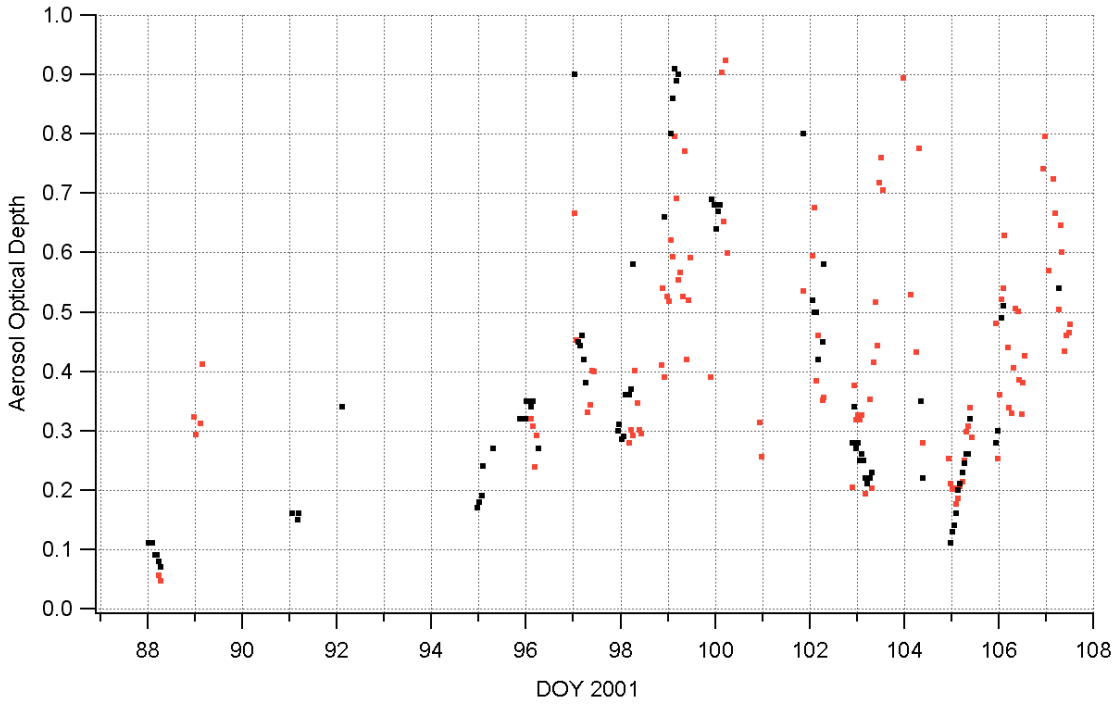

Figure 5.1.5 AOD (523 nm) from sunphotometer on ship (black) and lidar (red).

Figure 5.1.5 shows the aerosol optical depth during the cruise, starting as the ship approached Japan, from both sunphotometer and lidar-derived measurements. Starting with DOY 97 we see the sometimes very high values of AOD in and around the Sea of Japan during the dust event.

On the following page is an image plot of the *NRB* data from MPL 016 for the cruise (Figure 5.1.6). The aerosol extinction for the cruise is shown on the following page (Figure 5.1.7). In Figure 5.1.6 (*NRB*) one can see some reflections from thin cirrus clouds around 8-12 km. There are also some water clouds that are not apparent in the recovered aerosol extinction plot, because the *NRB* data were usually inverted using the best value of C for the cruise, not AOD, and the inversions were intentionally started below the clouds. Where there is black, either there were thick low clouds or it was night. As the ship approached Japan (DOY 89-92), increased backscatter is apparent in the figure.

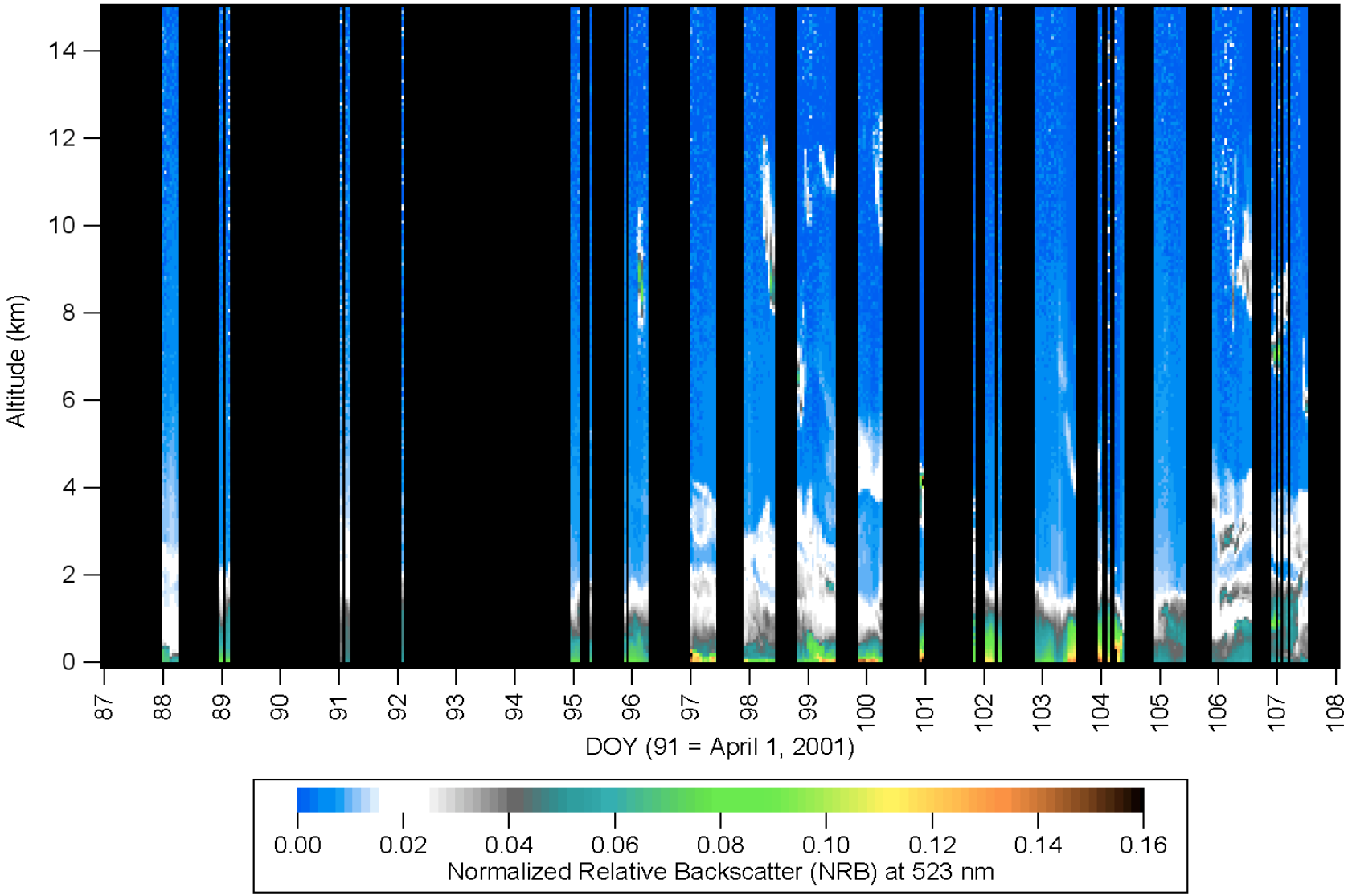

Figure 5.1.6 Vertical profiles of *NRB* lidar data for ACE-Asia cruise. Notice some high cirrus at 8-12 km despite cloud-screening.

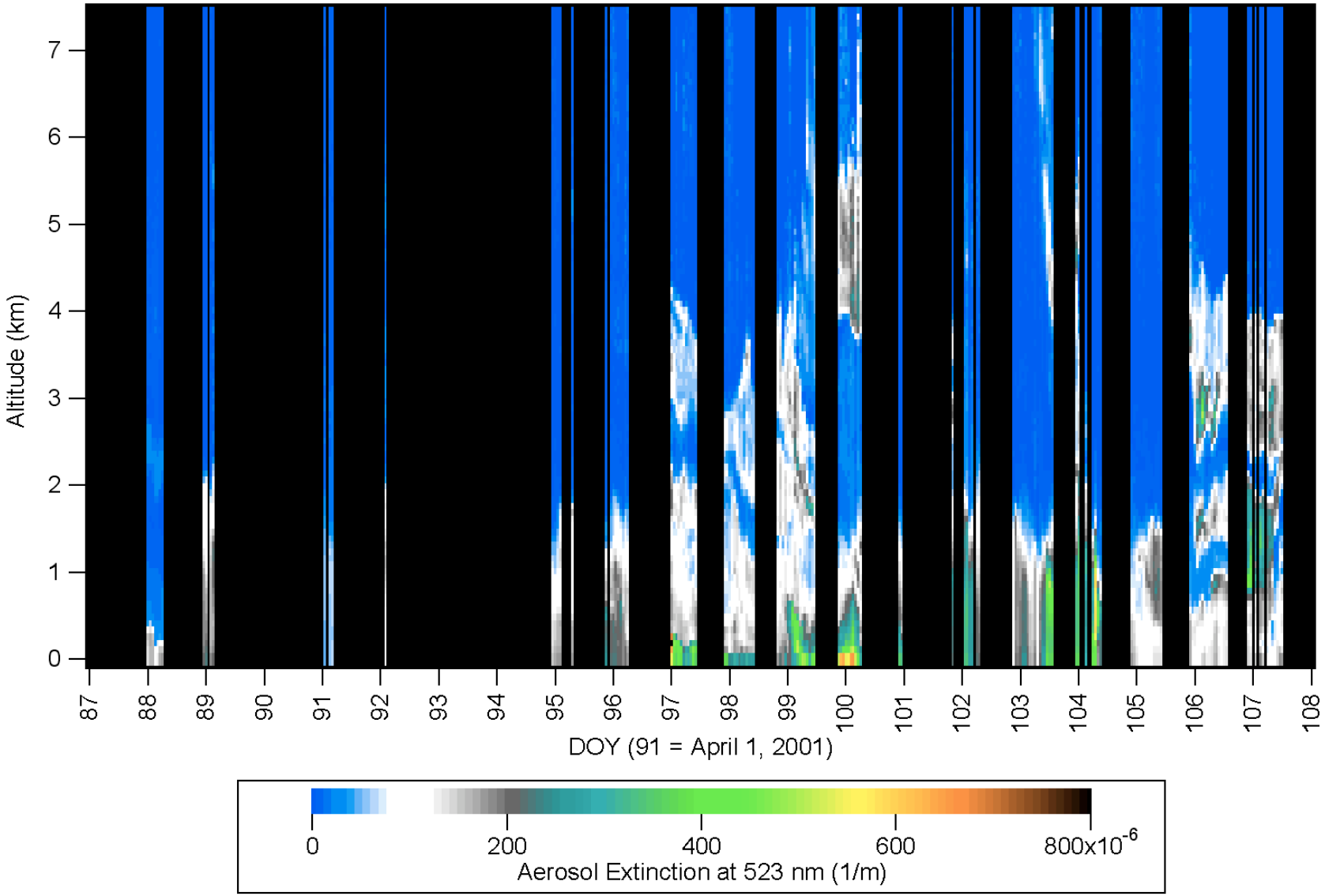

Figure 5.1.7 Vertical profiles of aerosol extinction at 523 nm from constant lidar ratio inversion of MPL data for ACE-Asia cruise.

The data in Figure 5.1.7 are the result of constant lidar ratio automatic inversions based on the system constant *C*. Again, as the ship neared Japan, we see increased aerosol. On DOY 88 there was a normal marine aerosol, with surface extinction of about 0.11 - 0.15 km^{-1}. On DOY 89, we see surface extinction of about 0.22 km^{-1}. On DOY 97-104 we see the highest surface extinction, with the maximum of around 0.60 - 0.70 km^{-1}. This was the period of extremely heavy soot and/or dust.

In order to better interpret the lidar data, I present here some data from other investigators on the Ron Brown. One way to constrain lidar inversions is by surface extinction. Figure 5.1.8 shows the surface extinction as measured independently of lidar on the ship during the cruise, together with the lidar surface extinction from constant lidar ratio inversions. The scattering data are from Dr. Christian Carrico of Colorado State University, who operated multiple nephelometers (TSI Inc., Shoreview, MN) aboard the Ron Brown at various RH levels to measure aerosol total scattering and hygroscopic growth. The data were taken continuously during the entire cruise, at wavelengths of 450, 550, and 700 nm. They are corrected for ambient temperature, pressure, and RH, and to 523 nm wavelength via an Angstrom exponent found from the 450 and 550 nm data. The absorption data are from Dr. Patricia Quinn of NOAA's Pacific Marine Environmental Laboratory (PMEL).

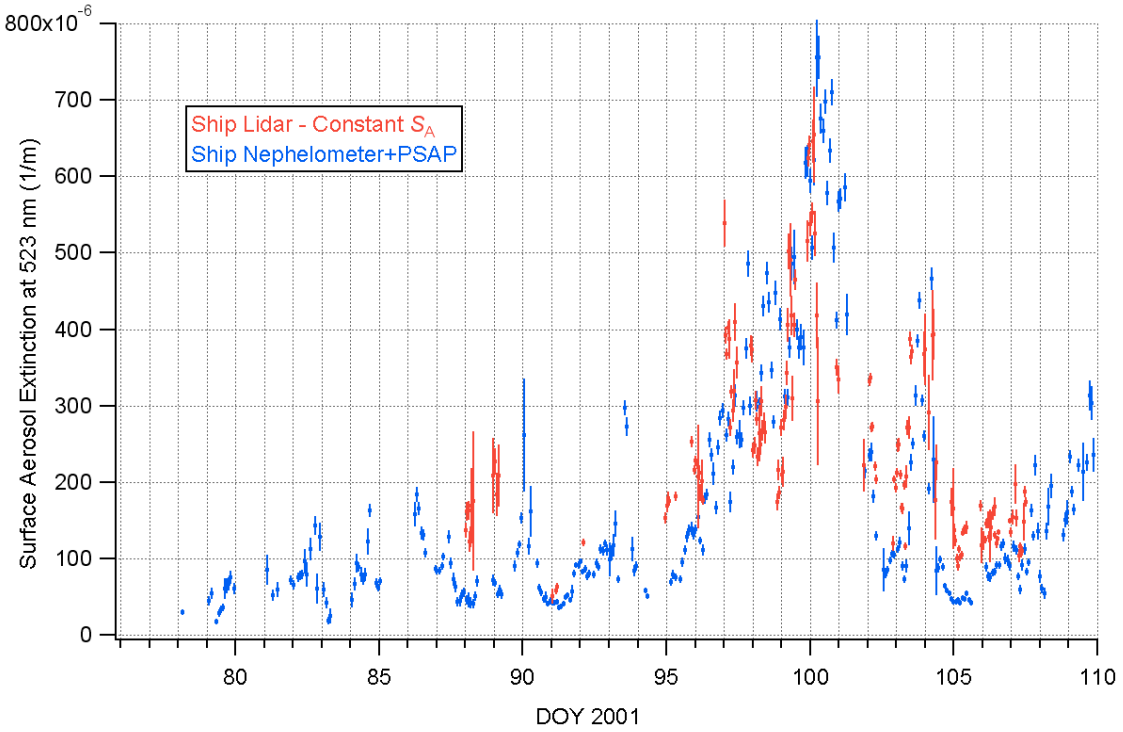

Figure 5.1.8 Surface aerosol extinction at 523 nm from MPL and ship air-sampling instruments.

Absorption was measured continuously during the cruise with a Particle Soot Absorption Photometer ("PSAP", Radiance Research Inc.) operating at a wavelength of 550 nm. The data were corrected for ambient temperature and pressure, and added to the scattering data. Figure 5.1.8 shows the surface extinction thus derived (blue) versus the surface extinction from constant-S_A lidar inversions (red). The general trends are in agreement. However, note that usually the lidar surface extinction is higher than the ship-based extinction, except for DOY 98-101 when the reverse is true. This suggests that before DOY 98 and after DOY 101 there was elevated aerosol with higher lidar ratio than at the surface, while from DOY 98-101 the surface aerosol had the higher lidar ratio. As expected, significant amounts of elemental carbon (soot) and dust (Asian desert) were measured during the cruise. Figure 5.1.9 shows the elemental carbon measured on the

ship, while Figure 5.1.10 shows the elements in the dust. These data are also from Dr. Quinn of PMEL. Clearly DOYs 101-104 show the highest dust levels at the surface, while DOYs 97-104 show the highest levels of black carbon, an indication of soot from fossil fuel combustion and/or biomass burning.

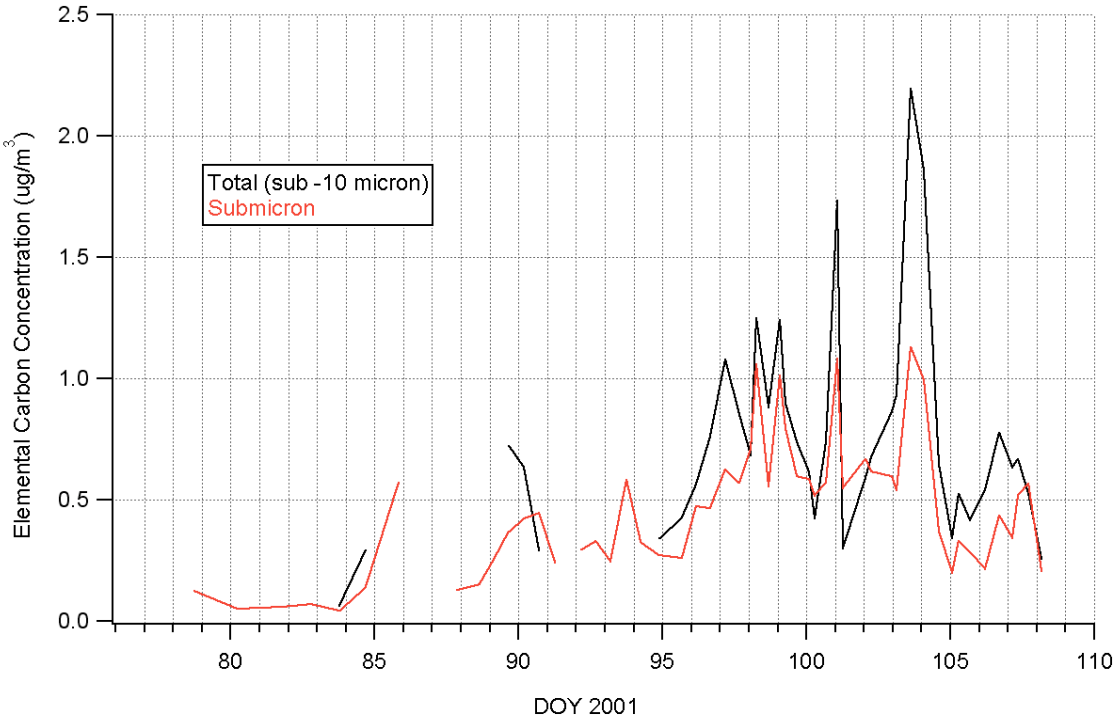

Figure 5.1.9 Elemental carbon from sampled air during ACE-Asia (Quinn).

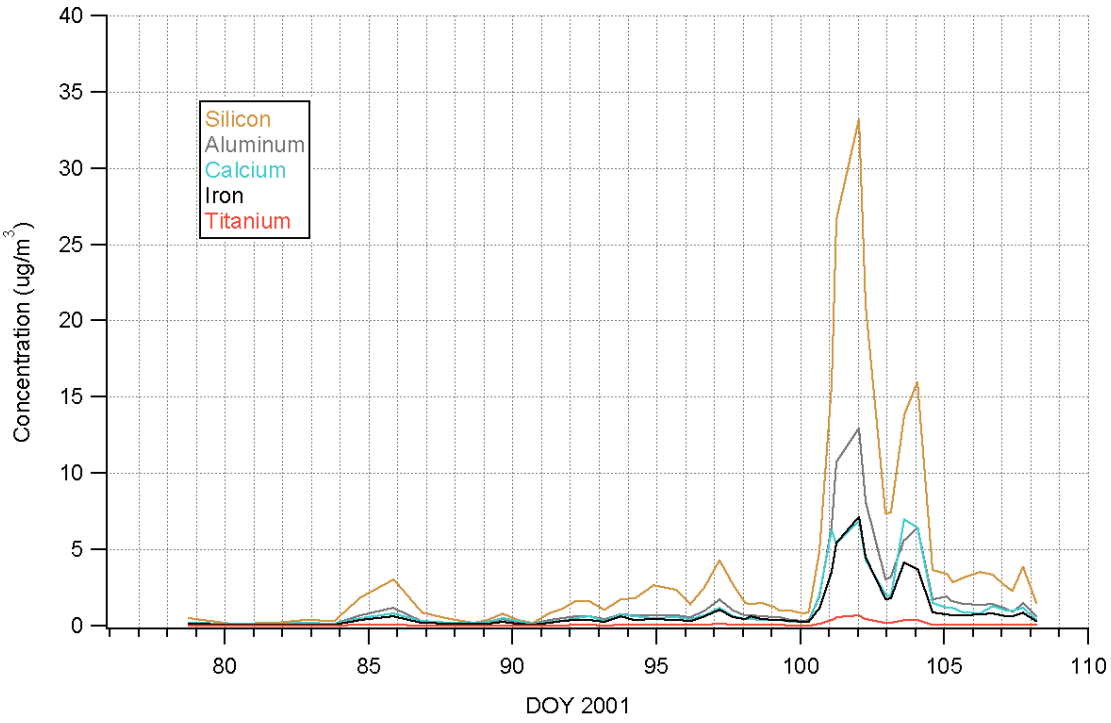

Figure 5.1.10 Dust element concentrations from sampled air during ACE-Asia (Quinn).

5.2 Discussion of Particular Cruise Lidar Data

In this section I present actual aerosol extinction profiles inverted with constant-S_A and variable-S_A. For each graph, the blue trace is the aerosol extinction, the gray traces are the Monte Carlo-derived standard deviation of aerosol extinction due only to variation in the data and uncertainty in the independent AOD measurement, C, or both, if used. The red trace is the surface-to-altitude AOD. The violet trace is the lidar ratio S_A. The green trace is the relative humidity and the black trace is the temperature, both measured by balloon radiosonde launched from the ship within one hour of the lidar data.

The general approach is to invert the data assuming a constant S_A, then choose an altitude to break the aerosol into two layers, one ("MBL") from the surface up to that altitude and the other ("upper-layer") above that altitude. Then we invert again, allowing each of the "layers" to have its own lidar ratio, and constraining the inversion algorithm to produce the same surface extinction as measured by the ship-borne nephelometers and PSAP. In some cases, the surface extinction matches within the uncertainty and a constant-S_A inversion is indicated. In most cases during ACE-Asia, the MBL lidar ratio needs to be adjusted downward to reconcile the lidar-derived surface extinction with that measured by the ship-borne nephelometers and PSAP. Consequently, the upper-layer lidar ratio must increase. We shall look at three representative days: DOYs 88, 98, and 100.

5.2.1 DOY 88 – March 29, 2001

On this day we saw a thin MBL with upper layers. The ship was approximately 500 km west of Japan. Figure 5.2.1a shows the results of a constant-S_A inversion for the data averaged over an hour near local noon (02:00 – 03:00 UTC, local = UTC + 10):

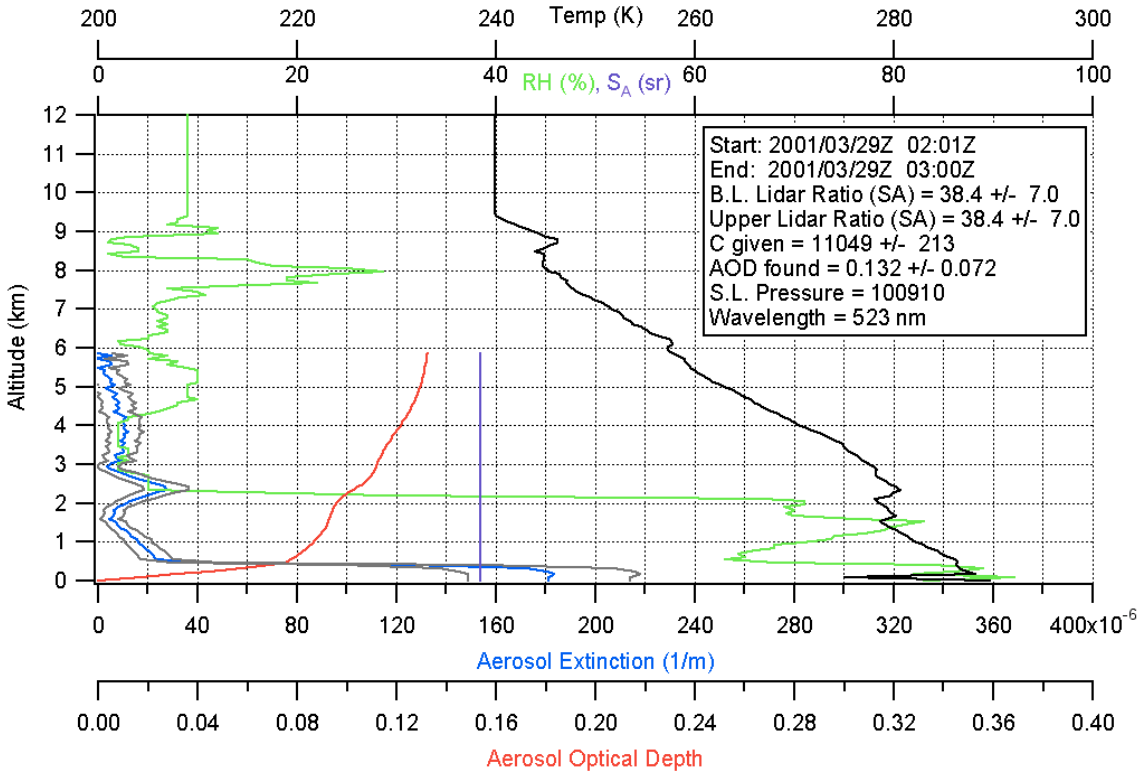

Figure 5.2.1a Constant-S_A inversion of lidar data averaged over an hour near local noon, DOY88 2001, 500 km west of Japan.

This inversion shows a surface extinction of about 0.180 km^{-1} with a column lidar ratio of 38.4 +/- 7.0, higher than expected for a clean marine aerosol. The ship-borne nephelometer (corrected for wavelength and RH) and PSAP data indicated a surface extinction at 523 nm of 0.046 +/- 0.0084 km^{-1}. In order to reconcile this with the lidar data, an inversion was done with variable-S_A such that the boundary layer extinction was closer to that measured at the surface. The result is shown in Figure 5.2.1.b.

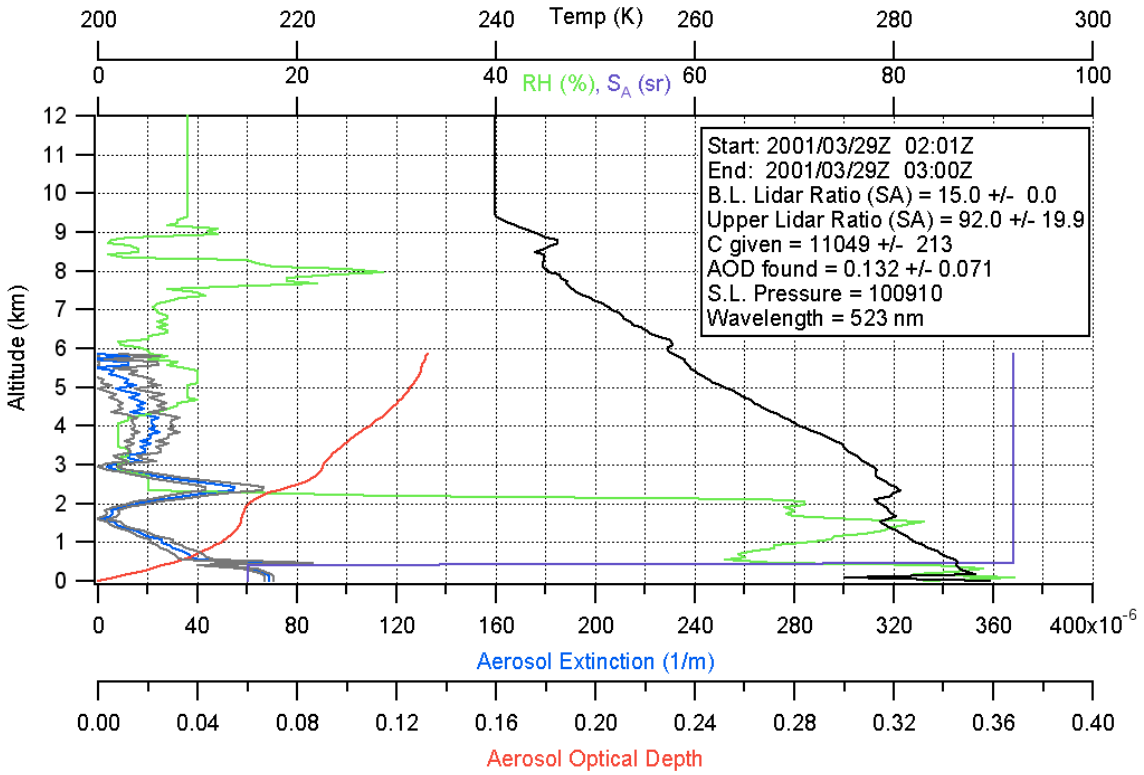

Figure 5.2.1b Same *NRB* data as in Figure 5.2.1a but inverted with variable lidar ratio constrained at the surface.

Here we see that with an S_A value of 15 we get a surface extinction of about 0.069 km^{-1}, which is still 50% more than that implied by the surface measurements. It is unlikely that S_A in the MBL was much lower than 15, so this is probably close to the best estimate of the actual extinction profile. The relatively high (92 +/- 20) S_A in the upper layers suggests a continental component to the aerosol there, with significant absorption at 523 nm. If we consult the body of knowledge concerning optical properties of aerosols by type, we find that only the "urban" and "continental" types possess lidar ratios in the 50-80 range [Ackermann, 1998, Doherty et al., 1999]. It is often the relatively strong absorption of elemental carbon and/or mineral dust that produces such high lidar ratios [Ackermann, 1998], although they can also be produced by aerosol nonsphericity. The surface elemental carbon and dust data indicate relatively low values (Figures 5.1.8 and

5.1.9), supporting the low lidar ratio in the MBL. The column value of 38.4 sr then implies the significantly higher lidar ratio above the MBL. The surface Angstrom exponent from the nephelometers was 0.44, implying large particles consistent with a relatively clean marine aerosol, while the column value (sunphotometer) was 0.52. With the boundary layer AOD at 523 nm equal to 0.036 (from Figure 5.2.1b), and the upper layers AOD equal to 0.096, we may use the surface and column Angstrom exponents to infer an average upper layer Angstrom exponent of 0.55. Here we have used

$$\tau_{A,400} = \tau_{A,523}\left(\frac{400}{523}\right)^{-\alpha} \tag{5.2.1}$$

and

$$\alpha = \frac{-\ln(\tau_{A,400}/\tau_{A,523})}{\ln(400/523)} \tag{5.2.2}$$

Figure 5.2.1c (courtesy Jim Johnson of PMEL, as are all the back-trajectories presented) shows back-trajectories from the ship's location for 950, 750 and 500 mb, corresponding to altitudes of about 0.5, 2.5 and 5.5 km respectively.

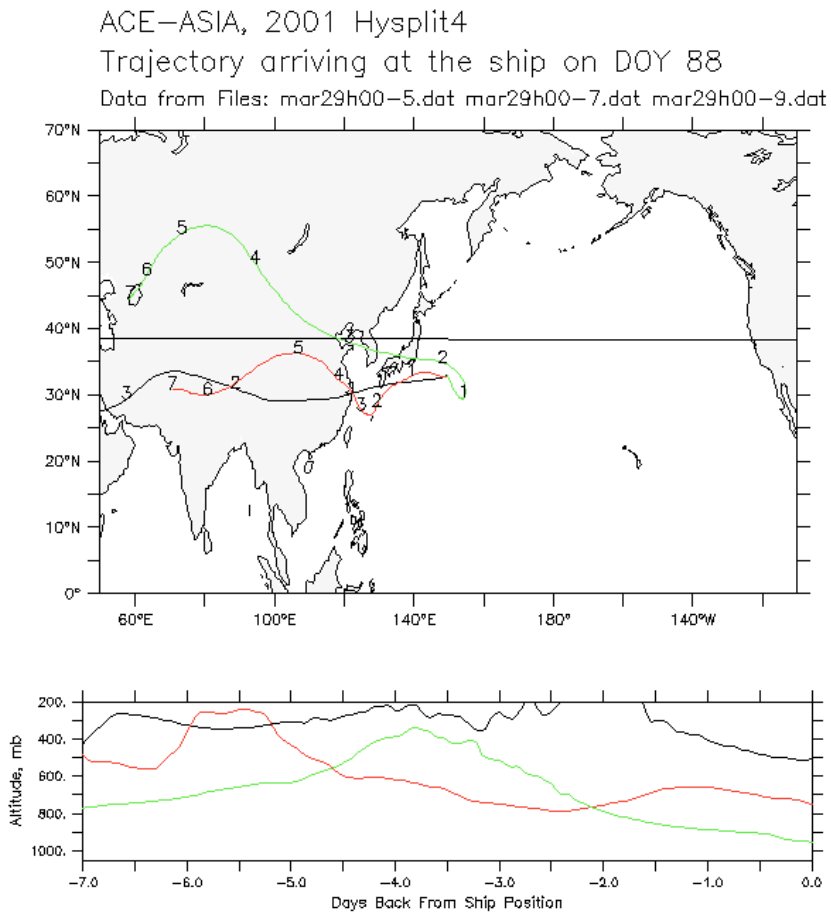

Figure 5.2.1c Back-trajectories at 3 altitudes for airmass arriving at the ship 00:00 UTC DOY 88, 2001.

Figure 5.2.1c shows that the low-level airmass has come a longer distance over the sea than the upper-level airmass, which has come quickly straight from the continent. The mid-level airmass (2.5 km) has been over the sea as long as the boundary layer, but comes from the same region as the upper-level airmass. These observations explain why the MBL aerosol was relatively cleaner, and suggest that the aerosol above 3 km may have the greatest continental component.

5.2.2 DOY 98 – April 8, 2001

On this day there was a thick boundary layer (1.4 km) and a distinct elevated layer from about 2 to 3.5 km. There was a CIRPAS Twin Otter flight over the ship from 05:54 to 06:20 Z, (2:54 to 3:20 local), and a C-130 flight from 04:29 to 04:53 UTC. The following plot shows the results of a constant-S_A inversion for the MPL data averaged over this time period:

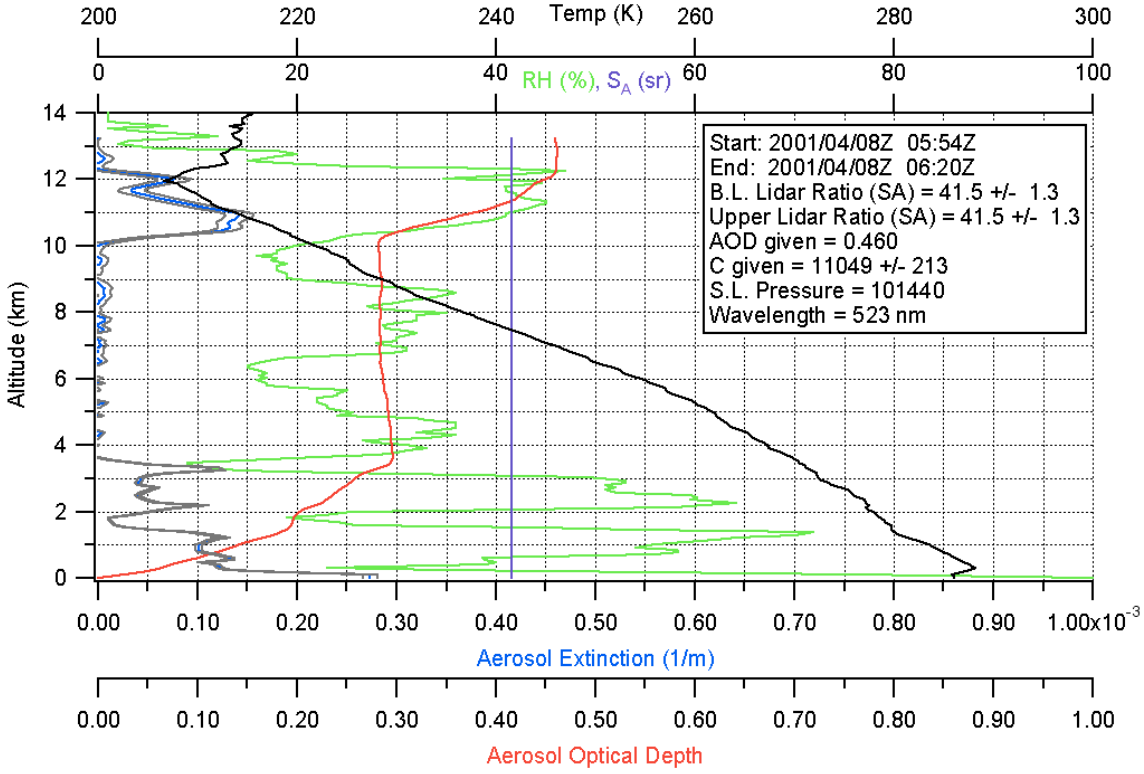

Figure 5.2.2a Constant-S_A inversion of lidar data averaged over 26 minutes during the C-130 flight, DOY 98, 2001, over the Sea of Japan.

This inversion is based on the calibrated value for C of 11049 +/- 213, and independent AOD measurements, as the data above 12 km are so noisy that the Rayleigh returns are far less certain than either the calibrated value of C or the independent AOD measurement. Sunphotometer measurements from the ship during the flight gave an AOD of 0.46 +/- 0.02. Clearly there is a thin cirrus layer from 10 to 12 km. In order to

remove this, a “below clouds” inversion was done based on the calibrated value of *C* (Figure 5.2.2b).

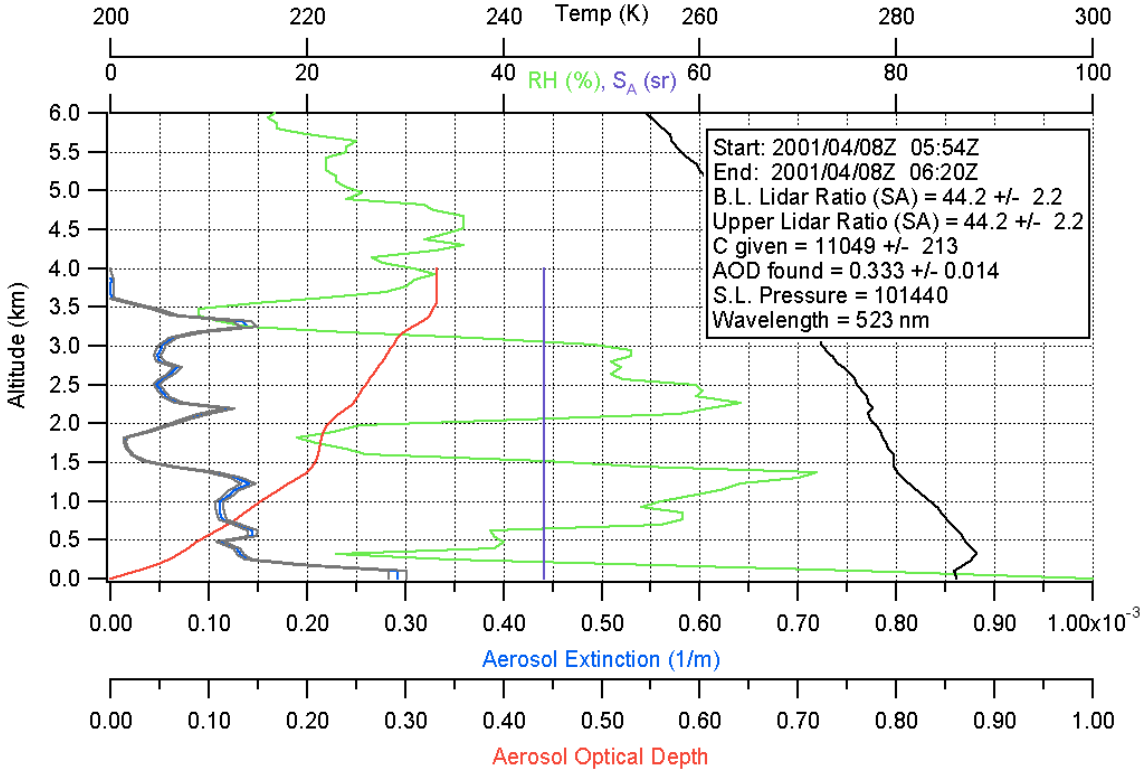

Figure 5.2.2b Same *NRB* data as in Figure 5.2.2a but inverted below cirrus layer.

The AOD found for the aerosol layers is 0.333 +/- 0.014. The suspiciously low uncertainty is due to the low noise in the data for the lower altitudes and the assumed nearly constant value of *C*. This shows a surface extinction of about 0.29 +/- 0.01 km^{-1} and a lidar ratio of 44.2 +/- 2.2 sr. At this time the ship-instrument data showed extinction at 523 nm to be 0.298 +/- 0.012 km^{-1}. These numbers agree very well, so the surface extinction suggests that S_A is fairly constant within the first 4 km. The C-130 extinction and lidar ratio data are shown below, together with the MPL versions:

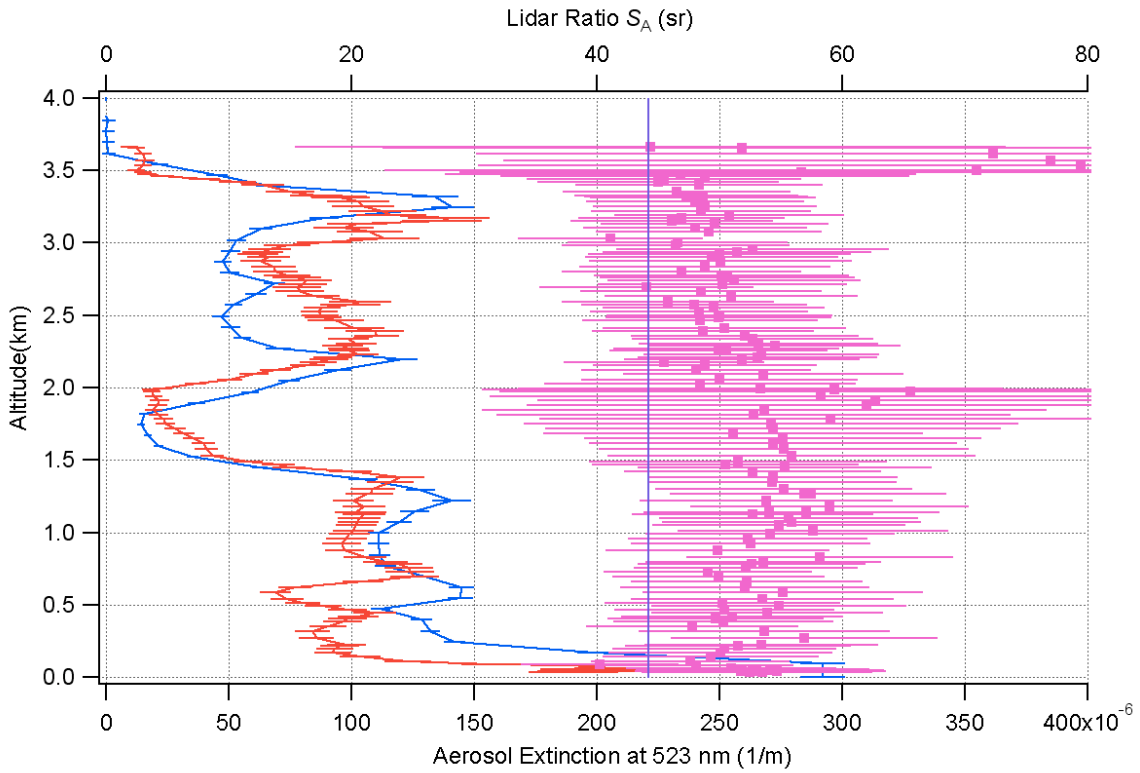

Figure 5.2.2c C-130 lidar ratio at 523 nm (pink), MPL column lidar ratio (violet), C-130 aerosol extinction (red), MPL aerosol extinction (blue) for the C-130 flight over the ship on DOY 98, 2001.

The C-130 data in Figure 5.2.2c (red - extinction, pink - lidar ratio) indicate a relatively constant lidar ratio of about 50 sr as compared to my column value of 44.2 +/- 2.2 sr, although 44.2 is for the most part within the C-130 uncertainty. The extinctions are quite similar, though they show some "layer drift" over the hour between the C-130 flight and the lidar data. The lidar extinction is consistently greater than the C-130 extinction below 700 m.

The NASA/Ames CIRPAS Twin Otter aircraft was flying this day as well, and its 14-channel sunphotometer (AATS-14) recorded an AOD profile at 525 nm in a climb during the same time period. This is shown in Figure 5.2.2d.

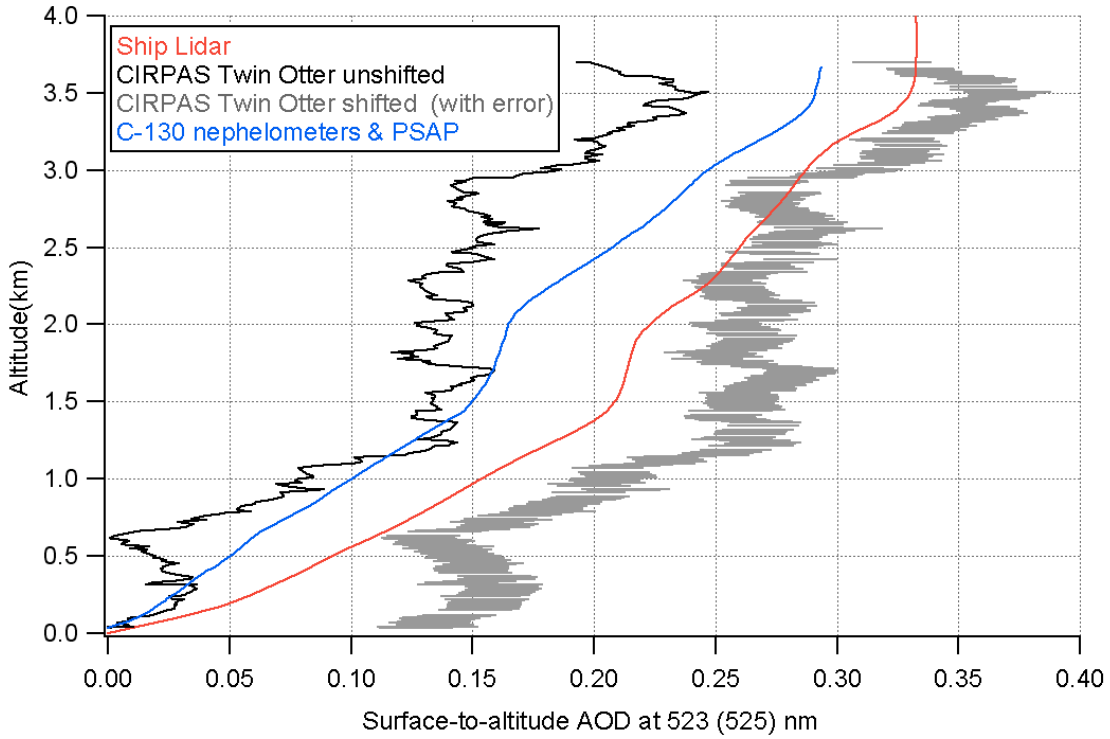

Figure 5.2.2d Comparison of C-130, Twin Otter and MPL aerosol optical depth vs. altitude. The C-130 data are for the period 0428-04:59 UTC, The Twin Otter data are also shown offset by 0.13 AOD to account for the cirrus layer, thus the surface-to-altitude AOD in the plot is not zero (see text).

The column AOD was uncertain during the Twin Otter flight – we see in the plot that the surface-to-altitude AOD decreased during the climb from 250 m to 700 m, which is impossible in a stable and horizontally homogeneous atmosphere. This suggests that the cirrus layer was variable, reducing during the beginning and end of the climb. With the average column AOD (including the cirrus layer) being 0.46 +/- 0.02 and the AOD (aerosol alone) being 0.33 +/- 0.014 (from the lidar) for the period in question, we conclude that the cirrus layer must have had an average optical depth of 0.13 +/- 0.034. To estimate the lidar ratio of the cirrus layer, the MPL data were reinverted with the aerosol lidar ratio constrained to 44.2, the value from the below-clouds inversion. The results are shown in Figure 5.2.2e.

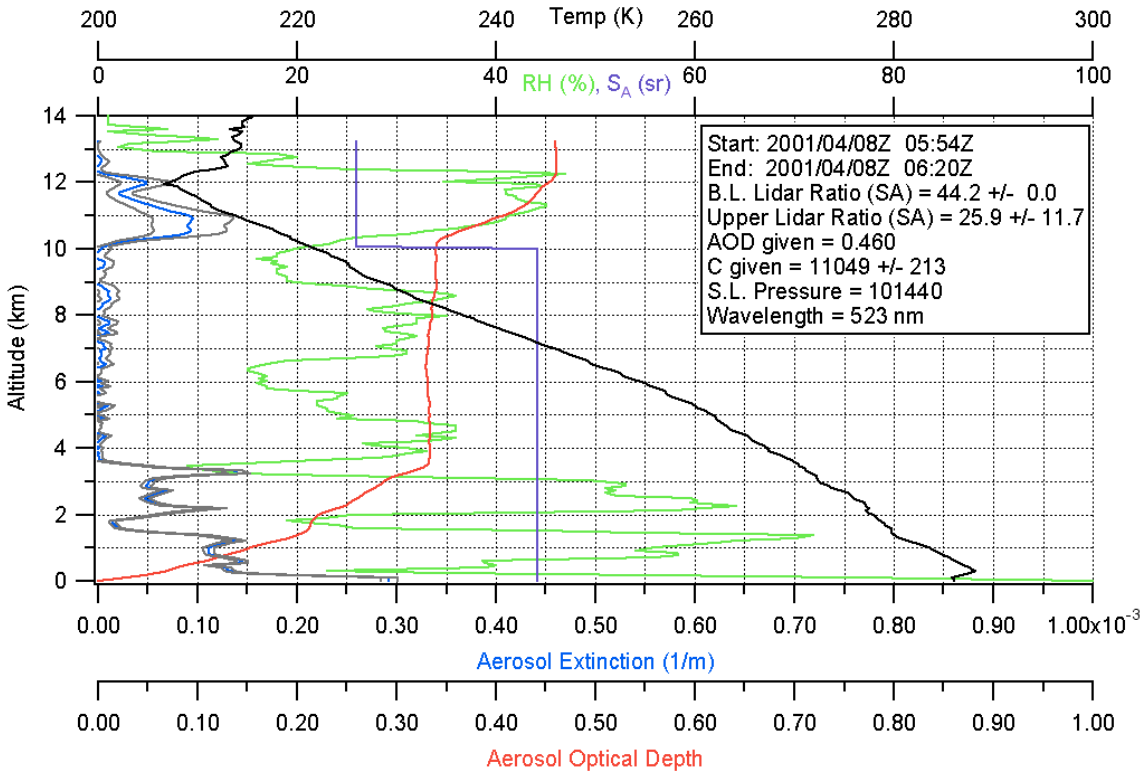

Figure 5.2.2e Same *NRB* data as in Figures 5.2.2a and 5.2.2b but with variable-S_A for cirrus layer, constrained to S_A of 44.2 for aerosol layers.

The variable-S_A inversion gives an optical depth for the cirrus layer of 0.13, as required, and an effective lidar ratio of 25.9 +/- 11.7 sr, which is compatible with measurements in the literature, such as 12.5-28.6 sr at 532 nm [Elouragini and Flamant, 1996] and 11-38 sr at 694 nm [Sassen et al., 1989]. When the optical depth of the cirrus layer is added to the Twin Otter AOD profile, we get the fairly good agreement seen in Figure 5.2.2d. AOD profiles are often differentiated with respect to altitude to obtain extinction, but this was not useful in this case as the AOD profile is too noisy, with many segments having negative slope. The Angstrom exponent from the C-130 nephelometers is shown in Figure 5.2.2f, along with the C-130 and ship surface absorption.

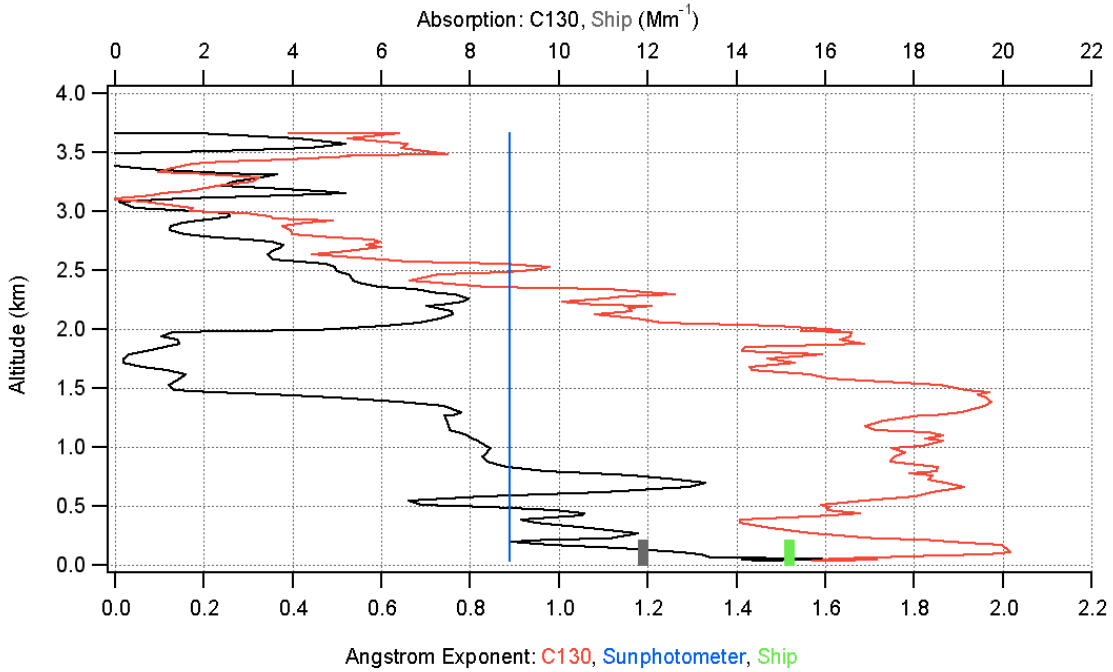

Figure 5.2.2f C-130 Angstrom exponent and absorption vs. altitude, surface Angstrom exponent and absorption from ship, column Angstrom exponent from sunphotometer on ship.

These are in good agreement and suggest that the lower layers aerosol is composed of smaller particles, the upper layers of larger particles. The column Angstrom exponent from the handheld sunphotometer data was 0.89, while the ship nephelometers obtained 1.52. The column Angstrom exponent includes the cirrus layer, which should reduce the column value from the aerosol-only value. The surface absorption of 0.012 km^{-1} is relatively high, as is the low-layer absorption from the C-130. Referring back to Figures 5.1.8 and 5.1.9, we see a high level of elemental carbon at the surface at this time (DOY 98), and a small, (yet much higher than background) level of dust. The actual number for elemental carbon within an hour after the aircraft flights was 1.25 $\mu g/m^3$, which was the fourth highest value of the cruise (recorded approximately twice per day). Of this amount, 1.06 $\mu g/m^3$ was sub-micron in size. We conclude that the higher Angstrom

exponent in the lower layers is primarily due to black carbon from continental sources mixed with the marine aerosol.

Figure 5.2.2g shows back-trajectories from the ship's location. The lower-level airmass appears to come from the continent near North Korea, a possible source of pollution, while the airmass at 2.5 km comes from the Mongolian Desert, a source of dust.

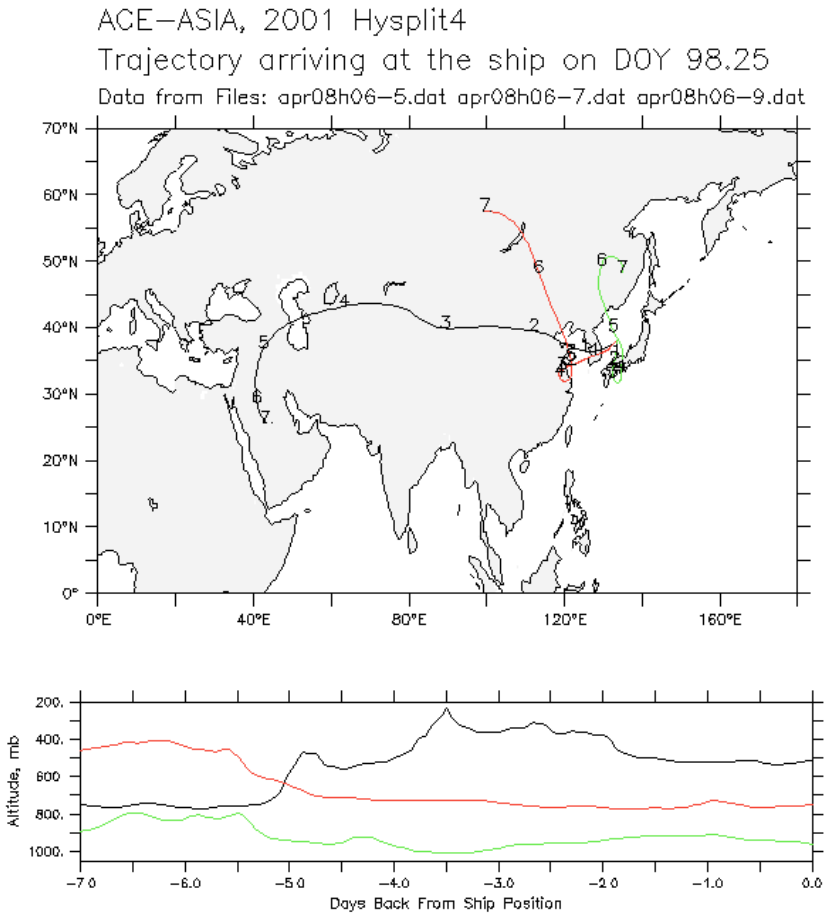

Figure 5.2.2g Back-trajectories at 3 altitudes for airmass arriving at the ship 06:00 UTC DOY 98, 2001.

Finally, we have the C-130 single-scatter albedo profile in Figure 5.2.2h: The total layer single-scatter albedo for the aerosol from 0 to 1.5 km is 0.91 while that for the aerosol from 2 to 3.5 km is 0.96, reflecting the higher absorption in the lower layers.

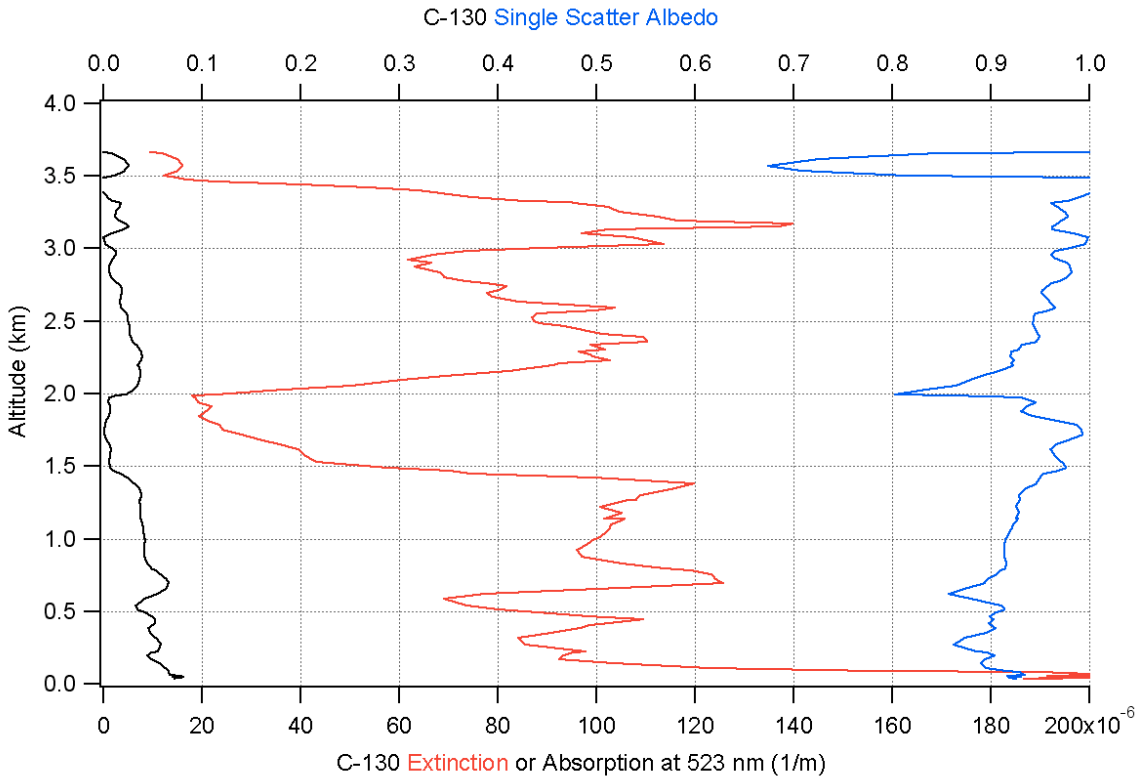

Figure 5.2.2h C-130 aerosol absorption, extinction and single-scatter albedo vs. altitude.

5.2.3 DOY 100 – April 10, 2001

On this day there was a thick boundary layer and a distinct elevated layer from about 4 to 6 km. The optical depth was quite high this day, varying from 0.6 to 1.0 at 523□m according to sunphotometer measurements. The surface extinction as measured by the lidar and the nephelometers/PSAP was among the highest of the cruise. The following plot shows the results of a constant-S_A inversion for the MPL data averaged over this time period:

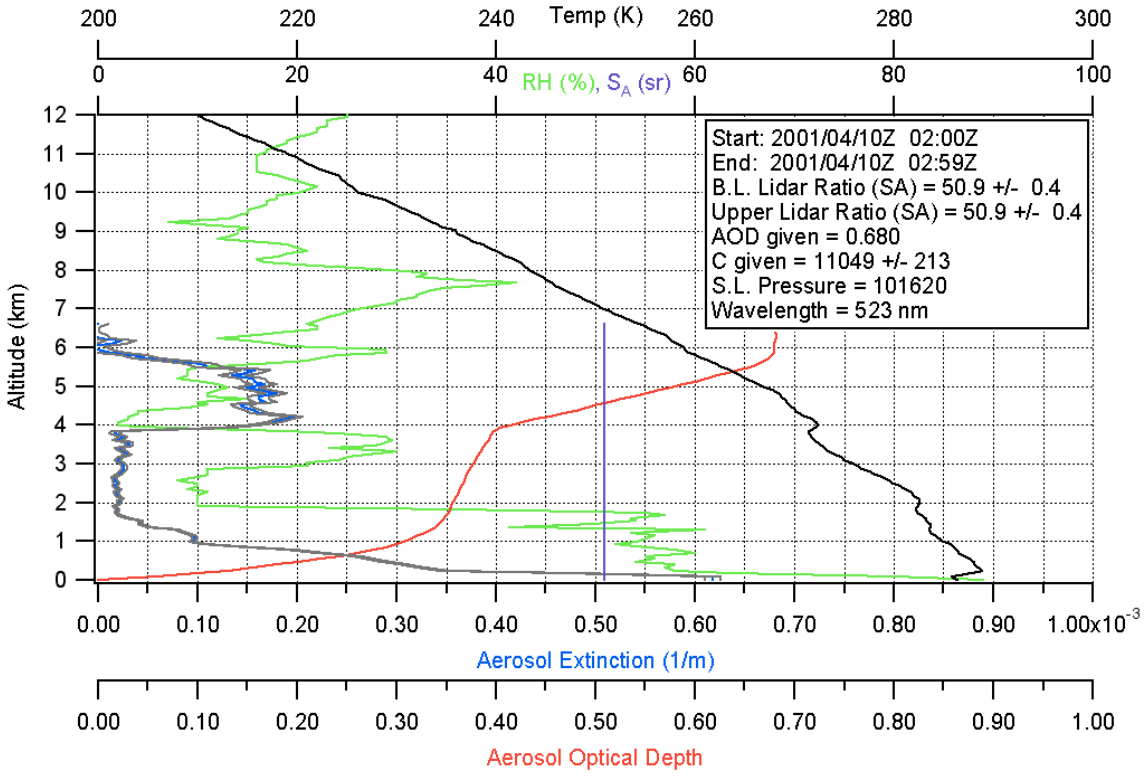

Figure 5.2.3a Constant-S_A inversion of lidar data averaged over an hour near local noon, DOY 100, 2001, over the Sea of Japan.

This inversion is based on the calibrated value for C of 11049 +/- 213, and an independent measurement of AOD from the ship of 0.68. It gives a surface extinction of about 0.62 +/- 0.01 km^{-1} and a column lidar ratio of 50.9□±□0.4□sr. At this time the ship-instrument data showed aerosol extinction at 523 nm to be 0.54□±□0.03□km^{-1}. The data

were reinverted, with the surface extinction constrained to the ship-instrument value, and the results are shown in Figure 5.2.3b.

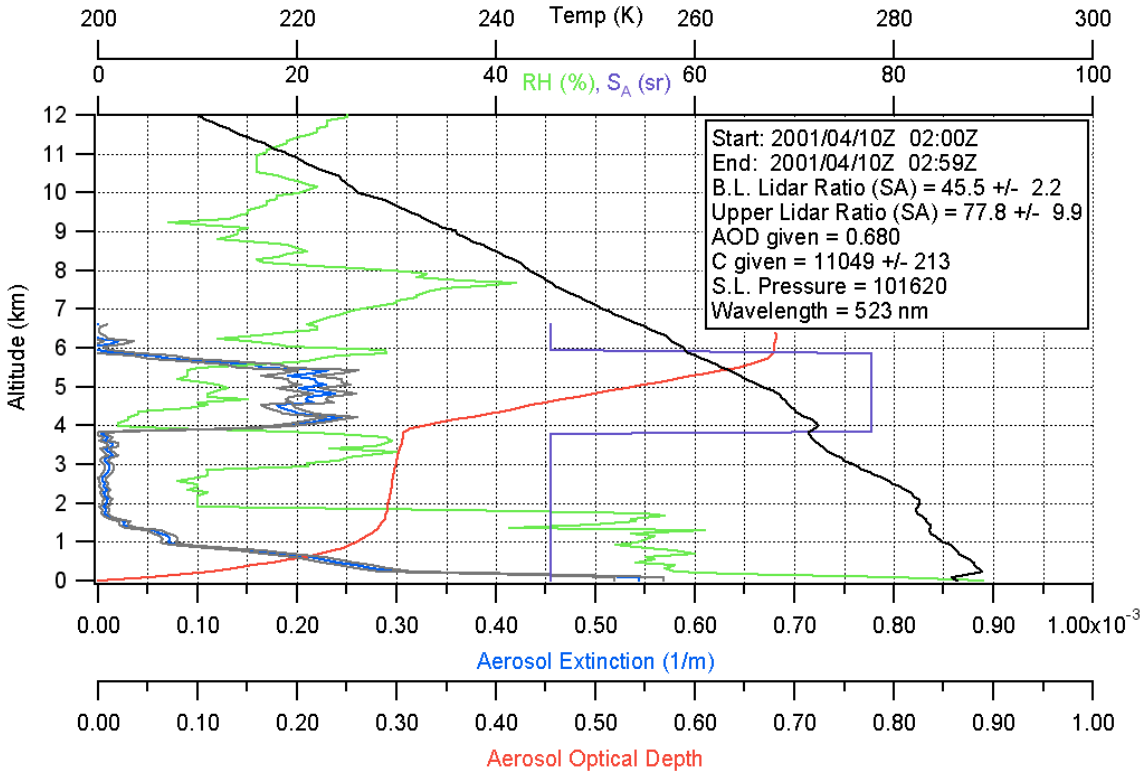

Figure 5.2.3b Same *NRB* data as in Figure 5.2.3a but inverted with variable-S_A constrained to surface extinction measured by ship nephelometers..

We assume that the upper layer is well-mixed and limited to the altitudes between 3.8 and 6 km. The surface-extinction constraint forces a lidar ratio for the upper layer of 77.7□+/-□9.9 sr, suggestive of absorbing aerosols such as dust and/or black carbon. Referring back to Figure 5.1.8 and 5.1.9, we see that the black carbon and dust levels at the surface were not particularly high compared to values a short time later, suggesting that most of the dust and/or black carbon was in the elevated layer. The lidar ratio for the lower layers being 45.5 sr indicates that the surface aerosol was also somewhat contaminated with continental components. The surface Angstrom exponent from the

ship nephelometers was 1.32, indicating smaller particles mixed with sea salt. The column Angstrom exponent (sunphotometer) was 0.86.

Figure 5.2.3c shows the back-trajectory plots for the airmass arriving at the ship 2 hours before the period being discussed:

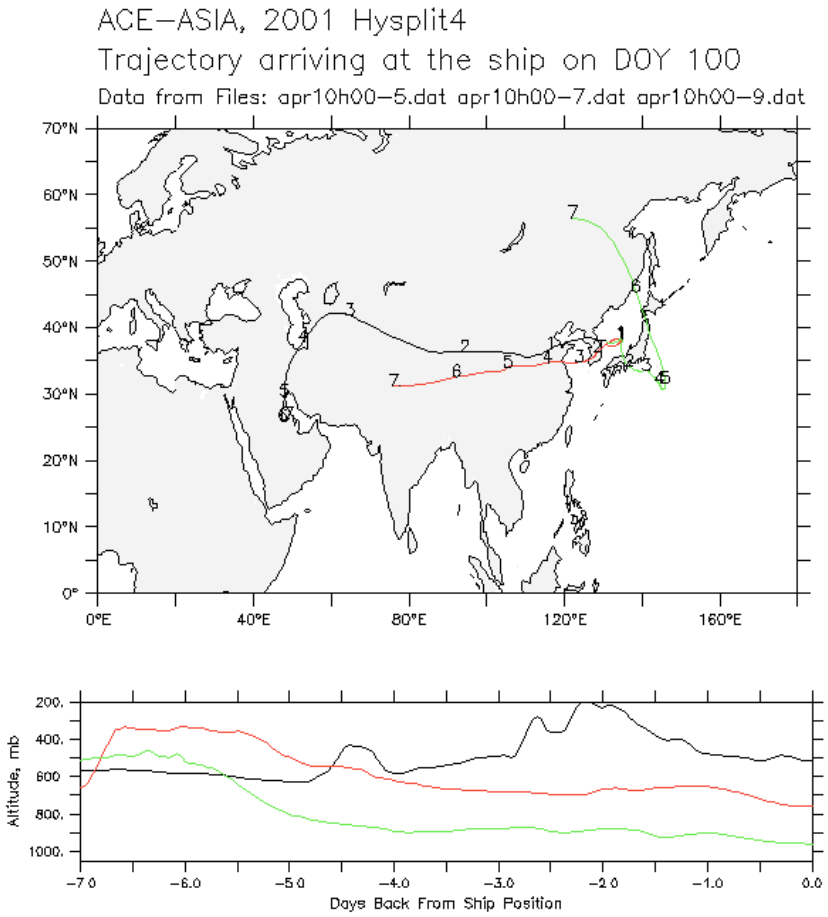

Figure 5.2.3c Back-trajectories at 3 altitudes for airmass arriving at the ship 00:00 UTC DOY 100, 2001.

We see that the upper-level airmass came from the continent, where dust and soot originate, while the lowest-level airmass had been at sea, and over Japan, before arriving at the ship.

5.3 Two-Layer Analysis of the Cruise

Finally, we turn again to the entire period during which lidar observations were made, and examine the results of two-layer variable lidar ratio inversion, constrained to independently measured surface extinction as in the previous examples. Boundary layer height was determined as the first altitude at which the constant lidar ratio extinction falls to less than half of its lower maximum, or where the RH changes by half its value. The boundary layer lidar ratio was limited to a minimum value of 15 sr. Figure 5.3.1 shows the recovered aerosol extinction vs. altitude for the cruise. Sharp discontinuities are sometimes apparent. These are due to the sudden change in lidar ratio above the assumed boundary layer. Figure 5.3.2 shows the recovered lidar ratio for the boundary layer and upper layers. The general effect of constraining the inversions to the independently measured surface extinction is to place more of the aerosol extinction in upper layers.

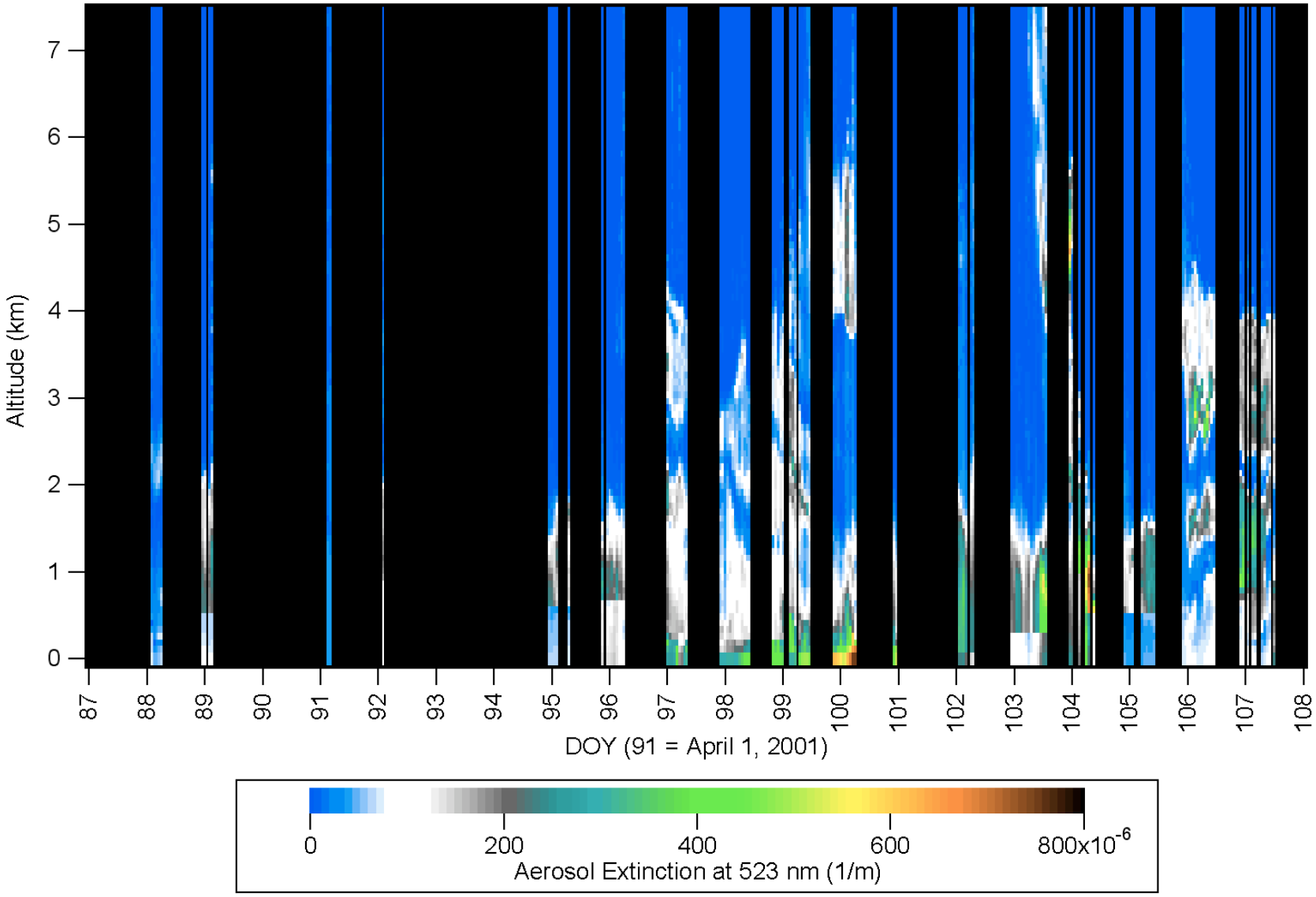

Figure 5.3.1 Vertical profiles of aerosol extinction at 523 nm from variable lidar ratio inversion of MPL data for ACE-Asia cruise.

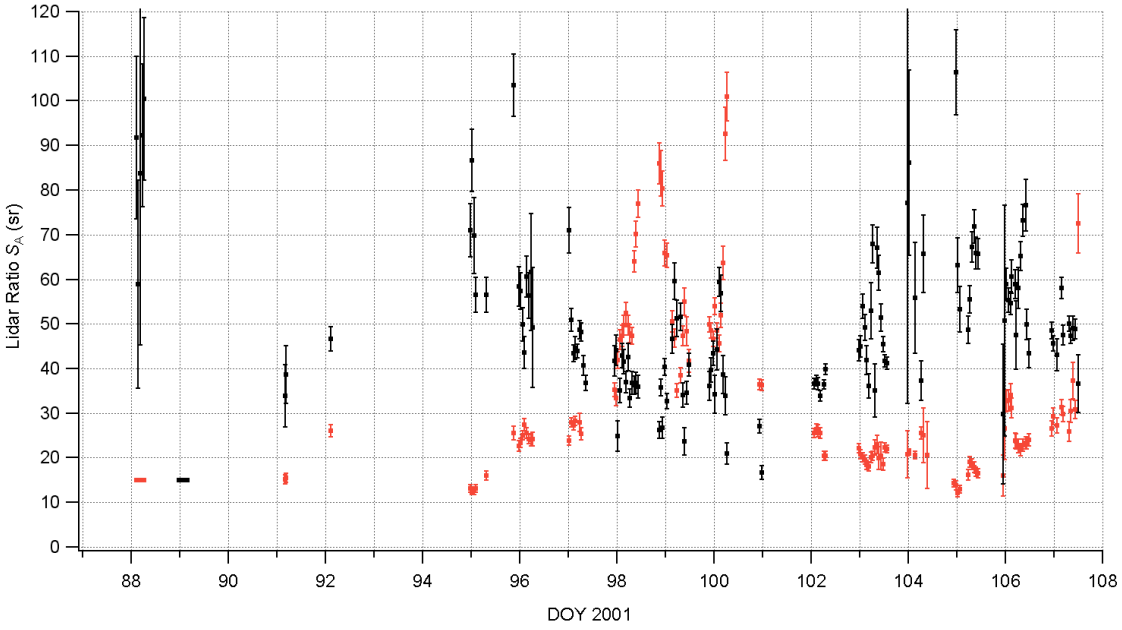

Figure 5.3.2 Recovered lidar ratio for boundary layer (red) and upper layers (black).

Note that the lidar ratio for the upper layers is higher than that for the boundary layer, except for the period from DOY 98 to DOY 101. This period included some of the highest surface black carbon and dust concentrations, with apparently cleaner aerosols above.

The "blue-green" (using wavelengths from 400 to 550 nm) Angstrom exponent was measured at the surface by the nephelometers, and for the column (when possible) by sunphotometer. The boundary layer Angstrom exponent and the implied upper level Angstrom exponent are shown in Figure 5.3.3.

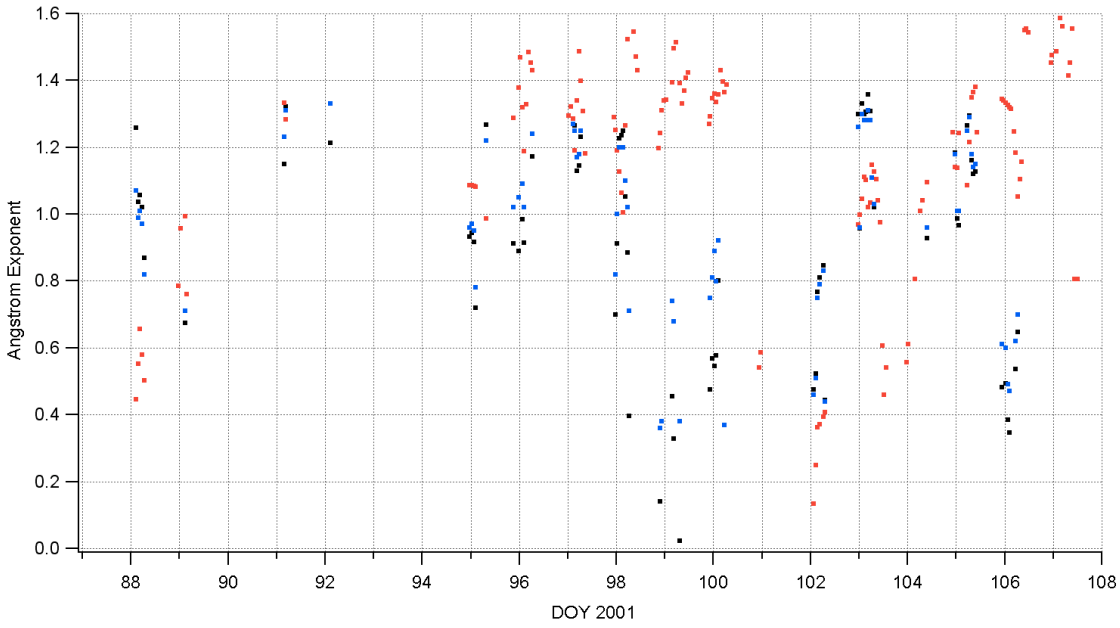

Figure 5.3.3 Angstrom exponents: Boundary layer (red), upper layers (black) and column (blue).

We see that the Angstrom exponents in the upper layers are higher than or comparable to those in the boundary layer, except for the period from DOY 97 to DOY 101. This indicates the upper layer aerosol was "cleaner" (meaning less dust and black carbon) than the boundary layer during this period, in agreement with the lidar ratio data (Figure 5.3.2).

Figure 5.3.4 shows the total AOD and the fraction in the boundary layer for the cruise. The mean fraction of AOD in the boundary layer was 18.5%. Figure 5.3.5 shows the integrated aerosol extinction with contours at 25, 50, 75, 90, and 95%, and the boundary layer height. Those portions exceeding 7 km are suspected of containing thin cirrus.

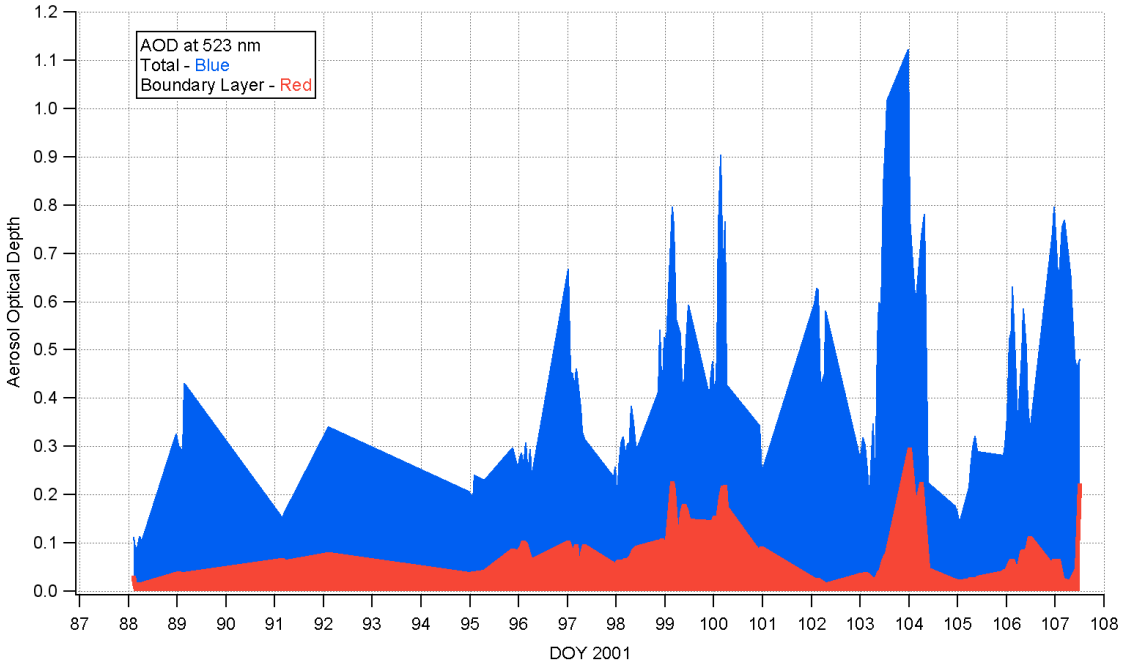

Figure 5.3.4 Total AOD (blue) and boundary layer AOD (red) at 523 nm.

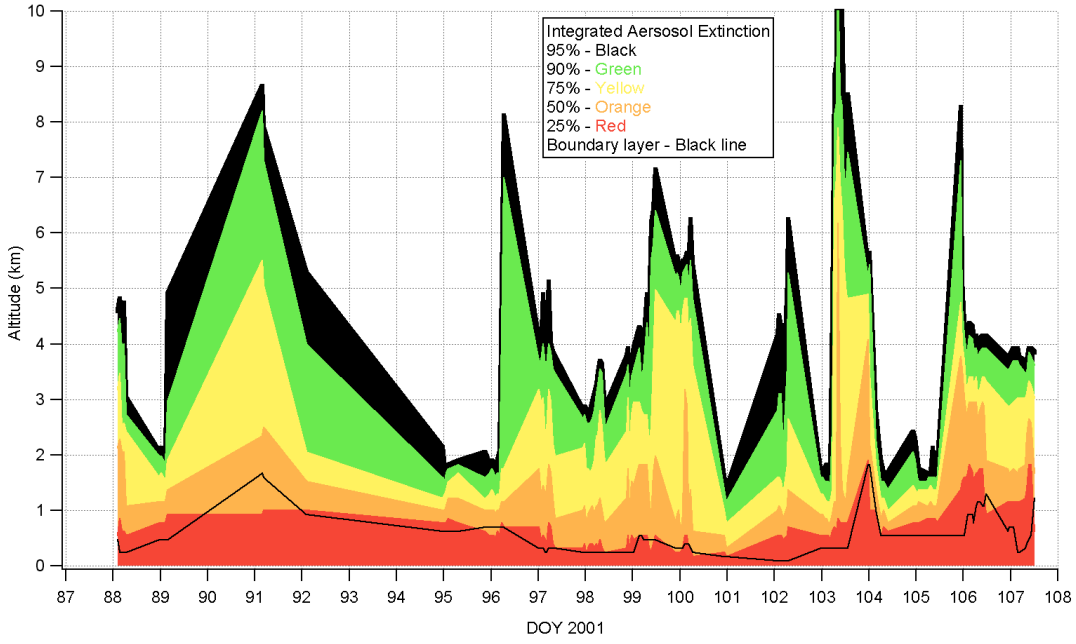

Figure 5.3.5 Integrated aerosol extinction (surface-to-height AOD) at 523 nm.

Ch. 6. Conclusions and Future Applications

6.1 Lidar Analysis Techniques

Improved techniques for the analysis of lidar data, incorporated in a semi-automatic inversion algorithm, have been presented. Tests with noisy pseudodata have demonstrated that this inversion algorithm can better recover the vertical structure of aerosol extinction coefficient and lidar ratio. Application of the improved algorithm to field data has shown the ability to calibrate the lidar, in particular, the determination of the system constant *C*. This calibration allows the recovery of aerosol vertical structure under clouds, and aerosol optical depth when conditions prevent the use of passive methods. The uncertainty in the recovered optical properties increases with altitude and decreases with collection and averaging time. The RMS uncertainty in recovery of column lidar ratio for the data analyzed in this dissertation was 3.1 sr. The mean uncertainty in recovered AOD when inverting to *C* was +/- 0.06. The lidar can also be used to identify thin cirrus layers and estimate their optical depth and lidar ratio.

It has also been demonstrated that the technique of constraining a lidar inversion to an independent measurement of extinction at the surface can provide information on the optical properties of elevated layers.

6.2 ACE-Asia Lidar Data

The lidar data from the ACE-Asia cruise have been inverted using the improved algorithm. The resulting extinction profiles and lidar ratios have been presented along with uncertainties. They show elevated (2-6 km) aerosol layers on DOYs 97-107, 2001 over the Sea of Japan and nearby waters during the spring dust event. The mean column lidar ratio for the period from DOY 88 to DOY 107 was 40.1 sr, with an RMS variability of 7.5 sr. With variable lidar ratio inversion, the mean boundary layer lidar ratio was 30.2 sr while the mean upper layer lidar ratio was 50.2 sr with variabilities of 19.6 sr and 18.2 sr respectively. These lidar ratios are higher than for clean marine aerosols, and chemical analysis has shown the primary cause to be dust and black carbon. Lidar ratios > 45 sr in upper-level aerosol layers suggest substantial absorption. This is supported by comparisons with aircraft measurements.

6.3 Future Applications

It is clear that an elastic backscatter lidar in the mid-visible range can provide important vertical information about aerosols and cirrus clouds. As this is one of the greatest sources of uncertainty in radiative forcing calculations, one would expect to see an increase in the deployment of lidars around the world. NASA's MPLNET and the European Commission's EARLINET are two programs that promise to do just that. The availability of real-time vertical information about aerosols will provide the much needed input to global climate models to allow greater accuracy in their predictions. It will also help with the interpretation of data from space-borne instruments, such as MODIS and SeaWiFS.

Micro Pulse Lidars are particularly suited to field-deployment. They will certainly be used increasingly in aerosol and cloud field studies. The data collected by lidar during ACE-Asia is already being incorporated into a local climatology for the Asian Pacfic region, just as with ACE-1 in the region near Tasmania, ACE-2 around the Canary Islands, Aerosols99 in the Atlantic, and INDOEX in the Indian Ocean. As more data is collected, we will be much better equipped to identify trends in the production and vertical distribution of aerosols, and their effect on the environment.

References

Ackermann, Jorg, The Extinction-to-backscatter Ratio of Tropospheric Aerosol: A Numerical Study, *Journal of Atmospheric and Oceanic Technology, V15*, 1043-1050, 1998.

Ackermann, Jorg, P. Volger, and M. Wiegner, Significance of multiple scattering from tropospheric aerosols for ground-based backscatter lidar measurements, *Applied Optics, V38*, No. 24, 5195-5201, 1999.

Ansmann, A., M. Riebesell, U. Wandinger, C. Weitkamp, E. Voss, W. Lahmann, and W. Michaelis, Combined Raman Elastic-Backscatter LIDAR for Vertical Profiling of Moisture, Aerosol Extinction, Backscatter, and LIDAR Ratio, *Applied Physics B, V55*, 18-28, 1992.

ARM Aerosol Working Group Report, http://www.arm.gov/docs/documents/tech_reports/aerosol_wg2000.pdf, July 2000.

Chomko, Roman M., and Howard R. Gordon, Atmospheric correction of ocean color imagery: use of the Junge power-law aerosol size distribution with variable refractive index to handle aerosol absorption, *Applied Optics, V37,* No. 24, 5560-5572, 1998.

Doherty, Sarah J., T. L. Anderson, and R. J. Charlson, Measurement of the lidar ratio for atmospheric aerosols with a 180 backscatter nephelometer, *Applied Optics, V38*, No. 9, 1823-1828, 1999.

Dubovik, Oleg, B. Holben, T. E. Eck, A. Smirnov, Y. J. Kaufman, M. D. King, D. Tanre, and I. Slutsker, Variability of Absorption and Optical Properties of Key Aerosol Types Observed in Worldwide Locations, *Journal of the Atmospheric Sciences, V59*, 590-608, 2002.

Elouragini, Salem and P. H. Flamant, Iterative method to determine an averaged backscatter-to-extinction ratio in cirrus clouds, *Applied Optics, V35*, 1512-1518, 1996.

Fernald, Frederick G., Analysis of atmospheric lidar observations: some comments, *Applied Optics, V23*, 652-653, 1984.

Fernald, Frederick G., B. M. Herman, and J. A. Reagan, Determination of Aerosol Height Distributions by Lidar, *Journal of Applied Meteorology, V11*, 482-489, 1972.

Filippenko, Alexei V., The Importance of Atmospheric Differential Refraction in Spectrophotometry, *Publications of The Astronomical Society of the Pacific*, *V94*, 715-721, 1982.

Gordon, Howard R., Atmospheric correction of ocean color imagery in the Earth Observing System era, *Journal of Geophysical Research, V102,* No. D14, 17081-17106, 1997.

Gordon, Howard R., T. Du, and T. Zhang, Remote sensing of ocean color and aerosol properties: resolving the issue of aerosol absorption, *Applied Optics, V36*, 8670-8684, 1997.

Huang, I. H., personal communication, Science and Engineering Services, Inc., 2002.

Huebert, Barry J., ACE-Asia Project Prospectus, http://saga.pmel.noaa.gov/aceasia/prospectus/prospectus022601.html, 2001.

Menzies, Robert T., D. M. Tratt, J. D. Spinhirne, D. L. Hlavka, Aerosol layers over the Pacific Ocean: Vertical distributions and optical properties as observed by multi-wavelength airborne lidars, *Journal of Geophysical Research, V107*, No. D16, **AAC 5** 1-16, 2002.

Ramanathan, V., P. J. Crutzen, J. Lelieveld, A. P. Mitra, D. Althausen, J. Anderson, M. O. Andreae, W. Cantrell, G. R. Cass, C. E. Chung, A. D. Clarke, J. A. Coakley, W. D. Collins, W. C. Conant, F. Dulac, J. Heintzenberg, A. J. Heymsfeld, B. Holben, S. Howell, J. Hudson, A. Jayaraman, J. T. Kiehl, T. N. Krishnamurti, D. Lubin, G. McFarquhar, T. Novakov, J. A. Ogren, I. A. Podgorny, K. Prather, K. Priestly, J. M. Prospero, P. K. Quinn, K. Rajeev, P. Rasch, S. Rupert, R. Saourny, S. K. Satheesh, G. E. Shaw, P. Sheridan, and F. P. J. Valero, Indian Ocean Experiment: An integrated analysis of the climate forcing and effects of the great Indo-Asian haze, *Journal of Geophysical Research, V106*, No. D22, 28,371-28,938, 2001.

Quinn, P. K., T. S. Bates, D. J. Coffman, T. L. Miller, J. E. Johnson, D. S. Covert, J.-P. Putaud, C. Neususs, and T. Novakov, A comparison of aerosol chemical and optical properties from the 1st and 2nd Aerosol Characterization Experiments, *Tellus, V52B*, 239–257, 2000.

Sassen, Kenneth, M. K. Griffin, and G. C Dodd, Optical Scattering and Microphysical Properties of Subvisual Cirrus Clouds, and Climatic Implications, *Journal of Applied Meteorology, V28*, 91-98, 1989.

Schneider, J., D. Balis, C. Bockmann, J. Bosenberg, B. Calpini, A. P. Chaikovsky, A. Comeron, P. Flamant, V. Freudenthaler, A. Hagard, I. Mattis, V. Mitev, A. Papayannis, G. Pappalardo, J. Pelon, M. R. Perrone, D. P. Resendes, N. Spinelli, T. Trickl, G. Vaughan, and G. Visconti, A European aerosol research lidar network to

establish an aerosol climatology (EARLINET), *Journal of Aerosol Science, V31*, S592-S593, 2000.

Spinhirne, James D., Micro Pulse Lidar, *IEEE Transactions on Geoscience and Remote Sensing, V31*, No. 1, 48-55, 1993.

Spinhirne, James D., Compact Eye Safe Lidar Systems, *Review of Laser Engineering, V23*, No. 2, 26-32, 1995.

Turner, David D., R. A. Ferrare, L. A. H. Brasseur, W. F. Feltz, T. P. Tooman, Automated Retrievals of Water Vapor and Aerosol profiles from an Operational Raman Lidar, *Journal of Atmospheric and Oceanic Technology, V19*, 37-50, 2002.

United States Standard Atmosphere 1976, program adapted from fortran courtesy Public Domain Aeronautical Software (PDAS), http://www.pdas.com/atmos.htm, 2002.

Voss, Kenneth J., E. J. Welton, P. K. Quinn, J. Johnson, A. M. Thompson, and H. R. Gordon, Lidar measurements during Aerosols99, *Journal of Geophysical Research, V106*, No. D18, 20821-20831, 2001.

Welton, Ellsworth J., *Measurements of Aerosol Optical Properties Over the Ocean Using Sunphotometry and Lidar*, doctoral dissertation, June, 1998.

Welton, Ellsworth J., J. R. Campbell, T. A. Berkoff, J. D. Spinhirne, S. Tsay, and B. Holben, *First Annual Report: The Micro-pulse Lidar Worldwide Observational Network (MPL_Net)*, Project Report, 2001.

Zuev, V. E., Laser-Light Transmission Through the Atmosphere, *Topics in Applied Physics Volume 14: Laser Monitoring of the Atmosphere*, E. D. Hinkley, ed., Springer-Verlag, NY, 1976.